Characterization, Modeling, and Applications of Novel Magneto-Rheological Elastomers

A thesis submitted to the Miami University
Honors Program in partial fulfillment of the
Requirements for University Honors with Distinction

Author: Robert Sinko
Mechanical Engineering and Statistics Major
Miami University, Oxford, Ohio
May 2012

ABSTRACT

Characterization, Modeling, and Applications of Novel Magneto-Rheological Elastomers

by Robert Sinko

Magnetorheological elastomers (MREs) are an emerging branch within the smart materials field that consists of hard or soft magnetic particles embedded in a rubber compound. Current applications and research have been focused on changing the stiffness of these materials by applying an external magnetic field. Components of vibration absorbers and base isolation systems that employ this material have shown the capability of offering improved performance over conventional solutions. These particular applications use soft magnetic material; however, MRE materials containing hard magnetic filler materials (those that remain permanently magnetized) were the primary focus of this project and are referred to as H-MREs. When a magnetic field is applied perpendicularly to these particles, the filler particles generate a net torque and these samples can be used as a controlled actuator. Preliminary work has been conducted to characterize these H-MREs (since their properties are significantly different than "soft" MREs) and this work has shown their usefulness in engineering applications. However, unlike comparable smart materials such as piezoelectrics and electroactive polymers (EAP), additional modeling and experimentation needs to be conducted in order to develop usable models and better understand their behavior. The first portion of this paper focuses on developing experimental models to predict the behavior of H-MRE materials as cantilevered beam actuators for use in future applications.
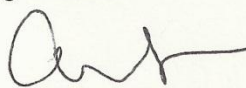
Two additional, newer applications for which H-MREs could be useful are energy harvesting and sensing. Sensors are utilized almost everywhere today as they are used to monitor the performance of a system (whether it is fluid flow, vibration measurements, etc.). Piezoelectric materials, those that respond to electric stimuli, and Galfenol, an engineered material similar to MREs, have been studied extensively for their application as self-sensing actuators. It is hypothesized that H-MREs could be used in a similar capacity by developing a way to monitor the displacement of the material using a magnetic circuit. Based on a similar principle, energy harvesting involves the conversion of one form of energy (kinetic, solar, etc.) into a more storable form. Previous research has been conducted using other smart materials in this capacity and it is also hypothesized that H-MREs could be used in a similar capacity by capturing energy from mechanical vibrations and storing it in the form of electrical energy/power using a specialized circuit and the same principles discussed above. The primary goal of the second portion of this project will be to determine the feasibility of using H-MREs in the capacity of energy harvesting and sensing technologies. This feasibility study includes the development of experiments to assess these capabilities and the implementation of the experiments for verification of the predicted behavior. Finally, much consideration is given to work that will need to be done in the future in order to fully understand the behavior of these materials and allow them to be implemented in future relevant applications.

Characterization, Modeling, and Applications of Novel Magneto-Rheological Elastomers

By Robert Sinko

Approved by:

_____, Advisor
Dr. Jeong-Hoi Koo

_____, Reader
Dr. Amit Shukla

_____, Reader
Dr. Kumar Singh

Accepted by:

_____, Director, University Honors Program
Dr. Carolyn Haynes

v

Acknowledgements

I would like to thank a number of people who have contributed to the completion of this project, as well as provided guidance throughout the course of the project.

Table of Contents

List of Figures

List of Tables

Introduction: Magneto-Rheological Elastomers

In the engineering field, it has been identified that most materials respond to external stimuli in some fashion, such as how metals will tend to expand and contract when exposed to a change in temperature or how glass will shatter when imparted with a force beyond its strength. All of these properties are inherent to the nature of the materials and are a result of their atomic structure, processing, time in use, or any of a number of other important factors. Smart materials are similar in that they also respond to some sort of external stimulus, such as magnetic or electric fields, temperature, presence of moisture, etc. However, the distinguishing feature that sets them apart from conventional materials is that these changes due to external stimuli have been purposely engineered into the properties of the material and can be exploited for use in a wide-ranging scope of applications. Some of these applications include use in electronics, biomedical devices, and countless others ranging from large-scale civil engineering projects (bridge and road constructions) to small-scale nanotechnology applications.

Magnetorheological fluids (MRFs) were discovered in 1948 by Ranibow [1] as one of the first smart materials and involve the dispersion of magnetic particles within a viscous fluid. The operating principle of these smart materials is that when a magnetic field is applied around the materials, the magnetic particles will tend to align themselves with the magnetic field and form chains within the fluid. These chains alter the viscosity/damping characteristics of the fluid by impeding motion of the fluid and ultimately change the response of the system to any loading [2]. This branch of smart materials has become particularly useful in the automotive industry as a component of suspension systems where they are included as part of the shock absorbers. In particular, the 2010 Acura ZDX [3] has implemented these fluids in their suspension system to allow riders to experience the highest quality ride possible. The success of MRFs in engineering applications demonstrates that smart materials are becoming widely adopted and particularly useful; encouraging the development of even more smart materials since the inception of MRFs and remaining at the forefront of engineering research today.
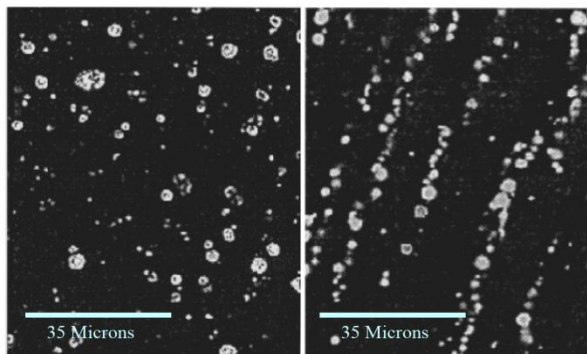
Figure 1: Microscopic view of MRE materials showing the dispersion of magnetic particles (white) within the base elastomer (black). The SEM image on the right shows a random dispersion of magnetic particles, while the image on the right illustrates the magnetic particles ordered into chains; a characteristic of H-MREs.

Magneto-rheological elastomers (MREs), pictured above in Figure 1, are an emerging branch within the smart materials field (derived from MRFs) that consist of hard or soft magnetic particles [4] embedded in a rubber compound. The properties of these materials can be changed significantly based on the type of filler particles used as well as the rubber compound. The operating principles of these materials are two-fold, depending on the type of magnetic filler

particle that is embedded within the base elastomer. For soft magnetic particles, those that only become magnetized in the presence of an external magnetic field, their behaviors are nearly identical to those of MRFs. In MRFs, the magnetic particles are free to move within the viscous fluid to freely form chains when a magnetic field is applied. In MREs, however, the magnetic particles still try to form chains but are trapped within the elastomer base and cannot move a significantly through the material. In trying to form these chains, the particles cause a change in stiffness of the material that can be exploited for numerous engineering applications. Such applications where a dynamic stiffness change is desirable are base isolation systems or adaptive vibration absorbers [5, 6]. Davis [7] has shown that the stiffness of these materials can be changed by nearly 100% (as measured by the shear modulus) when the particles are aligned by an external magnetic field, as illustrated by the results of his experiment below in Figure 2.
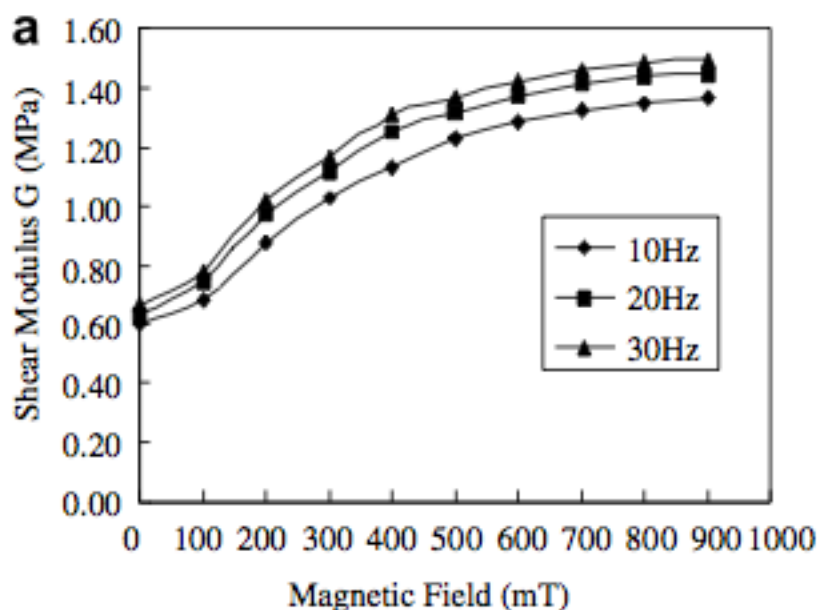
Figure 2: Plot created by Davis [7] illustrating the change in shear modulus (measure of stiffness) of MRE materials when an external magnetic field is applied.

On the other hand, MREs that contain hard magnetic filler materials, those that remain permanently magnetized, possess different behaviors and properties and are the scope of this investigation. In fabricating these H-MRE samples, the magnetic particles are made to be aligned with a particular orientation. This is accomplished by placing the samples within an electromagnet while the base elastomer cures in order to form permanent chains of magnetic particles as pictured below in Figure 3. This is a process that can be done with soft filler particles as well in order to mimic H-MRE materials for certain applications [8], however, using hard magnetic filler particles creates a net permanent magnetization for these materials [7]. This net magnetization opens the door for a number of additional applications for MRE materials in general including, but not limited to, the three primary areas of this investigation: actuators, sensors, and energy harvesters.
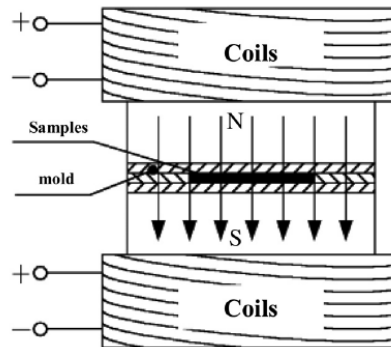
Figure 3: Set-up for the alignment of magnetic particles within an H-MRE sample during fabrication [7]. The sample can be placed within the electromagnet in any direction to ensure proper orientation for a given application.

Although some preliminary work has been conducted on characterizing the behavior of H-MREs, there is still much work to determine their potential for future engineering applications and implementation. The focus of this thesis paper is to try and characterize and investigate the feasibility of using H-MRE materials in a number of different applications; particularly sensing, energy harvesting, and actuation. The scope of this project included the fabrication of H-MRE samples using a process developed at Miami University, design and implementation of experiments to assess the capabilities of H-MREs for the given applications, as well as model development based on the experimental results. The following sections detail the process of inquiry utilized in this thesis and the results demonstrating the capabilities of H-MREs as a novel smart material for engineering applications.

H-MRE Actuators: Displacement and Blocking Force

One of the simplest and most important applications of H-MRE technology is the implementation of the materials as actuators. In previous studies, a number of other smart materials have been implemented as actuators through the use of electric stimuli, such as piezoelectric materials [9, 10] and electro-active polymers (EAP) [11]. These materials have proven to be capable and reliable devices in this field. However, H-MRE materials offer a number of potential improvements over conventional smart actuators including:

- The ability to be actuated without any physical connection to the material. Both piezoelectrics and EAPs require some electric stimuli to be applied directly to the material, whereas H-MRE materials can be remotely controlled by simply varying the magnetic field around the material.

- The ability to be fabricated into actuators of any shape and size. One of the limitations of piezoelectric and EAP materials are that they are very fragile and their properties degrade if made into larger samples, which is not the case for MRE materials.

Based on these primary factors and a number of others, it is clear that H-MRE materials offer a number of advantages over the status quo for actuation technology. In order to adequately assess their capabilities as actuators, experiments needed to be designed to measure both the displacement of the material and the blocking force [9, 10]. The displacement is important since it helps to define the bending characteristics of the material, while the blocking force is important

since it helps to quantify the scope of applications for which these actuators would be most appropriate. That is, the amount of force these actuators can provide needs to be evaluated to determine if they could be used in large machines or micro devices. For this application of H-MRE technology in the thesis, the focus was on a combination of experimentation and theoretical modeling as discussed in the following sections. The first portion of this section deals with the displacement modeling of the actuator, while the second goes on to look at the blocking force.

Displacement Experimentation and Modeling

The focus of this portion of the study is to investigate the mechanisms of bending in H-MRE samples and to then determine an accurate theoretical model to predict the behavior of samples as actuators. Principles of traditional beam bending theories are utilized to develop a basic model that predicts the deflection of a cantilevered beam based on the applied external magnetic field. The model also consists of unknown constants that will allow for this model to be extended to other combinations of filler and base materials. Experimental data is collected for two different H-MRE samples and used to verify the theoretical model, as well as determine the optimal values of the constants that should be used for accurate modeling.

Actuation Mechanisms in H-MRE Materials

As previously discussed, when the H-MRE samples were fabricated they were aligned within an electromagnet such that the magnetic particles had a desired orientation. By simply applying an external magnetic field to these oriented and properly constrained H-MRE samples, a motion will be induced that could be utilized in various capacities such as artificial muscles or energy harvesting. In order to properly implement H-MRE into actuator applications, it is crucial to determine their behavior when subjected to an external magnetic field. Extensive studies have been conducted on other smart materials, such as electroactive polymers and piezoelectrics, to generate accurate models of their bending characteristics based on an applied external stimulus [12, 13, and 14]. By developing accurate and extensive models for H-MRE materials, it will allow for this class of smart material to begin being utilized in actuation applications where precise tip control is necessary.

Before examining how best to model the bending of an H-MRE actuator, it is important to understand the mechanism by which these materials can be made to bend. As stated previously, an H-MRE is composed of a base elastomer material and a dispersion of hard magnetic particles that are cured under a strong magnetic field. This causes the magnetic particles within the base elastomer to become aligned in a certain direction since the magnetic moment of each particle will be forced into a certain direction during the curing process. This resulting alignment is shown above in Figure 1, as compared to another MRE material that has been fabricated without aligning the particles. The principles of magnetism state that when an external magnetic field is applied perpendicular to the magnetic moment of a material, a torque will be generated within the material. This relationship can be summarized with the following vector equation in Eq. (1) where $\vec{\mu}$ is the magnetic moment of the material, $\vec{B}$ is the applied magnetic field, and $\vec{\tau}$ is the resulting torque.

$$\vec{\tau} = \vec{\mu} \times \vec{B} \qquad\qquad (1)$$

Since the torque generated is based on the cross-product, if the magnetic moment and magnetic field are in the same direction then no torque will be generated and there will simply be a magnetic force/attraction imparted on the material. However, by mounting the H-MRE actuator in such a way that these two vectors quantities are in the proper direction, a torque will be created by each magnetic moment within the material. It is impossible to consider each individual torque within the material since there are a large number of particles (millions) within each sample, so instead the net torque applied to the material as a whole is considered. This principle is illustrated in Figure 4 demonstrating how the magnetized sample is oriented in the magnetic field to generate bending of the sample.
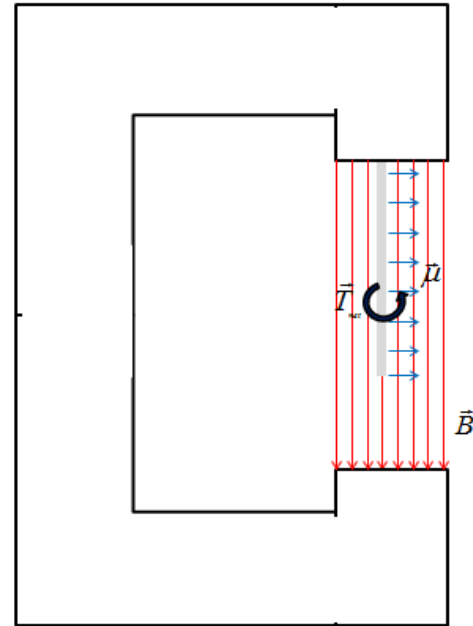
Figure 4: Illustration showing the H-MRE sample is oriented within an electromagnet and the resulting torque that is generated due to the applied magnetic field B.

Assumptions of the Model

In order to accurately model the physical bending of an H-MRE beam actuator, there are a few key assumptions that were made that are reasonable based on the fabrication methods and testing procedures for this study.

1) The material remains within the linear-elastic region of its stress-strain curve during the bending tests being conducted. This means that the stress developed within the material is linearly related to the strain through the Young's Modulus of the material, E_{MRE}. However, to simplify the analysis of this material it is assumed that the stress developed within the material is constant along the thickness of the beam. This assumption is reasonable because the thickness of the beam is small compared to the other geometric dimensions. In further modeling studies it would be worthwhile to consider a non-constant stress distribution and consider the implications of this on a model.

2) The material is assumed to be homogenous, with a dispersion of Neodymium particles within an elastomeric base, so that the mechanical properties of the material do not vary within the sample itself in any dimension.

3) The induced bending moment and resulting stresses within the beam are caused solely by the torque generated by the Neodymium particles as a result of the applied magnetic field. These stresses are also assumed to be only in the lateral direction.

Taking these assumptions into consideration, an experimental bending model was developed to predict the deflection of a beam based on the applied magnetic field.

Induced Internal Bending Moment

As discussed above the mechanism for the motion of this beam actuator is a result of the magnetization of the magnetic particles and applied magnetic field. Since the neodymium particles are aligned during the fabrication process, all of the individual torques they produce will be in the same direction. Therefore, it is possible to look at the net internal bending moment that is developed as the loading condition that causes the beam to bend under an applied magnetic field.

For the analysis of this model, is it assumed that the truly homogenous H-MRE sample can be thought of as two equivalent "layers", shown in Figure 5. As noted previously, a uniform stress distribution is assumed with the top layer experiencing compressive stress and the bottom layer experiencing tensile stress as a result of the applied bending moment. The magnitude of this bending moment can be found by determining the moment produced by the given stress distribution within the beam as shown in Eq. (2)

$$M = \int_A y \, dF = \int_A y \sigma \, dA \tag{2}$$

Using the given dimensions and properties of the stress distribution as shown in Figure 5 the resulting internal bending moment can be expressed in terms of the stress and geometric properties of the sample as follows:

$$M = \int_0^h \sigma y \, dA + \int_0^{-h} -\sigma y \, dA \rightarrow M = c\sigma \int_0^h y \, dy - c\sigma \int_0^{-h} y \, dy$$

$$M = \frac{c\sigma h^2}{2} - \left(-\frac{c\sigma h^2}{2}\right) = c\sigma h^2 \tag{3}$$
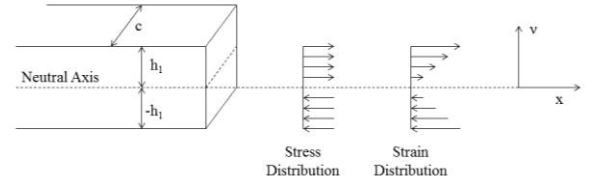
Figure 5: Image depicting the given geometric dimensions of the H-MRE actuator and the specified internal stress and strain distributions.

Based on the assumption that the applied magnetic field is solely responsible for causing stress in the material as a result of the torque created, it is easy to relate the stress developed in the material. However, there has not been previous work conducted to determine what type of relationship exists between the developed stress and applied magnetic field. Therefore it is important to introduce two constants, n and *(alpha)* in order to relate the stress and applied magnetic field. The constant α is introduced to allow the model to be applied to many different types of H-MRE based on different volume ratios and different base elastomers. The unknown constant n is introduced since the relationship between stress and applied magnetic field is not known, and may also change for different materials. The general form of the equation relating the stress developed to the applied magnetic field is given in Eq. (4)

$$\sigma = \alpha B^n \tag{4}$$

The direction of the stress is dependent on the interaction between the magnetization of the H-MRE sample and the direction of the applied magnetic field. Therefore, this equation simply predicts the magnitude of the stress and the direction would need to be identified based on information given for sample preparation. Substituting the relationship in Eq. (3) into Eq. (2) results in the following:

$$M = c\sigma h^2 \rightarrow M = c\alpha h^2 B^n \qquad (5)$$

Bending Curve Model

The second component of this model can then be derived under the assumption that the strain distribution within the material is linear. Using the method similar to that of previous modeling of smart materials [14] and Figure 6 as a reference, the strain can be expressed as shown below in Eq. (6)

$$\varepsilon = y \frac{d\theta}{dx} \qquad (6)$$

Where ε is the strain developed in the material, y is the distance from the neutral axis of the beam, $d\theta$ is the incremental bending angle of the actuator, and dx is an incremental element of the beam length. From, Hooke's Law we can further expend this equation to:

Figure 6: Expansion and contraction of the MRE beam for an incremental length dx.

$$\frac{\sigma}{E} = \varepsilon = y \frac{d\theta}{dx} \rightarrow \sigma_{MRE} = E_{MRE} y \frac{d\theta}{dx} \qquad (7)$$

The elastic modulus of the H-MRE sample is dependent both of the type of magnetic particle used as filler material as well as the base elastomer. Since no work has been previously completed regarding the stress-strain behavior (more specifically the Young's modulus) of the particular combination of elastomer and Neodymium particles, this quantity must be estimated using the rule of mixture. The rule of mixture for composite materials states that the elastic modulus is dependent upon the elastic modulus of the components as well as the ratio in which they are mixed as given in Eq. (8) [15]:

$$E_{MRE} = E_{Elastomer} V_{Elastomer} + E_{Filler} V_{Filler} \qquad (8)$$

Where $E_{Elastomer}$ is the elastic modulus of the base elastomer material, E_{Filler} is the elastic modulus of the filler particles, $V_{Elastomer}$ is the volume fill percentage of the base elastomer, and V_{Filler} is the volume fill percentage of the filler particles. Using this principle gives an upper limit for the elastic modulus of the material and should provide a reasonable estimate for the model. In the future, typical stress-strain tests can be conducted on samples of the H-MRE material to determine the elastic modulus more precisely.

The moment of inertia for the actuator also influences the bending of the actuator and depends upon the geometric dimensions and shape of the cross sectional area. The moment of inertia for each of the sections can be calculated using conventional formulas [16] and shown to be:

$$I_{MRE} = \frac{h^3 c}{3} \qquad (9)$$

Using this information, the internal bending moment can be related to the stresses and moments of inertia by the following:

$$M = \int_{A_{TOP}} \sigma y \, dA + \int_{A_{BOTTOM}} -\sigma y \, dA \rightarrow$$

$$M = c\sigma \int_0^h y \, dy - c\sigma \int_0^{-h} y \, dy = cE_{MRE} \frac{d\theta}{dx} \int_0^h y^2 \, dy - cE_{MRE} \frac{d\theta}{dx} \int_0^{-h} y^2 \, dy$$

$$M = cE_{MRE} \frac{d\theta}{dx} \left(\int_0^h y^2 \, dy - \int_0^{-h} y^2 \, dy \right)$$

$$M = cE_{MRE} \frac{d\theta}{dx} \left(\frac{2h^3}{3} \right) = 2E_{MRE} \frac{d\theta}{dx} \left(\frac{h^3 c}{3} \right)$$

$$M = 2E_{MRE} I_{MRE} \frac{d\theta}{dx} \qquad \textbf{(10)}$$

The equation presented in Eq. (10) above includes the relationship between the incremental bending angle $d\theta$ and an incremental element of length dx. However, for many of the applications mentioned it is important instead to control the incremental vertical deflection dv in terms of the incremental length dx. Using the diagram shown in Figure 7 the following relationship can be observed:
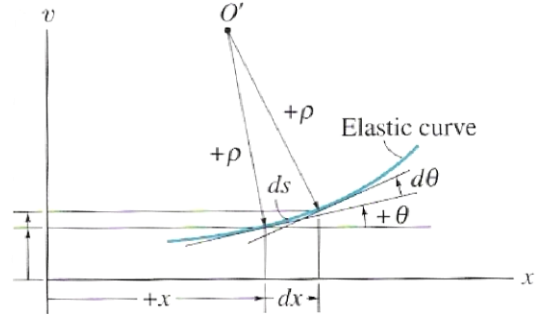
Figure 7: Relationship between the curvature of the beam and the vertical deflection for an incremental length, dx [16].

$$\theta = \arctan\left(\frac{dv}{dx} \right) \qquad \textbf{(11)}$$

Differentiating this relationship with respect to the incremental length element dx gives Eq. (12):

$$\frac{d}{dx}\left[\theta = \arctan\left(\frac{dv}{dx} \right) \right] \rightarrow \frac{d\theta}{dx} = \frac{\dfrac{d^2 v}{dx^2}}{1+\left(\dfrac{dv}{dx} \right)^2} = \frac{v''}{1+(v')^2} \qquad \textbf{(12)}$$

Substituting Eq. (12) into Eq. (10):

$$M = 2E_{MRE} I_{MRE} \frac{d\theta}{dx} \rightarrow M = 2E_{MRE} I_{MRE} \frac{v''}{1+(v')^2} \qquad \textbf{(13)}$$

This equation demonstrates that the moment is dependent on the second derivative of the vertical deflection with respect to the length. This is consistent with conventional beam theory as presented in [9]. Equating Eq. (13) and Eq. (5):

$$M = 2E_{MRE}I_{MRE}\frac{\upsilon''}{1+(\upsilon')^2} = c\alpha h^2 B^n \rightarrow$$

$$\frac{\upsilon''}{1+(\upsilon')^2} = \frac{c\alpha h^2 B^n}{2E_{MRE}I_{MRE}} \tag{14}$$

In order to solve this non-linear second order differential equation, it needs to be rearranged in the following manner.

$$\frac{\upsilon''}{1+(\upsilon')^2} = \frac{c\alpha h^2 B^n}{2E_{MRE}I_{MRE}} \rightarrow \upsilon'' = \frac{c\alpha h^2 B^n}{2E_{MRE}I_{MRE}}\left[1+(\upsilon')^2\right] \rightarrow$$

$$\upsilon'' - \frac{c\alpha h^2 B^n}{2E_{MRE}I_{MRE}}\left[1+(\upsilon')^2\right] = 0$$

$$\upsilon'' - \frac{c\alpha h^2 B^n}{2E_{MRE}\left(\frac{ch^3}{3}\right)}\left[1+(\upsilon')^2\right] = 0 \rightarrow \upsilon'' - \frac{3\alpha B^n}{2E_{MRE}h}\left[1+(\upsilon')^2\right] = 0 \tag{15}$$

There is no straight-forward method to solve for the deflection of the beam as a function of the horizontal distance *v(x)* so this equation must be solved numerically using a system of linear first-order ordinary differential equations (ODE). The system of equations used for solving this non-linear second differential equation using the MATLAB ode45 function is shown below:

$$\text{Let } q_1 = \upsilon \text{ and } q_2 = \upsilon'$$

$$q_2 = q_1' \tag{16}$$

$$q_2' - \frac{3\alpha B^n}{2E_{MRE}h}\left[1+q_1^2\right] \tag{17}$$

Experimental Testing/Sample Preparation

The focus of this study is verifying that this beam model can be applied to individual H-MRE samples with different base and filler materials being used for fabrication. The samples were prepared in-house at Miami University using Neodymium particles and Dow Corning silicon base elastomer materials [17]. The fabrication of the samples was performed using the following process:

1) Measure necessary quantities of neodymium particles and base material for desired volume ratio and mix thoroughly.

2) Add catalyst in necessary ratio as specified by the manufacturers recommendations and mix until mixture is homogenous

3) Pour material into mold and place in electromagnet under a magnetic field of 1.5 T for approximately one hour in the proper orientation. Remove from electromagnet and allow to the sample to cure for an additional 24 hours before removing it from the mold.

4) Cut the sample to the desired dimensions

For this study, samples were prepared with a thickness of 3 mm, a width of 14 mm, and a length of 52 mm. It should be noted that the real length of the beam was taken to be 50 mm since the mounting device required 2 mm of the sample to be inserted in order to properly constrain it. The filler material used was neodymium particles mixed with Dow Corning HS II and HS IV base elastomers. The volume ratio for each of the samples was chosen to be 30%, since this has been shown to be the optimal volume fill percentage for MRE materials in previous studies [11]. The mechanical properties of these materials were such that E_{Neo}=41.9 GPa [18] and the elastic modulus of the two elastomers were estimated as $E_{Elastomer}$=0.76 MPa and $E_{Elastomer}$=0.36 MPa for HS II and HS IV, respectively. The fabricated and cut samples are shown below in Figure 8.

An electromagnet and mounting mechanism were fabricated as shown below in Figure 9 so that the H-MRE sample could be mounted vertically and suspended from the electromagnet in order to neglect the effects of bending due to its own weight as much as possible. The deflection in the v direction was measured with a LK-G150 laser displacement sensor from Keyence Corporation. Measurements were taken along the length of the beam at increments of 2 mm in order to plot the bending curve of the sample. Since an electromagnet was used, it was possible to only control the current applied and tests were conducted at applied current of 0-1.5A in increments of 0.25 A. The correlation between the current and magnetic field as used in the model is discussed below.
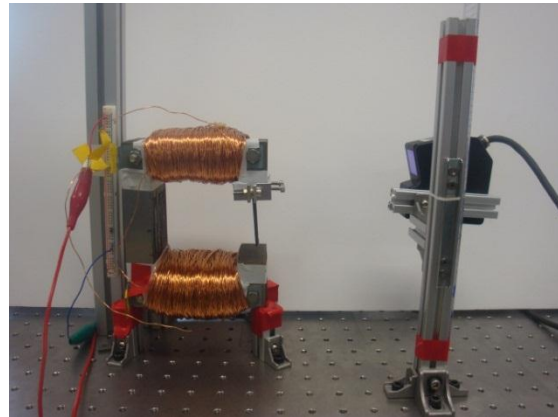
Figure 8: Image of the fabricated H-MRE samples used for experimental testing of the developed beam model.

Figure 9: Experimental test set up with the H-MRE mounted in the electromagnet (left) and the laser displacement sensor mounted to measure horizontal distance (right).

Magnetic Field Considerations

The model for predicting the bending characteristics of H-MRE beams assumes that a constant magnetic field is applied across the material. However, with any type of electromagnet, there are certain losses that lead to a magnetic field gradient developing between the two surfaces of the electromagnet. The gradient was measured using a Gaussmeter and an experimental model was developed that predicts the magnetic field flux as a function of the current and distance from the top surface of the electromagnet.
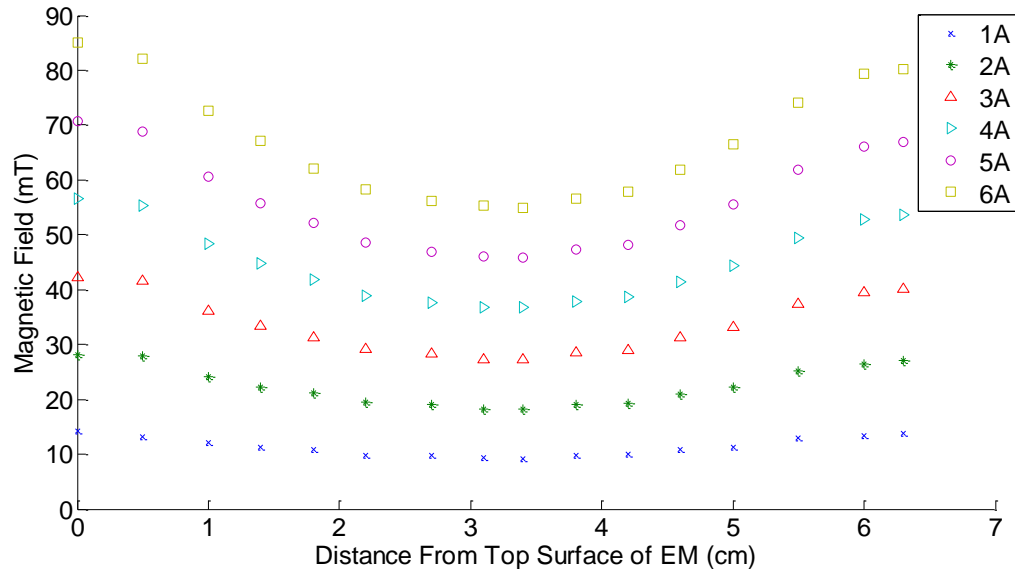
Figure 10: Experimental results of measuring the magnetic field inensity (in mT) between the two surfaces of the electromagnet and demonstrating the loss of flux density that occurs.
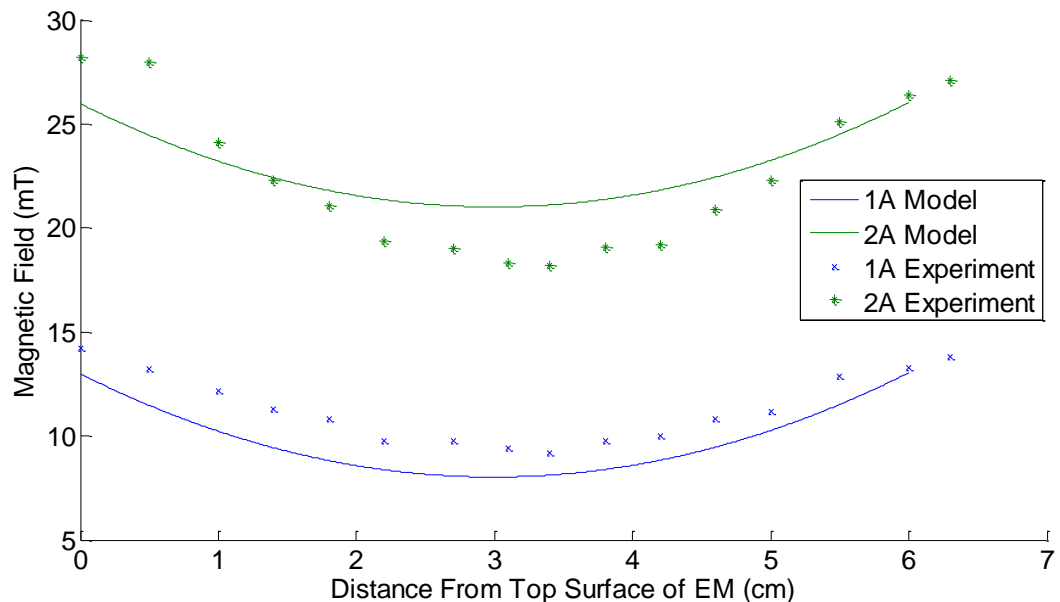
Figure 11: Experimental and model results for the magnetic flux density for an applied current of 1 A and 2 A. The coefficient of determination for this model is r^2=0.9903, indicating a very strong fit of the model.

Figure 10 demonstrates that there is a clear gradient in the magnetic field between the two surfaces of the electromagnet and also changes with applied current. It can be seen that the higher the applied current is, the larger the difference in magnetic field between the middle of the gap and the electromagnet surface. There is a difference of approximately 25 mT for an applied current of 6 A and only a difference of approximately 7 mT for an applied current of 2 A. Since, these samples are only being observed between 0-1.5 A it is reasonable to simply use an average value of the magnetic field in the model since there are only small differences observed. Average values are determined by the model generated using R statistical software and the measured values for the magnetic flux. Figure 11 shows the fit of this model for the range of currents that are applied during the experimental testing of the H-MRE beam. The average values used for applied currents, as predicted by the model, are presented in Table 1.

Table 1: Relationship between the current supplied to the electromagnet and the average magnetic field across the H-MRE sample as calcualted from the plots above.

Applied Current (A)	Average Magnetic Field (mT)
0.25	0.1394
0.5	3.3867
0.75	6.6340
1.00	9.8812
1.25	13.1285
1.50	16.3758

Experimental Results

Measurements were conducted on the deflection of the beam for different applied currents (varying magnetic fields) and the results are shown below in Figure 12 for HS II and in Figure 13 for HS IV.
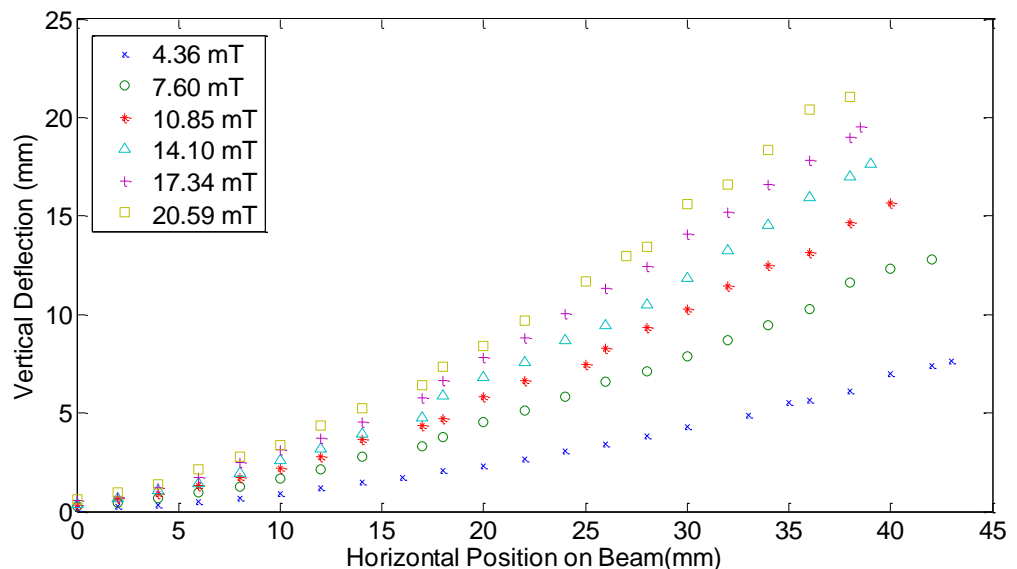
Figure 12: Experimental bending curve results for HS II H-MRE sample with 30% volume fill of neodymium particles.
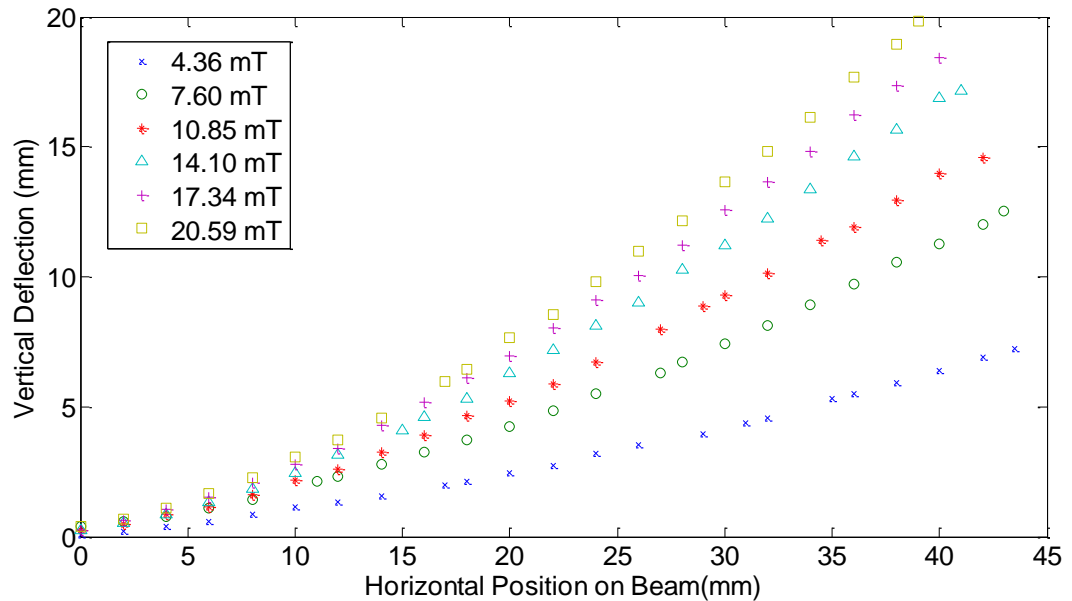
Figure 13: Experimental bending curve results for HS IV H-MRE sample with 30% volume fill of neodymium particles.

These figures demonstrate that there is a nonlinear relationship between the vertical displacement and horizontal position on the beam as predicted by the theoretical model developed for H-MRE beams. It is also evident that there is a non-linear relationship between the vertical deflection between and the magnetic field at a given horizontal distance. The nature of this change, the rate of change in the vertical deflection decreasing with increasing magnetic field, indicates that the constant *n* in the theoretical model should have a value less than one. This trend is observed for both of the base materials indicating that this relationship exists for all types of MRE materials.

There is also a difference between the responses for the two different materials as a result of their varying mechanical properties. This difference is not very pronounced since the combined elastic modulus of the H-MRE is largely dominated by the Neodymium particles but there is some difference that will be explored in the determination of the constants in the following section.

Optimization of Model Parameters

In order to determine if the model and experimental results are consistent, the constants α and *n* need to be chosen so that the resulting prediction is as accurate as possible. One method that can be used to choose these constants is to pick them such that the sum of the squared residuals is minimized. The residuals are defined as the difference between the measured value and predicted value. These values can be positive or negative so it is important to consider their squared values when trying to minimize this quantity. This technique is the one that is employed in most linear regressions so it seems reasonable to apply it to the non-linear model.

There is no straightforward method to determine how to pick these constants so the MATLAB function `fminsearch` was employed to optimize the parameters and minimize the sum of squared residuals. This function uses an algorithm (far beyond the scope of this paper) that cycles through different combinations of parameters to try and minimize the value of interest based on certain boundaries given to the parameters. Initially, it was the intention of this study to

try and determine one value of α that applied for each combination of filler material and base elastomer. Using the optimization method described above, constraints were placed on the value of *n* between 0 and 1, and the value of α between 1e7 and 1e9 (based on the units of the other parameters used in this study). Using the optimization parameters the sum of squared residuals was minimized for a value of *n*=1.0 and *α*=1e7. As can be seen from Figure 14, although the sum of squared residuals is minimized for this one value of alpha, there is not a very good fit of the theoretical curves to the experimental data for any applied current. Even when using other algorithms to try and improve the fit of the curves, there did not seem to be one global value for *α* that could be used for every modeling scenario for a particular material.
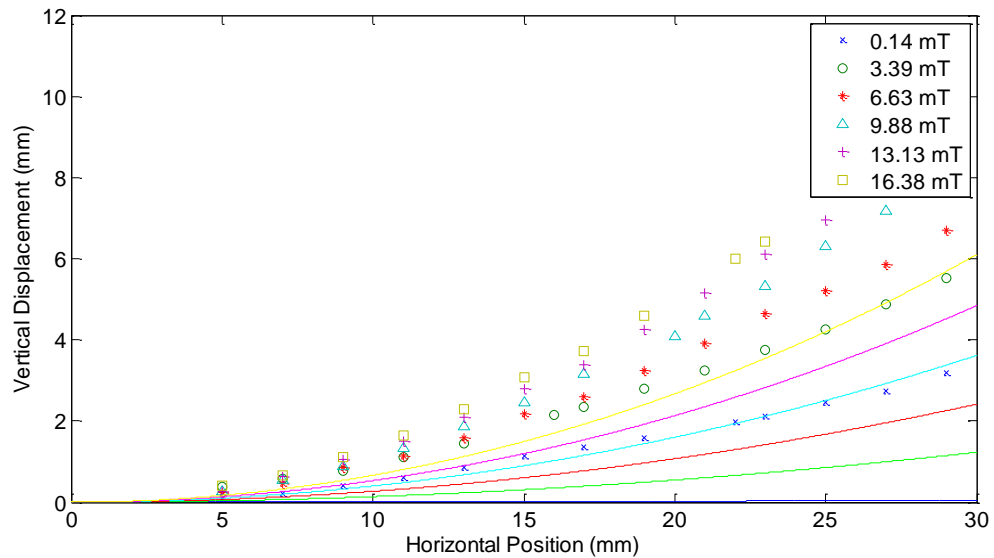
Figure 14: Results of first optimization iteration to determine one universal value of the constants. For this model α=1e7 and n=1.0.

This implied that the coefficient α included in this model actually accounted for more than just the mechanical properties of the MRE material, perhaps also being a function of the magnetic field, or even the magnetic field distribution. If the coefficient α is simply a function of the magnetic field, then it would be possible to add some sort of multiplier into the model in order to change this value based on the applied magnetic field. In an effort to identify this trend, value for the coefficient α were calculated over a wide range of values of the parameter *n* to determine if some relationship existed between the unique values of α for each different applied magnetic field. However, there was no clear relationship between the values of α for different applied magnetic fields and indicated that this value most likely also accounts for the magnetic field gradient that occurs along the length of the beam.

In order to identify the proper value of α for a given power *n*, many iterations of the optimization were performed with different fixed values of *n* and 6 unique α values were obtained. It was then determined that the combination of *n* and *α* that resulted in the lowest sum of square residuals should be used as the best indication of modeling the observed physical behavior of the H-MRE samples. The optimized values for *α* for each different applied magnetic field and power value are included below in Table 2 for HS IV and HS II respectively. The sum of square error was calculated for each different combination and it was determined that the best values of the

unknown parameter *n* are *n* =0.75 for HS IV and *n* = 0.60 for HS II. These results are also shown graphically with the experimental data in Figure 15 for HS IV and Figure 16 for HS II.

Table 2: Optimized Alpha Values for Varying Values of *n* for HS IV

Magnetic Field (B)	0.14 mT	3.39 mT	6.63 mT	9.88 mT	13.13 mT	16.38 mT
Power (n)						
0.50	2.15E+08	7.49E+07	6.56E+07	6.37E+07	6.12E+07	5.91E+07
0.55	2.38E+08	7.05E+07	5.96E+07	5.68E+07	5.38E+07	5.14E+07
0.60	2.62E+08	6.63E+07	5.43E+07	5.06E+07	4.73E+07	4.47E+07
0.65	2.89E+08	6.24E+07	4.94E+07	4.52E+07	4.16E+07	3.89E+07
0.70	3.19E+08	5.87E+07	4.49E+07	4.03E+07	3.66E+07	3.38E+07
0.75	**3.53E+08**	**5.52E+07**	**4.08E+07**	**3.59E+07**	**3.22E+07**	**2.94E+07**
0.80	3.89E+08	5.20E+07	3.72E+07	3.20E+07	2.83E+07	2.55E+07
0.85	4.29E+08	4.89E+07	3.38E+07	2.86E+07	2.49E+07	2.22E+07
0.90	4.74E+08	4.60E+07	3.08E+07	2.55E+07	2.19E+07	1.93E+07
0.95	5.23E+08	4.33E+07	2.80E+07	2.27E+07	1.92E+07	1.68E+07
1.00	5.77E+08	4.07E+07	2.55E+07	2.03E+07	1.69E+07	1.46E+07

Table 3: Optimized Alpha Values for Varying Value of *n* for HS II

Magnetic Field (B)	0.14 mT	3.39 mT	6.63 mT	9.88 mT	13.13 mT	16.38 mT
Power (n)						
0.50	2.24E+08	8.08E+07	7.37E+07	6.92E+07	6.67E+07	6.59E+07
0.55	2.47E+08	7.61E+07	6.70E+07	6.17E+07	5.88E+07	5.73E+07
0.60	2.73E+08	7.16E+07	6.10E+07	5.50E+07	5.17E+07	4.99E+07
0.65	3.01E+08	6.73E+07	5.55E+07	4.91E+07	4.55E+07	4.33E+07
0.70	3.32E+08	6.33E+07	5.05E+07	4.38E+07	4.00E+07	3.77E+07
0.75	3.67E+08	5.96E+07	4.59E+07	3.90E+07	3.52E+07	3.28E+07
0.80	4.05E+08	5.61E+07	4.18E+07	3.48E+07	3.09E+07	2.85E+07
0.85	4.46E+08	5.27E+07	3.80E+07	3.10E+07	2.72E+07	2.48E+07
0.90	4.93E+08	4.96E+07	3.46E+07	2.77E+07	2.39E+07	2.16E+07
0.95	5.44E+08	4.67E+07	3.15E+07	2.47E+07	2.10E+07	1.87E+07
1.00	6.00E+08	4.39E+07	2.86E+07	2.20E+07	1.85E+07	1.63E+07
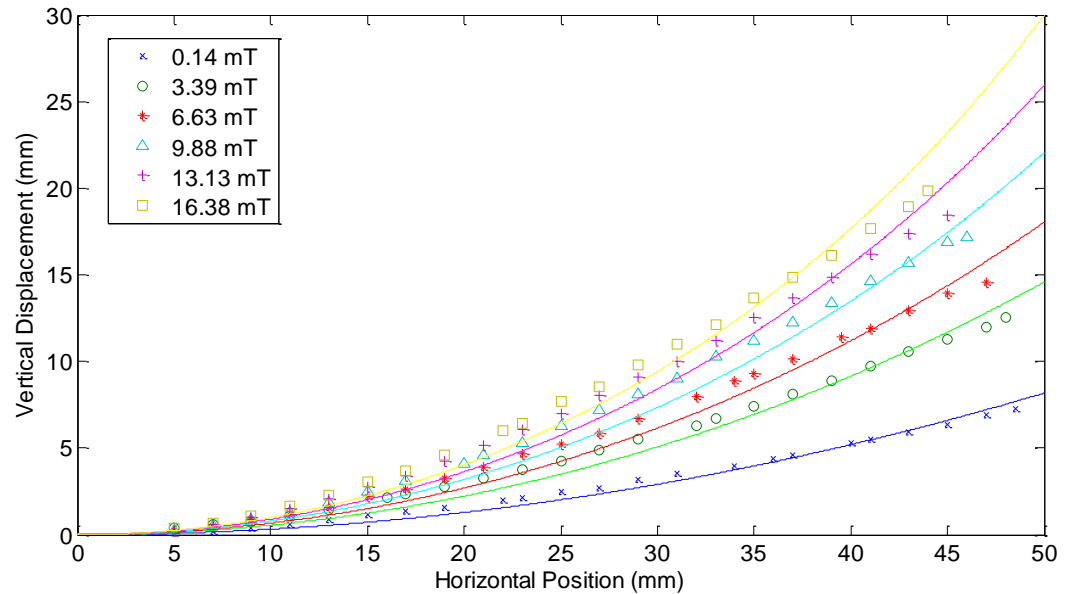
Figure 15: Optimization results for HS IV neodymium samples with different values of alpha and a value of n=0.75
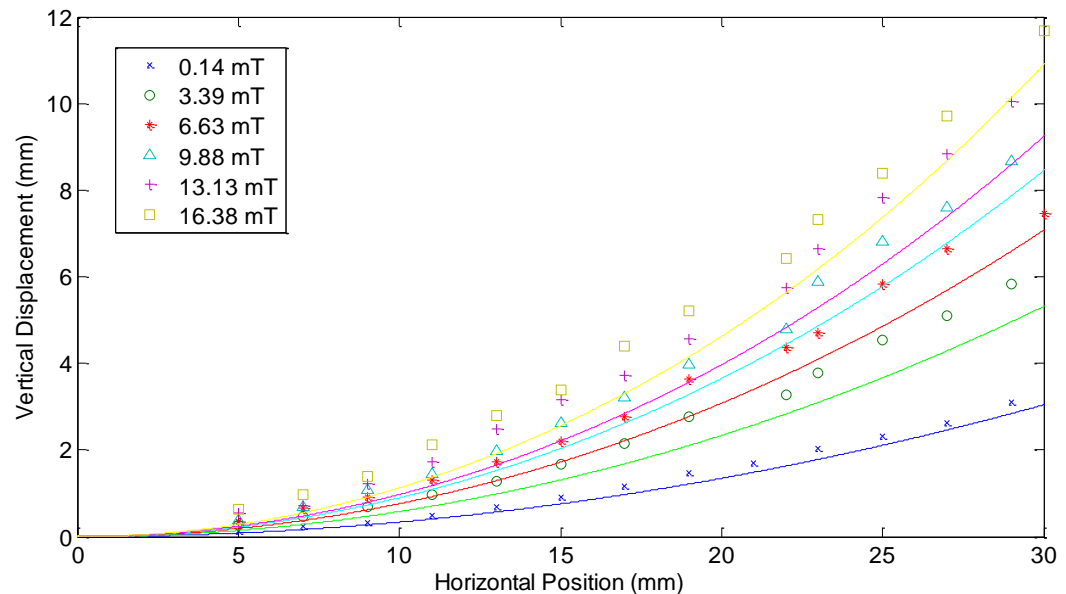
Figure 16: Optimization results for HS II neodymium samples with different values of alpha and a value of n=0.60

Further Model Optimization – Regression Approach

After conducting the initial model optimization methods as described previously, it was determined that there was no single value of α that could be used to capture the entire behavior of the different samples in bending. It was hypothesized that instead of this being simply a material property, that this value could be dependent on the applied magnetic field of the material. Therefore it was desirable to try and fit some sort of regression model to the optimal value obtained for α as a function of the applied magnetic field. In order to get a better idea of the

nature of the relationship (linear, quadratic, exponential, etc.), the alpha values as a function of the magnetic field were plotted and the relationship was observed (omitted for brevity).

By inspection, it was clear that the first data point in each case corresponding to an applied magnetic field of 0.14 mT was an outlier. This is evident above in Table 2 and Table 3, as well, since the alpha values obtained were always significantly higher than for any other of the applied magnetic fields. Therefore, before beginning the model selection process, this data point was discarded as it would be very influential in the overall model selection and determination of the model parameters. After discarding the data point, similar plots were constructed and it was evident that the relationship was improved. It was still difficult, however, to determine what type of model would be most appropriate for this modeling exercise. The relationship did appear quadratic in nature, but in order to be sure of these relationships, three different models were assessed. These models were a quadratic model, a cubic model, and a quartic model having the regression forms presented below in Eq. (18) – Eq. (20), respectively. Using these models and statistical software SAS [19], the coefficients for each term and corresponding coefficients of determination are presented below in Table 4. Additionally, the superimposed plots of these different models along with the raw data points are shown below in Figure 17 and Figure 18 for HS II and HS IV, respectively.

$$\alpha = p_1 B^2 + p_2 B + p_3 \tag{18}$$

$$\alpha = p_1 B^3 + p_2 B^2 + p_3 B + p_4 \tag{19}$$

$$\alpha = p_1 B^4 + p_2 B^3 + p_3 B^2 + p_4 B + p_5 \tag{20}$$

Table 4: Regression coefficients determined from modeling alpha values as a function of applied magnetic field.

HS II	Model	p_1	p_2	p_3	p_4	p_5	Coefficient of Determination,
	Quadratic Regression	1.655E5	-5.124E6	6.969E7	-	-	0.9797
	Cubic Regression	-2.101E4	7.887E5	-1.053E7	8.254E7	-	0.9978
	Quartic Regression	3015	-1.402E5	2.415E6	-1.939E7	9.825E7	1
HS IV							
	Quadratic Regression	1.377E5	-4.345E6	8.442E7	-	-	0.9968
	Cubic Regression	-7625	3.638E5	-6.307E6	8.908E7	-	1.0000
	Quartic Regression	277.3	-1.859E4	5.134E5	-7.121E6	9.053E7	1
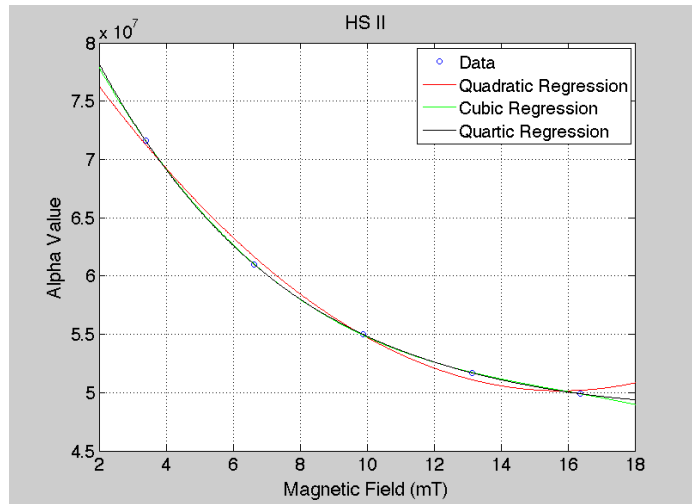
Figure 17: Regression modeling results for HS II.
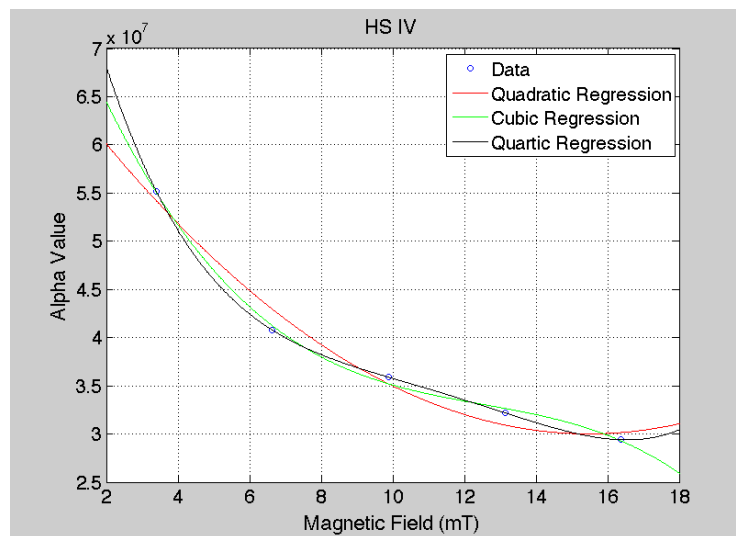
Figure 18: Regression modeling results for HS IV

Based on the results presented in Table 4 above, it is clear that all of these models tend to provide an excellent fit to the raw data. In order to choose the best model, the coefficient of determination is a good measure of goodness of fit as it explains the percentage variation of the response variable due to the independent variable. For all of the cases presented above, these values are well over 97% meaning they all have a very good fit. Therefore, another criteria used to determine the best model to use would be the degrees of freedom remaining after applying a certain model. When one continues to use higher order models (quartic and above) the coefficient of determination will ultimately increase since every change in the data can be accounted for by addition of higher order terms. However, this takes away from the degrees of freedom of the model and actually increases the error within these estimates. Therefore, it is recommended to choose the lowest order model, which in this case would be the quadratic regression since this provides an excellent fit to the data while still allowing for a sufficient number of degrees of freedom. Substituting this new value in for α from the original model in Eq. (15) would augment the model as shown below in Eq. (21).

$$\upsilon'' - \frac{3\left(p_1 B^2 + p_2 B + p_3\right)B^n}{2E_{MRE}h}\left[1 + (\upsilon')^2\right] = 0 \qquad\qquad \textbf{(21)}$$

Bending Model Conclusions
An experimental model was developed that serves to predict the bending motion of an H-MRE beam actuator based on the material properties and applied magnetic fields. The following conclusions can be drawn based on the results and discussion presented:

(1) The theoretical model developed for an H-MRE actuator is based on a few simple and reasonable assumptions and can be extended to any H-MRE with varying geometric dimensions and mechanical properties by including two simple unknown constants α and n.

(2) The results of experimentation show that there is a nonlinear relationship between the vertical deflection of the actuator and the applied magnetic field at a given horizontal position along the beam. In fact, the change in deflection decreases as the magnetic field is increased, indicating that a constraint of the model is that the unknown parameter n is less than 1.

(3) By placing simple constraints on the unknown parameters α and n, values can be chosen using optimization algorithms that minimize the square of the difference between the observed values and predicted values. The results of this work have shown that is difficult to predict a uniform value of α and n that apply to all of the different applied magnetic fields for a given material. The reason for this is hypothesized to be that part of the H-MRE sample extended outside of the plane of the electromagnet, thus being subjected to a lower magnetic field. Since the model assumes a uniform magnetic field is applied to the sample, this would change the loading and suggests a different model should be pursued and developed that incorporates the presence of a magnetic field gradient across the beam.

(4) After going back and observing the different values observed for α, it was determined that there may be some further relationship between this constant and the magnetic field. After choosing the appropriate regression model, the relationship between these two parameters was determined and the model was adjusted to simply be a function of the magnetic field and the parameter n.

Future Work
Although this study presents a comprehensive and adequate model for predicting the behavior of H-MRE materials as actuators, there is still much work to be done in terms of further characterization of the material. Some of these topics include:

(1) Verifying this model for samples of different dimensions and different mechanical properties to ensure that the generalizations made in terms of geometry and mechanics (Young's modulus) are valid. This will involve following the same experimental procedure as outlined above and simply optimizing the unknown

constants for these cases. This will also help determine if the constant α is solely influence by the material, or if the geometry is important as well.

(2) Develop a new test setup that will apply a uniform magnetic field across the H-MRE sample in order to try and determine a universal of *n* and *α* for a given material using the optimization methods discussed.

(3) Create a model for the blocking force of an H-MRE actuator in terms of its mechanical properties and its geometry. The blocking force is important for actuation applications because it quantifies the amount of force an actuator could provide and indicates how effectively the material can convert magnetic energy into mechanical energy.

(4) An extensive study into the mechanical properties of H-MRE materials themselves can be conducted in order to better characterize the stress-strain relationship as well as other important quantities such as Young's modulus, tear strength, ultimate tensile strength, etc.

Blocking Force Experimentation and Modeling

After investing the displacement developed within these H-MRE actuators, it was then important to study the blocking force that these material are capable of producing when actuated. The blocking force of an actuator is defined as the force required to be placed on the tip of the actuator to prevent any motion. A number of studies have looked at blocking forces for other smart actuators [9, 10], particularly for piezoelectric materials, demonstrating it is an important quantity to consider when evaluating the overall performance of a material for use as an actuator in future applications.

Whereas the overall goal of the displacement study was to determine if the samples behaved according to conventional beam theory and develop a workable model, this portion of the study focused on examining the relationships between sample variables and blocking force. Many of the articles reviewed for this portion of the project [20] looked at how the blocking force can be derived theoretically based on the forces/torques imported on the actuators. For H-MRE samples, the torque placed on the actuator is a function of the magnetic field as seen in Eq. (1). Using this information, the equivalent force developed at the tip can be calculated by simply relating the length of the sample to the net torque placed on the sample. However, it is difficult to quantify this torque using current lab equipment since there is no capability of measuring the magnetic dipole of individual particles or even the sample as a whole.

Due to these restrictions, it was determined that it is more important to observe the trends in the blocking force as a function of different sample variables. The particular variables of interest were the volume-fill percentage of magnetic particles and the base elastomer used (all had different stiffness values) in each sample. After examining the trends of these variables, an attempt at fitting an adequate model for predicting the blocking force was developed for use in future actuator applications. This model was simply based on interpretation of the data and trying to quantify how the volume fill percentage of the H-MRE and the stiffness of the base elastomer used influenced the blocking force.

Experimental Testing/Sample Preparation

The samples utilized in this experiment were also prepared in-house at Miami University using Neodymium particles and Dow Corning silicon base elastomer materials [10]. The fabrication of the samples was performed using the same process discussed in the displacement modeling section of this report, however, the dimensions varied from the previous experiment. For this study, samples were prepared with a thickness of 3 mm, a width of 35 mm, and a length of 52 mm as shown in Figure 19. It should be noted that the real length of the beam was taken to be 50 mm since the mounting device required 2 mm of the sample to be inserted in order to properly constrain it. The filler material used was neodymium particles mixed with Dow Corning HS II, HS III, and HS IV base elastomers. The properties of each of these different base elastomers as provided by Dow Corning [17] are included below in Table 5.

Table 5: Properties of Dow Corning base elastomers used in sample fabrication.

Elastomer Name	Specific Gravity	Durometer Hardness (Shore A)	Tensile Strength (psi)	Percent Elongation (%)	Estimated Stiffness (psi)[1]
HS II	1.21	16	550	500	110
HS III	1.16	10	400	550-575	71.111
HS IV	1.16	5	350	675	51.85

[1]Dow Corning does not conduct tests directly on the elastic modulus, but through contact with their engineers, they utilize the following formula in Eq. (22) to calculate the stiffness of an elastomer:

$$E = \frac{UTS}{0.01(\% Elongation)} \qquad\qquad \textbf{(22)}$$

The same electromagnet that had been fabricated for the displacement testing was again utilized for these tests so that the samples were mounted vertically and negated the effects of gravity on the blocking force. In order to measure the blocking force, a load cell was placed directly at the tip of the H-MRE sample and prevented motion that was observed in the displacement experiments, resulting in a net blocking force applied to the load cell. For this experiment, nine total samples were evaluated in order to adequately determine the relationship between the volume fill percentage and stiffness with the resulting blocking force. Each of the three base elastomers were used to fabricate three samples with varying volume fill percentages of 10%, 20%, and 30% neodymium particles. Measurements of the blocking force were taken by applying currents to the electromagnet ranging from 0 A to 8 A, which in terms of the magnetic field was approximately 0 – 105 mT. The resulting force in units of kgf (1 kgf = 9.8 N) was measured and recorded for each of the different samples. Each of the tests was conducted two times to ensure the accuracy of the measurements and provide more data points to be used in the regression modeling to follow. The experimental set-up showing the location of the load cell relative to the H-MRE sample is pictured below in Figure 20.
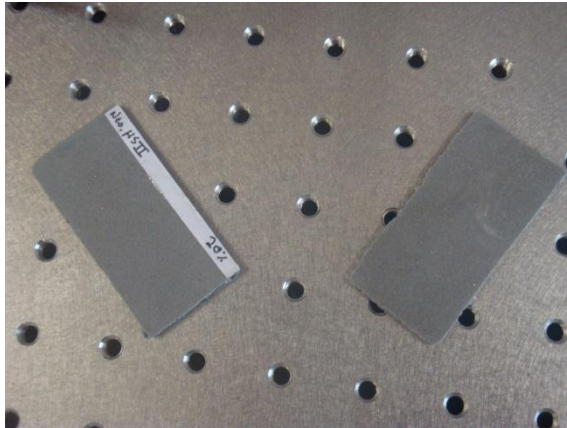
Figure 19: Image showing a few of the samples used in the blocking force experiments that were larger in size than those used in the displacement experiments.
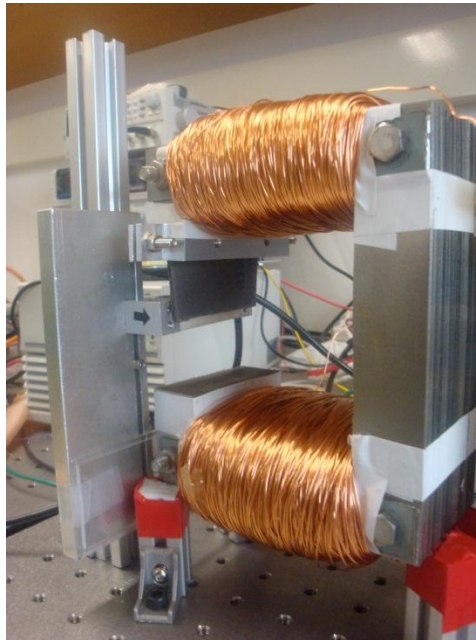
Figure 20: Experimental set-up for the blocking force experiments showing the H-MRE sample affixed to the electromagnet and the load cell placed to measure the blocking force at the tip of the actuator.

Experimental Results

The experiments were conducted as specified above in order to determine the trends in the blocking force of the samples as a function of both the volume fill percentage of magnetic particles and the stiffness of the base elastomer. A complete set of plots illustrating the results of these experiments are included in Appendix A for the reader's reference, with the results summarized as follows:

(1) For a given base elastomer, the blocking force increased in magnitude as the volume fill percentage of magnetic filler particles increased. This result is verified from the theoretical behavior of the material as higher volume fill percentages will

have greater net magnetization and a greater torque will be developed in the material as it bends.

(2) For a given volume fill percentage, there are a few trends that can be observed, as well as a few anomalies in the data:

o For every volume fill percentage, HS IV produced the lowest magnitude blocking forces. This is expected since HS IV is the softest material and could deform the easiest when contacting the load cell, resulting in reduced blocking force.

o It is difficult to distinguish between HS II and HS III for which one consistently has the largest blocking force since that varies depending on the volume fill percentage. This indicates that there could be some error with the actual fill percentage of the sample, or that they are two similar of an elastomer to realize any noticeable difference on this scale.

(3) The magnitudes of these forces are at most 0.16 kgf, indicating that actuators this size could impart of force of only around 1.5 N. However, by varying the size of the actuator as well as the volume fill percentage of the material, this value could be increased or decreased depending on the particular application.

Blocking Force Model Development

After conducting the experiments and interpreting the results, it was determined that an attempt at fitting a model to predict the blocking force of an H-MRE actuator. This model would be based solely on the experimental data of these findings and be some function of the blocking force, stiffness of the base elastomer, as well as the applied magnetic field. The model fitting process was rather straightforward as it used classical regression techniques to minimize the sum of squared errors to find the best values for the unknown coefficients. In looking to optimize the coefficients of this model, the first step was to look individually at each of the different types of materials to see if there was any obvious relationship between the blocking force and volume fill percentage (linear, quadratic, etc.) and determine if this was consistent for all of the materials. The model used had the following form presented in Eq. (23)

$$\hat{y} = \beta_1 x_1 + \beta_2 x_2^{\alpha} + \beta_3 x_1 x_2^{\alpha}$$

(23)

x_1: Applied Current in mA
x_2: Volume Fill Percentage of Neodymium Particles
α: Unknown Power of Volume Fill Percentage to Use

Looking at scatter plots of the data, one can clearly see there is a linear relationship between the applied current and blocking force. This makes sense because the magnetic field increases linearly with current, as does the net torque applied to the total sample. However, the scatter plots also revealed there was some relationship between the blocking force and the volume fill percentage that appeared to be different for each of the materials. In was clear this relationship was not linear, but it was difficult to judge just from visual inspection if it were a quadratic relationship, a cubic one, or some unknown power function. Therefore, it was determined that an unknown exponent α should be included in the model that could be used to determine this

relationship. In order to determine the optimal value for this parameter, the sum of square residuals needed to be minimized since it is the criteria for selecting the "best" model in most regression applications. As can be seen in the plots depicted in Figure 21, this minimum value of α was not consistent for each material and varied by material as indicated in Table 6

Table 6: The following table shows the optimal values of α for the initial blocking force models.

Material Name	Material Stiffness (psi)	Optimal Value of α
HS II	110	1.39
HS III	71.111	3.37
HS IV	51.85	1.90

After determining these values for α, the observed values and fitted vales were plotted against one another to determine whether these fits were appropriate for each of the data sets. An example of these plots for HS II is included below in Figure 22 and Figure 23, which demonstrates that the fit of this model with independent coefficients for each material is valid as there is little variation between the experimental and fitted values.
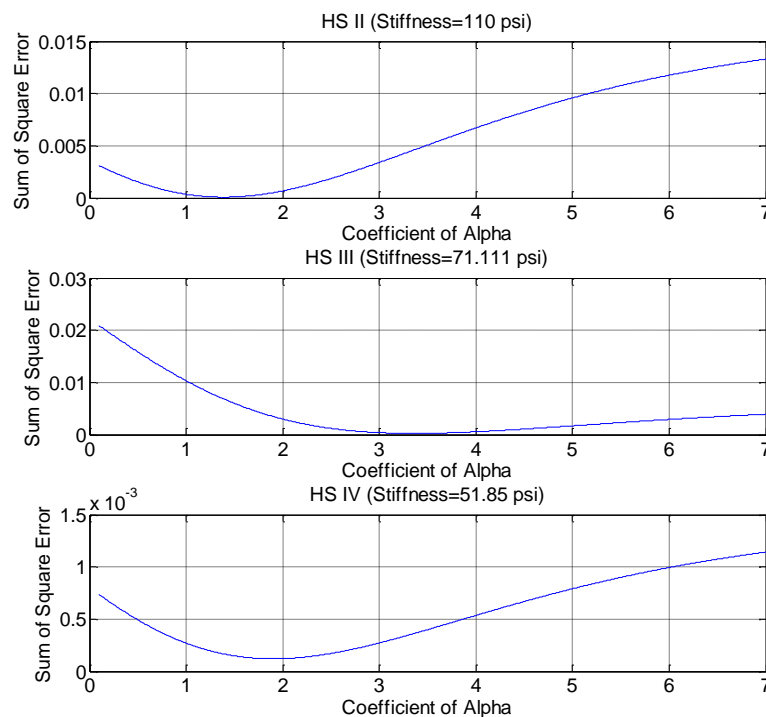

Figure 21: Plot showing the different minimized values of ALPHA to be used in the initial blocking force model form.
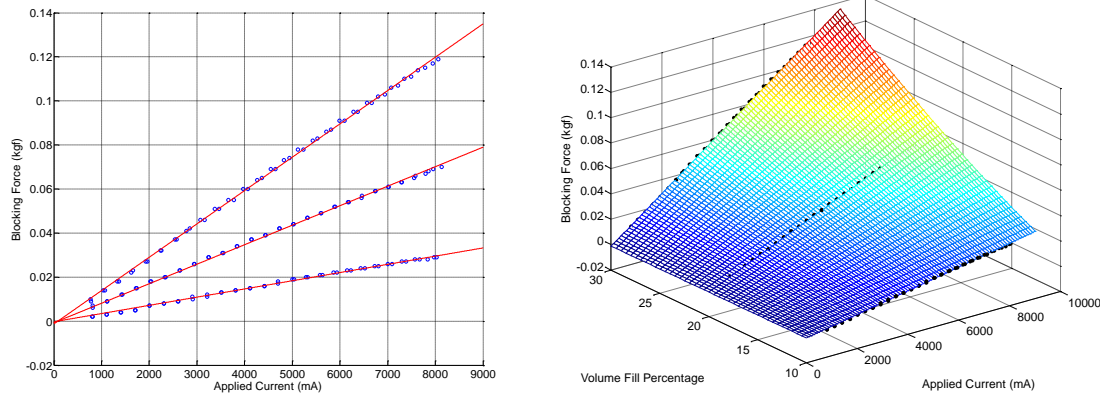
Figure 22: Plot showing the fit of the individualized model for HS II.

Figure 23: 3D plot showing the fit of individualized model for HS II.

Upon looking at the results for the regression models fit to the individual materials, it is clear that there is a good fit between the model and the experimental data. However, the overall goal of this study is to quantify the blocking force for H-MRE samples in general and ideally develop a model in which the material properties of the sample are also taken into consideration. The model with only the individual values would be valid; however, a new model would need to be fit for every different base elastomer that is used to fabricate an H-MRE actuator. Instead, information about the base elastomer should be included in the mode to allow for the development of a more global model appropriate for all H-MRE samples. The global model that was initially attempted for the observed results is given below in Eq. (24).

$$\hat{y} = \beta_1 x_1 + \beta_2 x_2^{\alpha} + \beta_3 x_3 + \beta_4 x_1 x_3 + \beta_5 x_1 x_2^{\alpha} + \beta_6 x_3 x_2^{\alpha} + \beta_7 x_1 x_2^{\alpha} x_3 \tag{24}$$

x_1: Applied Current in mA
x_2: Volume Fill Percentage of Neodymium Particles
x_3: Stiffness of Base Elastomer
α: Unknown Power of Volume Fill Percentage to Use

Again, for this model it is important to choose the optimal value of α and to assume that the relationship between blocking force and stiffness is linear in nature. Similar to the procedure used for the individualized model, this model minimized the sum of squared errors as the criterion for picking the optimal value of the unknown parameter α. Optimizing this parameter resulted in the following plot shown in Figure 24 for the minimum value of $\alpha = 2.06$.
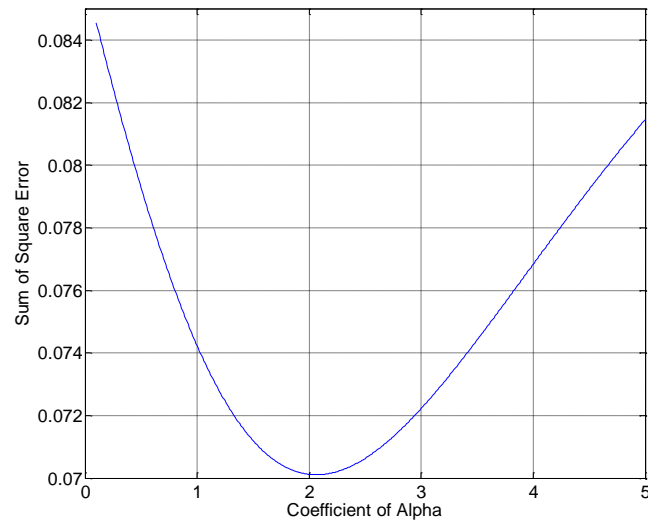
Figure 24: Minimized value of (alpha) for the general model.

Again, it was important to look at how this model fit the actual data because despite the fact that this was the value of alpha that minimized SSE for the general model, the form of the model could have been initially incorrect. The results of the fitted values plotted against the observed values are presented below in Appendix A with an example of HS II shown below in Figure 25. From these results, it is clear that there is some shortcoming in the model that needs to be addressed by changing the form of the model. Instead of assuming that the blocking force varies linearly with the stiffness of the material, the next step of the modeling would be to determine what function determines how the blocking force is related to the stiffness of the base material. However, at this point it was determined that the individualized model would be the best to adopt for these set of materials as there is a nearly flawless fit. Infinitely many more models could be tried by adding more and more terms to the model, but eventually the cost of adding more terms outweigh the benefits of an improved model.

Figure 25: Plot showing the global model that was attempted to be fit for the data of the HS II samples. Clearly this is not a good fit between the experimental and predicted values.

Blocking Force Conclusions

The reason for this great mismatch between the model predictions and the experimental values can be attributed to the data itself. When initially conduc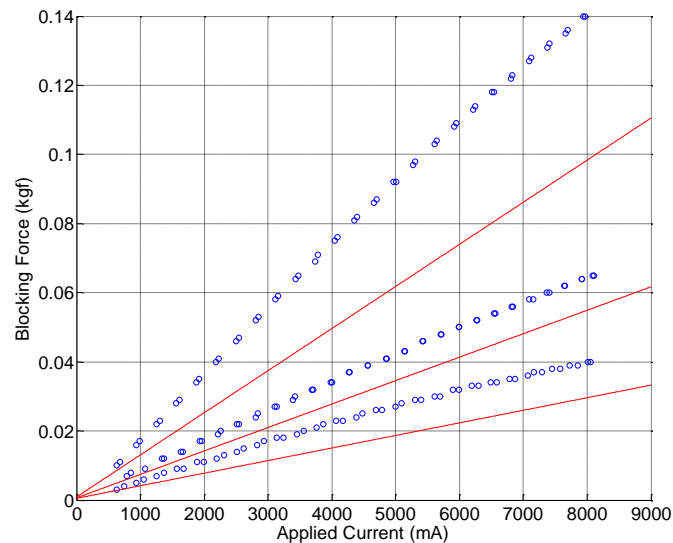ting the experiments and trying to quantify the relationship between materials, it was impossible to say that for a given volume fill, that one material would always produce the highest blocking force, one material would always produce the lowest, and one was always in the middle. Looking at the data, it is clear that from trial to trial, these relationships between materials varied significantly to the point it is indistinguishable. One of the other problems could be that the estimated values being used for the stiffness of these materials is based upon a "rule of thumb" provided by Dow Corning, Additionally, the stiffness also changes as a function of volume fill fraction due to more or less magnetic particles being present within the base elastomeric material, and this effect is not captured by the initial model.

Overall, based on the results of the data and the modeling efforts of predicting the blocking force as a function of volume fill percentage and stiffness, the following conclusions can be drawn:

(1) The blocking force varies linearly as a function of the magnetic field as expected and is directly related to the torque developed within the H-MRE sample due to net magnetic dipole moment.

(2) The blocking force is directly proportional to the volume fill percentage of magnetic filler particles, meaning that for higher volume fill percentages a higher blocking force is experienced. However, this relationship varies for each different base elastomer, indicating that there is also some relationship between the blocking force and some property of the base elastomer (most likely stiffness).

(3) Based on the results of the modeling, a general form of the model that can be utilized in the future and generally defines the behavior of the blocking force is given below in Eq. (25).

$$BlockingForce = B \cdot f(MaterialProperties, VF) \qquad \textbf{(25)}$$

<u>Future Work</u>

Moving forward, there are a number of steps that can be taken to ensure that an adequate blocking force model is developed that can be used to predict the blocking force for any H-MRE material being used in an actuation applications:

(1) Develop a theoretical model of the bending mechanisms as a function of the applied torque and use this model to determine how the blocking force at the tip compares theoretically and experimentally.

(2) Use more advanced modeling and optimization methods to determine an adequate fitting global model for the data that incorporates both the volume fill percentage and material properties of the base elastomer.

(3) Conduct additional experiments using different sized H-MRE samples to determine how the size of the H-MRE sample influences the blocking force in order to add another level of complexity and completeness to the blocking force model.

Sensing and Energy Harvesting Experimentation

Actuation can be considered one of the more "classic" areas of the engineering field as the invention of pneumatic actuators has blossomed into smart actuators being developed as discussed in the preceding sections of this report. On the other hand, sensing and energy harvesting are relatively "new" focus areas in the field of engineering and offer some of the most promising applications moving into the future. One of the key focus areas of much energy research today is the concept of energy and an attempt to find more efficient and effective energy methods [21]. Further, sensors are becoming increasingly important in a world where almost every device you pick up contains some sort of feedback device to allow for proper functionality. These two areas of sensing and energy harvesting are rapidly growing fields that H-MREs have the potential to influence and become a part of in the very near future.

First, it is important to consider some of the work that has already been conducted in the fields of sensing and energy harvesting to gain a better understanding of the scope necessary for these experiments. Similar to actuation, a number of other smart materials have been implemented in the fields of sensing and energy harvesting with great success. In particular, piezoelectrics [22] and a gallium-iron alloy known as Galfenol [23, 24, 25, and 26] are two of the materials at the forefront of work in these fields. Piezoelectrics were some of the first materials to be implemented in sensing and energy harvesting due to the principal of electrostriction [27]. When any conductor is acted upon such that there is a change in shape, an electric field is generated whose power can be harvested. One of the most unique applications involving piezoelectrics is the development of a "tree" of these materials in which the piezoelectric patches are the "leaves" that when moved by the wind could generate power [28, 29].

Similar to the effect of electrostriction, is the effect of magnetostriction in magnetic materials that indicates when a magnetic field is deformed there is a change in the magnetization of the material [30, 31]. If this material is contained within some sort of pick-up coil, then this energy can be harvested or sensed due to the induced voltage within the coil, as illustrated in Figure 26. This basic principle led to the development of Galfenol and a number of studies have been conducted that have looked at the behavior of this material and its capabilities as a sensor or energy harvester. Additionally, some work has been done with soft MRE materials and MRFs in terms of their sensing capabilities with promising results [32, 33].
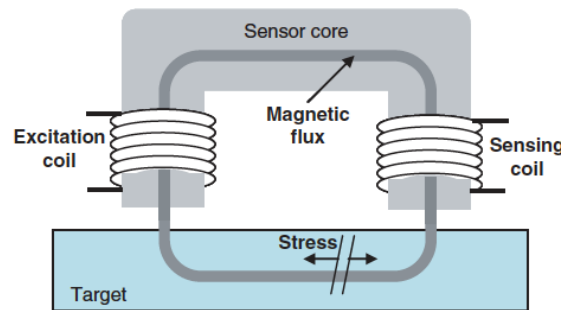

Figure 26: Illustration of a magnetic circuit used in many magnetostrictive sensing and energy harvesting applications [33].

Clearly, there are a number of functioning and effective technologies that exist today in the fields of sensing and energy harvesting, so the question arises: why would H-MRE materials offer any sort of improvement over the status quo? The answer to this question can be summed up with two simply words: flexibility and magnetization. Galfenol is considered the leader in magnetostrictive sensor and actuator technology but has the huge shortcoming that it is a rigid, solid material. Therefore it is limited in the scope of where it can be implemented. However, H-MRE materials are completely flexible and can be made into any shape and size without severely degrading the properties of the material. For example, if one wanted to harness the vibrations on a bridge beam that was circular, it would be difficult to attach a piece of Galfenol effectively. However, an H-MRE sample could be fabricated that would adhere to the given structure and provide an effective and secure solution to the problem.

Additionally, H-MRE materials are permanently magnetic because of the hard magnetic particles embedded within the base elastomer. In other applications where magnetostrictive materials have been used as sensors, a biasing coil has been needed to create a net magnetization within the material such that a voltage can be induced within the pick-up coil. Although this is not a difficult component to include in a system, its elimination could prove to free up valuable space and lead to cost savings. H-MRE materials would not need this bias coil because of their permanent magnetism and could effectively serve as sensors and energy harvesters. Clearly, there are a number of advantages to utilizing H-MRE materials and the following sections of the report will aim to further verify their feasibility in these capacities.

Theoretical Behavior of H-MRE Materials – Sensing and Energy Harvesting
As discussed above, the principle of magnetostriction causes a change in the net magnetization of a magnetic material. This indicates that if one were to strain an H-MRE, then the net magnetization would change and could easily be sensed with a pick-up coil. However, instead of

focusing on straining the material in these experiments, the focus will be on motion of the entire sample within a pick-up coil to better understand how the H-MRE samples would be able to sense vibrations and harness vibrational energy. The basic principle of operation for either of these applications is based on Faraday's law of induction, which states that the EMF generated within a closed circuit (ε) is proportional to the rate of change in the magnetic flux (*dB/dt*). For a tightly wound coil of wire with *N* turns, this equation can be expressed as below in Eq. (27):

$$\varepsilon = N \frac{d\Phi_B}{dt}$$

(27)

Aside from this very basic law of induced voltage within a coil, the scope of this project does not involve much more theoretical derivations of behavior. Instead, the focus is on the development and implementations of experiments that verify the predicted behavior and performance of H-MRE materials as both sensors and energy harvesters.

Sensing Experimentation

For the sensing experiments, the primary goal was to determine if the induced EMF within the pick-up coil could be used to measure some physical phenomenon within the material, such as the motion of a sample (position, velocity, acceleration) or some change of the geometry (strain). As stated, the focus of this study will simply be on determining if the H-MRE sample can be used to accurately detect motion. The primary goal of this experiment will be to compare the output voltage induced within a copper wire pick-up coil to the output voltage of a conventional sensor. If the two signals "match", then this will demonstrate that there is potential for H-MRE materials to be used as sensors in this capacity. The matching of the signals will not be assessed based on if the signals are identical since the magnitude of the output could be (and in fact is) orders of magnitude different. Instead, the primary variable of interest will be the frequency of each signal to determine if both are sensing the same behavior.

For this experimental set-up, picture below in Figure 27 the H-MRE sample was actuated using an MB Dynamics MODAL 50A shaker at frequencies of 10, 20, 40, 60, and 80 Hz. Initially a smaller voice-coil actuator from PASCO was to be used; however the amplitude of vibration was not high enough to produce an identifiable signal. Although it would be ideal to measure the induced voltage within the pick-up coil and the output from the laser sensor at the same time, it was not possible with the available equipment. The lighting within the pick-up coil was too dark for the laser sensor to reflect properly and capture the motion, so each of the tests needed to be ran independently in order to obtain the two signals necessary for comparison. For these tests, the samples that had been fabricated for the blocking force experiments were reused. Six different samples were examined; two from each of the elastomer bases with volume fill percentages of 20% and 30%.
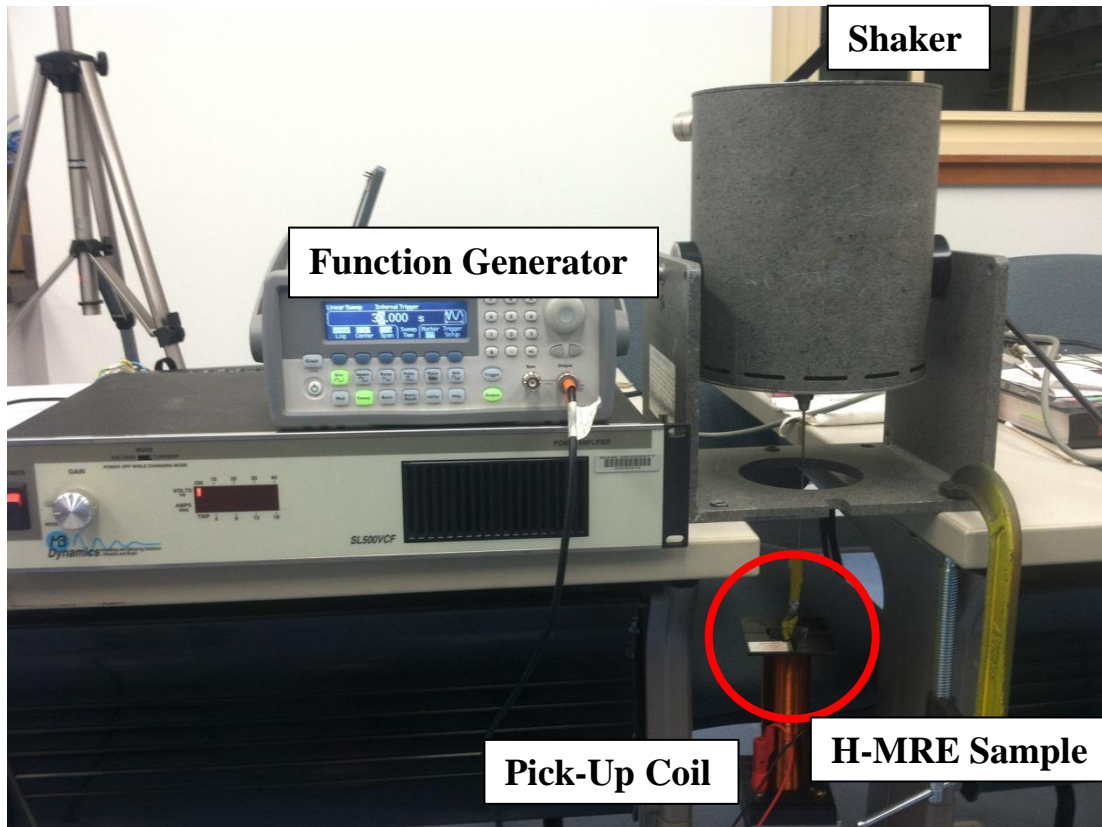
Figure 27: Experimental set-up for the sensing experiments showing how the H-MRE sample is actuated vertically in-and-out of the copper pick-up coil at varying frequencies to measure the induced EMF. Although not shown, the laser displacement measurements were made by simply removing the pick-up coil.

Sensing Experimental Results

After obtaining the results from both the laser displacement sensor and the induced voltage within the pick-up coil, the resulting signals from each were compared. Before making a comparison, one variation needed to be made with the laser displacement data. Since the induced voltage is proportional to the rate of change of the magnetic flux, it would be more appropriate to compare these values to the velocity of the material. By simply multiplying the magnitude of the displacement by the frequency of excitation, the velocity could be derived from this data. An example of a few of the plots showing the comparisons between the induced voltage and the sensor data are provided in Figure 28 and Figure 29 with the remainder included within Appendix B to this report.
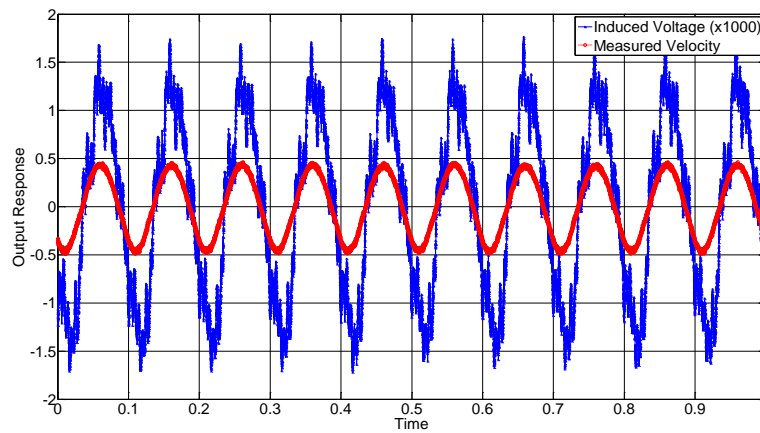
Figure 28: Sensing experimentation results for HS IV 30% excited at 10 Hz showing how the induced EMF within the pick-up coil and laser displacement sensor output have the same frequency signal.
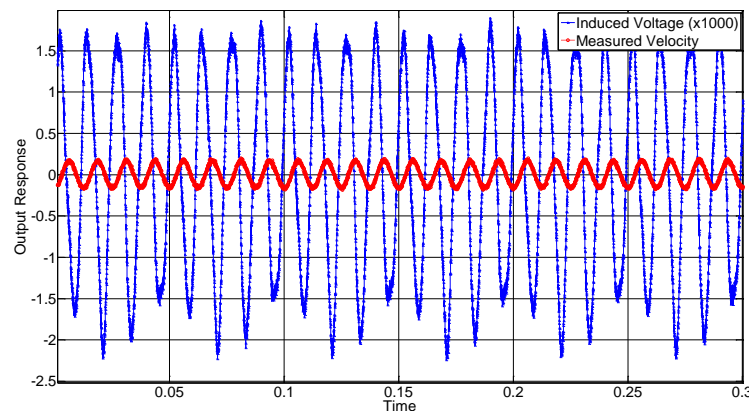

Figure 29: Sensing experimentation results for HS II 30% excited at 80 Hz showing how the induced EMF within the pick-up coil and laser displacement sensor output have the same frequency signal.

Sensing Conclusions

Based on the group of results as a whole given in Appendix B, it is clear that using H-MRE materials would be feasible for sensing applications. Almost all of the signals (when ignoring some noise in the system), have the same frequency regardless of if one is looking at the induced EMF or the output from the laser displacement sensor. There are a few key observations that can be made regarding the results of this experimentation, which are summarized as follows:

(1) The sensing behavior has good and bad characteristics for both low and high frequencies, indicating that it would not be limited to a certain range of frequencies; at least for this small range. It is worth noting that certain materials perform better for certain ranges of frequencies.

(2) The discrepancies between the signals in some cases are most likely attributed to noise in the signal of the induced voltage or non-uniform vibration. Since the H-MRE sample is only constrained with a clamp to be attached to the shaker, it is free

to twist and move in a number of other directions, so certain frequencies do cause non-axial vibrations that could influence the induced voltage within the pick-up coil.

(3) Nearly all of the materials perform poorly around their resonance frequencies of 40-60 Hz. Even though these signals are distinguishable, they are not purely sinusoidal indicating that some non-axial motion is occurring which may obstruct the data of interest.

Energy Harvesting Experimentation

The second set of experiments was focused on the abilities of H-MRE materials to be used as energy harvesters in future applications. For these experiments, the output measurement of interest was again the EMF generated within the pick-up coil. The primary goal for these tests was to determine the optimal operating parameters of the samples for use as energy harvesters. There are a number of different variables that can be changed during fabrication of an H-MRE such as volume fill percentage of magnetic particles, dimensions of the sample, orientation of the magnetic particles, as well as the base elastomer material. Most importantly, it is important to determine how much of an effect the volume fill percentage of a material has on the energy harvesting potential of an H-MRE sample. In this experiment, the energy harvesting potential will be measured based on comparisons between multiple samples and by calculating an efficiency factor as described below.

In this experimental set-up, pictured below in Figure 30, the H-MRE was placed in a fixture that was fabricated so that the sample would vibrate so as to simulate a cantilevered beam. By attaching this fixture to the PASCO voice coil actuator, this vibration could be effectively simulated. The samples used for these experiments were the same ones used for the sensing and blocking force experiments. The samples were clamped into the fixture, and the voice coil actuator drove the vibration of the sample at six different frequencies (7.5 Hz, 10 Hz, 12.5 Hz, 15 Hz, 20 Hz, and 25 Hz). These frequencies were chosen by simply observing the behavior of the H-MRE sample to find places where the vibrational motion was appropriate for this experiment. The sample itself was again placed in the pick-up coil in order to measure the induced voltage caused by this vibration. Additionally, a laser displacement sensor was again used in order to ultimately calculate the velocity of the sample during vibration. Measurements were taken for seven different samples and compared against one another qualitatively by simply looking at the results of the induced EMF within the pick-up coil. Quantitatively, an efficiency factor was developed which was a ratio of the electrical energy output to the mechanical energy input to determine which samples had the most optimal performance for this particular set-up.
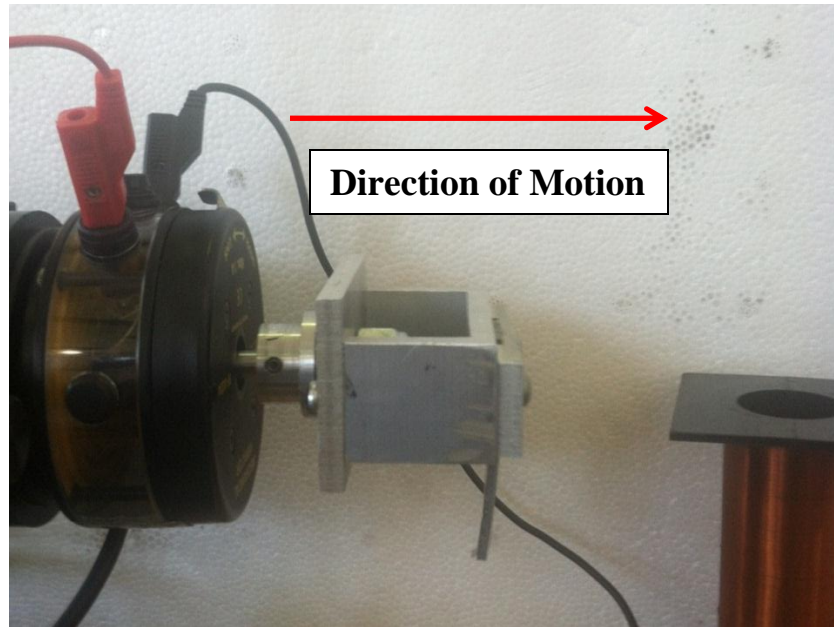
Figure 30: Photo of the experimental set-up used for the energy harvesting experiments showing the fixture that is attached to the PASCO voice-coil actuator to cause a cantilevered beam vibration of the H-MRE sample.

Energy Harvesting Results

The initial energy harvesting results simply compare the induced voltage output signals among samples made of the same base elastomer with varying volume fill percentages. In general, each of the samples when actuated with a sine sweep signal, have the same generic pattern and a distinct point where the induced voltage in the coil starts to climb significantly, as depicted in Figure 31. It is hypothesized that this corresponds to the resonant frequency of the sample since that is when the vibration would be the largest, therefore changing the magnetic flux at the fastest rate and in turn the induced voltage. In order to verify these results, it was important to determine this one frequency for each of the different samples analyzed in this study. In order to determine the frequency components of a signal, a mathematical technique known as the Fast Fourier Transform (FFT) in implemented. Without going into too many of the mechanics of this analysis, an FFT looks at a time signal and determines which frequency components are prevalent and additionally which have the highest magnitude. For a sine sweep such as this, using an FFT will help to quantify the resonant frequency that corresponds to the highest induced voltage, as shown in Figure 32. The results of the sine sweep and FFT for the samples are included in Appendix C, with the results for ideal operating frequencies of each sample summarized below in Table 7:

Table 7: Summary of the ideal operating frequencies of the samples as cantilevered beam energy harvesters based on the results of the energy harvester experiments.

Sample	Ideal Operating Frequency (Hz)	Sample	Ideal Operating Frequency (Hz)
HS II 10%	11.5	HS III 20%	12.63
HS II 20%	12.14	HS III 30%	12.37
HS II 30%	12.17	HS IV 20%	12.17
		HS IV 30%	12.96

Based on the results of the table above, it is clear that there is a difference in the ideal operating frequency for each of the samples tested in these experiments. Since this frequency is related, and in fact identical to, the resonant frequency of each sample this indicates that energy harvesters can be designed for any particular application. The reason that there are differences among these seemingly identical samples (geometry-wise) is that the volume fill percentage of magnetic particles, as well as the base elastomer contributes to a variation in resonant frequency. Overall, these experiments show that H-MRE materials do have potential as energy harvesters and can be designed accordingly once a need in a certain application is presented.
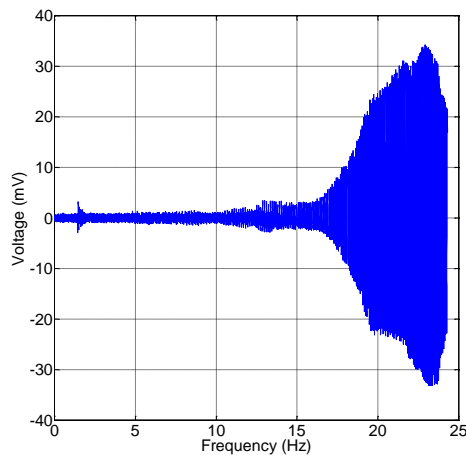
Figure 31: Plot showing the general shape of the sweep response for energy harvesting experimentation.
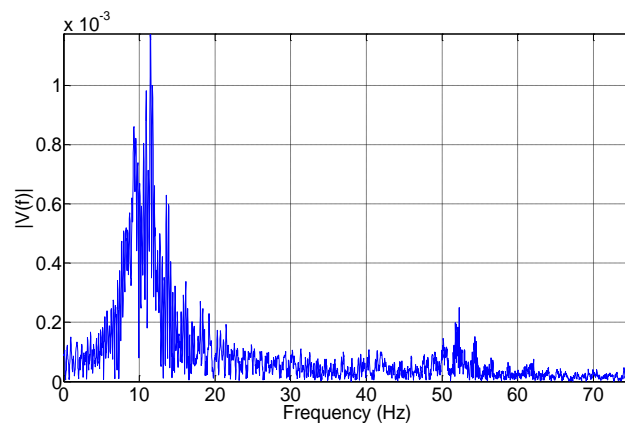
Figure 32: Example FFT plot showing that there is a clear ideal operating frequency for use of H-MRE materials as energy harvesters.

Additionally, for all samples it is clearly seen that an increasing volume percentage of magnetic filler particles leads to an increase in the maximum output voltage for that particular energy harvester, as pictured in Figure 33. This is important for designing energy harvesters in the future because this trend would imply that more magnetic particles should be added for higher power outputs. However, it is clear that this will also vary the dynamic properties of the material (resonant frequency), and will need to be considered in design applications. Also, in the future it will be beneficial to test samples with even higher volume fill percentages to determine if there is

any sort of saturation point where adding more magnetic filler particles actually becomes detrimental to performance.
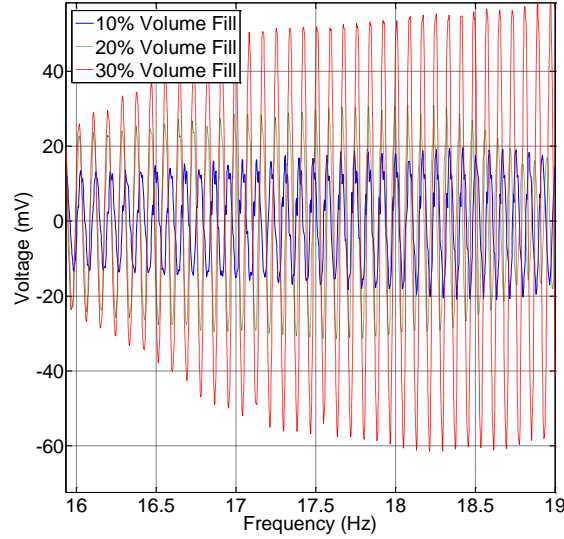
Figure 33: Plot showing the difference of induced voltage within the pick-up coil for different volume-fill percentages of HS II H-MRE samples.

Aside from simply looking at the graphical output of the energy harvesting response of these samples, it was also important to try and quantify these results. In order to do so, an efficiency factor was derived that measured the ratio of the power generated in watts versus the mechanical work done by the sample per kg mass as measured by the velocity (J/kg). To calculate the mechanical energy input into the system, the relationship between energy and velocity as given by Eq. (28) below was utilized, where E_{mech} is the mechanical energy/work input, m is the mass of the sample, and v is the velocity. By ignoring the mass of the sample, the energy per unit mass can be easily derived and is utilized in the efficiency ratio.

$$E_{mech} = \frac{1}{2}mv^2 \qquad \textbf{(28)}$$

Instead of using a laser vibrometer or similar device to measure the velocity of the device directly, the displacement of the sample was measured using a laser displacement sensor. Using the form of a sinusoidal displacement, $x(t)$, given below in Eq. (29) and the relationship between the displacement and velocity given in Eq. (30), a value for the average velocity of the sample at a given frequency, ω, was derived.

$$x(t) = A\sin(\omega t) \qquad \textbf{(29)}$$

$$v(t) = \frac{d}{dt}[x(t)] = \frac{d}{dt}[A\sin(\omega t)] = A\omega\cos(\omega t) \qquad \textbf{(30)}$$
$$\|v(t)\| = A\omega$$

To calculate the maximum power, the maximum voltage must first be calculated using the time domain plots shown in Appendix C. Instead of looking at a sweep over a range of frequencies, a number of individual frequencies were examined in order to determine a general trend and a range of reasonable values. At each of the frequencies within the sweep, the maximum voltage was obtained by a detailed inspection of the plots and data. However, in order to calculate power this value alone could not be used since this is essentially an alternating voltage signal due to the sinusoidal motion of the sample. For an AC signal, the power of the signal is given as a function of the RMS voltage, V_{rms}, and resistance of the load R in Eq. (31) below. Additionally, the peak-to-peak voltage of a sinusoidal signal can be converted to an RMS voltage using Eq. (32).

$$P = \frac{V_{rms}^{2}}{R} \tag{31}$$

$$V_{rms} = \frac{V_{peak}}{\sqrt{2}} \tag{32}$$

Using these relationships below, an efficiency factor as measured by the ratio of the electrical energy output to the mechanical energy input was derived for each sample at a number of different frequencies. These ratios are given per unit resistance and unit mass as intensive properties to try and better characterize H-MRE devices in general. In order to quantify the potential of these devices, the output signal was assumed to be amplified by 100 times, since the magnitude of the unaltered signal is too small to provide sufficient power for most devices. Using an amplifier is a common technique to generate higher voltages and powers, however, at a certain point amplifiers do not work without some additional power input. For these initial calculations, this additional power input will be ignored since it is rather negligible for such small amplifications. The results of these calculations are provided below in Table 8. Additionally, information about the velocity and voltage that were calculated from the experimental data is included in Appendix C for the reader's reference.

Table 8: Values of the efficiency factor developed for the H-MRE samples used in energy harvesting experiments.

Sample	Volume Fill Percentage	Excitation Frequency Efficiency ($\frac{\Omega}{kg}$)					
		7.5 Hz	10 Hz	12.5 Hz	15 Hz	20 Hz	25 Hz
HS II	10%	0.28%	0.51%	0.16%	0.36%	11.85%	2.01%
HS II	20%	0.35%	0.28%	0.25%	0.79%	29.54%	8.49%
HS II	30%	1.35%	3.42%	0.79%	2.57%	96.02%	35.60%
HS III	20%	0.18%	0.18%	0.19%	0.24%	3.04%	22.91%
HS III	30%	1.52%	1.19%	1.51%	0.64%	1.68%	50.95%
HS IV	20%	0.25%	0.31%	0.23%	0.39%	0.94%	1.50%
HS IV	30%	0.75%	0.87%	0.74%	0.67%	0.38%	20.09%

Based on the results presented above, it is clear that there is a large potential for energy harvesters to be created using H-MRE materials in the future. It is important to remember that the

efficiencies presented here are on a per mass and per load basis, meaning that depending on the application, the efficiencies could start decreasing rather rapidly. A combination of low mass and low loads would lead to the most ideal energy harvesters there are, but balancing the two variables will be important in designing the most efficient energy harvesters possible. Additionally, although the power generated is only a few mili-watts (mW), this power is still useful for micro devices that don't have a high power draw. Clearly, if the proper application is selected, any H-MRE material could be a suitable power source by simply harvesting vibrational energy. Overall, it is clear that H-MRE materials show potential for use in this growing field moving into the future.

Energy Harvesting Conclusions
Based on the results of the graphical interpretations as well as the numerical calculations, the following conclusions can be drawn for the energy harvesting capabilities of H-MRE materials:

(1) In energy harvesting applications, it is most beneficial to have H-MRE samples with a higher volume fill percentage of magnetic particles as the results clearly indicate higher induced voltages for those samples with more magnetic particles.

(2) In designed energy harvesters, it is important to utilize a device with the ideal resonant frequency for the particular application since this will lead to the largest induced voltage within a pick-up coil. This is evidence by the large increase in induced voltages in these experiments in the plots of Appendix C.

(3) Overall, H-MREs seem to have relatively low efficiencies in terms of converting mechanical energy into usable electrical energy (when accounting for reasonable masses and electrical loads). However, there may be some improvements to be made in the system design that could address these issues. By using op-amps or other amplifying tools, these signals could become more useful in the future for power devices and harnessing otherwise wasted energies.

Conclusion of the Thesis/Potential Future Work
The objective of these studies was to try and better understand the behavior of hard magneto-rheological elastomers in a number of different potential applications. Since these are a relatively new smart material, insufficient work has been done by others in terms of the basic characterizations necessary before implementing these materials as solutions to real-world engineering problems. Through this study, the groundwork has been laid for the use of H-MRE materials as actuators, sensors, and energy harvesters in the future. This study has shown that this material is capable of being implemented in all of these applications. Although all of these experiments have been critical to understanding this material and advancing the knowledge of the scientific community, it is important that work continues in the future on H-MRE materials with some potential ideas for continued research summarized as follows (other future work ideas included within body of text):

Actuation Applications
- Conduct additional experiments using different samples to determine the adequacy and accuracy of the current model, refining the model as needed. These experiments will also assist in properly optimizing the model parameters by providing a larger data set.

- Continue to develop an appropriate bending model using both conventional and novel techniques for verification. The current model was developed using conventional Euler beam theory, however a number of other theories have been developed and should be considered. Also, including other variables such as the viscous damping of the material could prove crucial in more accurately predicting the bending behavior.

- Continue to develop models for the blocking force of the materials, focusing more specifically on how the geometric properties influence the blocking force of the sample. Instead of trying to focus on a fully global model to define the blocking force for every H-MRE, it would be beneficial to consider each combination of base elastomer and filler particles as an "alloy" and develop individual models for the behavior of each material.

- Develop an appropriate computational simulation of the material using some sort of commercial multi-physics software (i.e. COMSOL MultiPhysics) to better understand the theoretical behavior.

Sensing Applications
- The capabilities of H-MRE materials to sense a well-defined sinusoidal signal have been clearly established, however, it would be important to also determine the ability of these samples to detect more arbitrary signals as would be encountered in real life.

- Develop experiments to assess the capabilities of H-MRE as strain gauges by measuring the induced voltages as an H-MRE material is strained. These experiments could be developed to measure both axial and rotational strain.

- Determine appropriate mathematical models that help to determine the proper relationships/scaling factors between the actual motion of an H-MRE sample and the induced voltage. This would essentially involve developing calibration curves for each particular H-MRE sensor, similar to those provided with any commercial sensor.

- Development of a smart actuator whose position can be controlled using the actuation properties of H-MRE materials. Additionally, this actuator would utilize the sensing properties of the material to determine its position and incorporate this capability into a feedback control system.

Energy Harvesting Applications
- Subject the energy harvesting samples to a random noise excitation to determine if energy can still be harvested appropriately even without ordered sinusoidal motion. This would be a more accurate representation of how vibrational energy would need to be harvested on any structure.

- Develop an energy storage circuit in which the harvested energy from a pick-up coil could be stored within a capacitor and then used to power some sort of small device. This would help to give a more clear understanding of the scope of energy harvesters and how much power they could practically provide.

- Conduct additional experiments to determine the ideal orientation of H-MRE particles as energy harvesters. Additionally, introduce biasing magnetic fields to examine the effects this has on the energy harvesting capabilities of the materials.

Clearly, there is a great deal of research to be done in the area of H-MRE and smart materials in general. These types of materials have a stronghold on a number of crucial engineering applications moving forward in the coming years. This project itself has helped to show the capability of these materials in certain applications and begin some of the initial modeling and characterization of the material needed for other engineers to utilize in future designs. All of the experiments and activities performed in this project have been a success and clearly have helped to provide sufficient evidence of the hypothesized behavior of H-MRE materials. Therefore, based on the results of this extensive study on the behavior of hard magneto-rheological elastomers in the capacity of actuators, sensors, and energy harvester, it is evident that these materials should be at the fore-front of consideration for utilization in these applications in the coming years.

References

[1] Rabinow, J., 1948, "The Magnetic Fluid Clutch," Transactions of the American Institute of Electrical Engineers, 67(2), pp. 1308-1315.

[2] Jolly, M. R., Bender, J. W., and Carlson, J. D., 1998, "Properties and Applications of Commercial Magnetorheological Fluids," International Symposium on Smart Structures and Materials, The International Society for Optics and Photonics, San Diego, CA.

[3] "2011 Acura ZDX - Integrated Dynamics System." *Acura.com*. Web. 04 Mar. 2011. <http://www.acura.com/Features.aspx?model=ZDX&modelYear=2011&context=Performanc e#integrated_dynamics_system>.

[4] "Types of Magnetic Materials", Magnetic Materials Unit, Japan National Institute for Materials Science, Updated: June 3, 2011 http://www.nims.go.jp/apfim/soft&hard.html

[5] Deng, H.-x., and Gong, X.-l., 2008, "Application of Magnetorheological Elastomer to Vibration Absorber," Communication in Nonlinear Science and Numerical Simulation(13), pp. 1938-1947.

[6] Jung, H.-J., Park, J.-S., and Koo, J.-H., "Dynamic Analysis of a Smart Base-Isolation System Based on MR Elastomers," Proc. Conference on Smart Materials, Adaptive Structures, and Intelligent Systems, American Society of Mechanical Engineers.

[7] Davis, L. C., 1999, "Model of Magnetorheological Elastomers," Journal of Applied Physics, 85(6), pp. 3348-3351.

[8] Faidley, L., Tringides, C., and Hong, W., "Sensor Behavior of Magneto-Rheological Elastomers," Proc. Conference on Smart Materials, Adaptive Structures, and Intelligent Systems, American Society of Mechanical Engineers.

[9] Moskalik, A. J., and Brei, D., 1999, "Force-Deflection Behavior of Piezoelectric C-Block Actuator Arrays," Smart Materials and Structures, 8(5), pp. 531-543.

[10] Wang, Q.-M., and Cross, L. E., 1999, "Tip Deflection and Blocking Force of Soft PZT-Based Cantilever RAINBOW Actuators," Journal of the American Ceramic Society, 82(1), pp. 103-110.

[11] Bar-Cohen, Y., Xue, T., Shahinpoor, M., Simpson, J. O., and Smith, J., "Low-Mass Muscle Actuators Using Electroactive Polymers (EAP)," Proc. International Symposium on Smart Structures and Materials, International Society for Optics and Photonics.

[12] Isikman, S. O., Ergeneman, O., Yalcinkaya, A. D., and Urey, H., 2007, "Modeling and Characterization of Soft Magnetic Film Actuated 2-D Scanners," IEEE Journal of Selected Topics in Quantum Electronics, 12(2), pp. 283-289.

[13] Lee, S., Park, H. C., and Kim, K. J., 2005, "Equivalent Modeling for Ionic Polymer-Metal Composite Actuators Based on Beam Theories," Smart Materials and Structures, 14(6), pp. 1363-1368.

[14] Alici, G., Mui, B., and Cook, C., 2006, "Bending Modeling and its Experimental Verification for Conducting Polymer Actuators Dedicated to Manipulation Applications," Sensors and Actuators(126), pp. 396-404.

[15 Li, G., Zhao, Y., Pang, S.-S., and Li, Y., 1999, "Effective Young's Modulus Estimation of Concrete," Cement and Concrete Research(29), pp. 1455-1462.

[16] Hibbeler, R.C., 2008, *Mechanics of Materials*, Pearson Prentice Hall, New Jersey

[17] "Dow Corning Technical Library." *Dowcorning.com*. Dow Corning Corporation. Web. 7 Sept. 2011.
<http://www.dowcorning.com/applications/search/content/default.aspx?WT.svl=1>.

[18] "Matweb: Material Property Data", www.matweb.com, Accessed: April 23, 2012

[19] Neter, J., Kutner, M., Wasserman, W., and Nachtsheim, C., 1996, Applied Linear Statistical Models, McGraw-Hill, New York, NY.

[20] Conway, N. J., and Kim, S.-G., "Large-Strain, Piezoelectric, In-Plane Micro-Actuator," Proc. International Conference on Micro Electro Mechanical Systems (MEMS), IEEE, pp. 454-457.

[21] Yiming Liu, Geng Tian, Yong Wang, Junhong Lin, Qiming Zhang, and H. F. Hofmann. "Active Piezoelectric Energy Harvesting: General Principle and Experimental Demonstration." *Journal of Intelligent Material Systems and Structures* 20.5 (2008): 575-85.

[22] Atulasimha, J., and A. B. Flatau. "Experimental Actuation and Sensing Behavior of Single-crystal Iron-Gallium Alloys." *Journal of Intelligent Material Systems and Structures* 19.12 (2008): 1371-381.

[23] Yoo, J.-H., and Flatau, A. B., "A Bending Mode Galfenol Electric Power Harvester," Proc. Conference on Smart Materials, Adaptive Structures, and Intelligent Systems, American Society of Mechanical Engineers.

[24] Downey, P. R., and Flatau, A. B., 2005, "Magnetoelastic Bending of Galfenol for Sensor Applications," Journal of Applied Physics, 97(10), pp. 10R505-(501-503).

[25] Flatau, A. B., and Staley, M. E., "Characterization of Energy Harvesting Potential of Terfenol-D and Galfenol," Proc. International Conference on Smart Structures and Materials, The International Society for Optics and Photonics.

[26] Tian, T. F., Li, W. H., and Deng, Y. M., 2011, "Sensing Capabilities of Graphite Based MR Elastomers," Smart Materials and Structures, 20(2).

[27] Jung, H.-J., Kim, I.-H., and Jang, S.-J., 2011, "An Energy Harvesting System Using the Wind-Induced Vibration of a Stay Cable for Powering a Wireless Sensor Node," Smart Materials and Structures, 20(7).

[28] Stephen, N. G., 2006, "On Energy Harvesting from Ambient Vibration," Journal of Sound and Vibration(293), pp. 409-425.

[29] Wang, D. H., and Wang, T., 2009, "Principle, Design and Modeling of an Integrated Relative Displacement Self-Sensing Magnetorheological Damper Based on Electromagnetic Induction," Smart Materials and Structures, 18(9).

[30] Sodano, H. A., Inman, D. J., and Park, G., 2004, "Estimation of Electric Charge Output for Piezoelectric Energy Harvesting," Strain Journal, 40(2), pp. 49-58.

[31] Sodano, H. A., Inman, D. J., and Park, G., 2004, "A Review of Power Harvesting from Vibration using Piezoelectric Materials," The Shock and Vibration Digest, 36(3), pp. 197-205.

[32] Grimes, C. A., Mungle, C. S., Zeng, K., Jain, M. K., Dreschel, W. R., Paulose, M., and Ong, K. G., 2002, "Wireless Magnetoelastic Resonance Sensors: A Critical Review," Sensors, 2, pp. 294-313.

[33] Calkins, F. T., Flatau, A. B., and Dapino, M. J., 2007, "Overview of Magnetostrictive Sensor Technology," Journal of Intelligent Material Systems and Structures, 18, pp. 1057-1066.

Appendix A – Blocking Force Experimental Data and Modeling Results
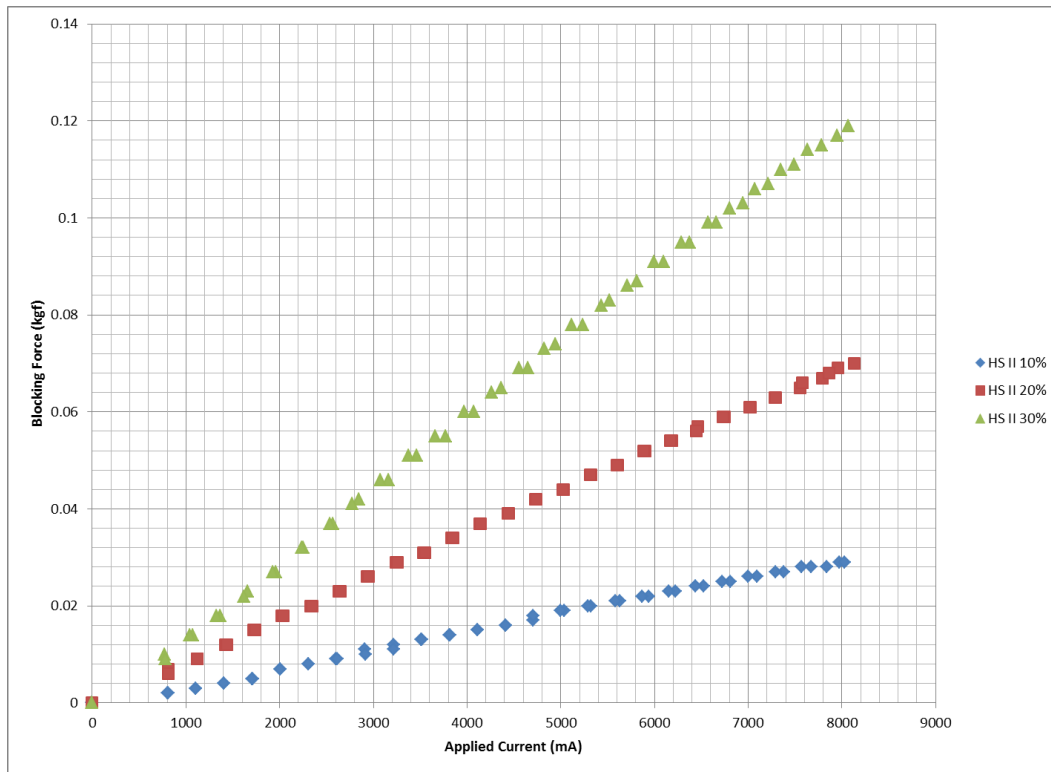
Figure 34: Blocking force experimental results for HS II.
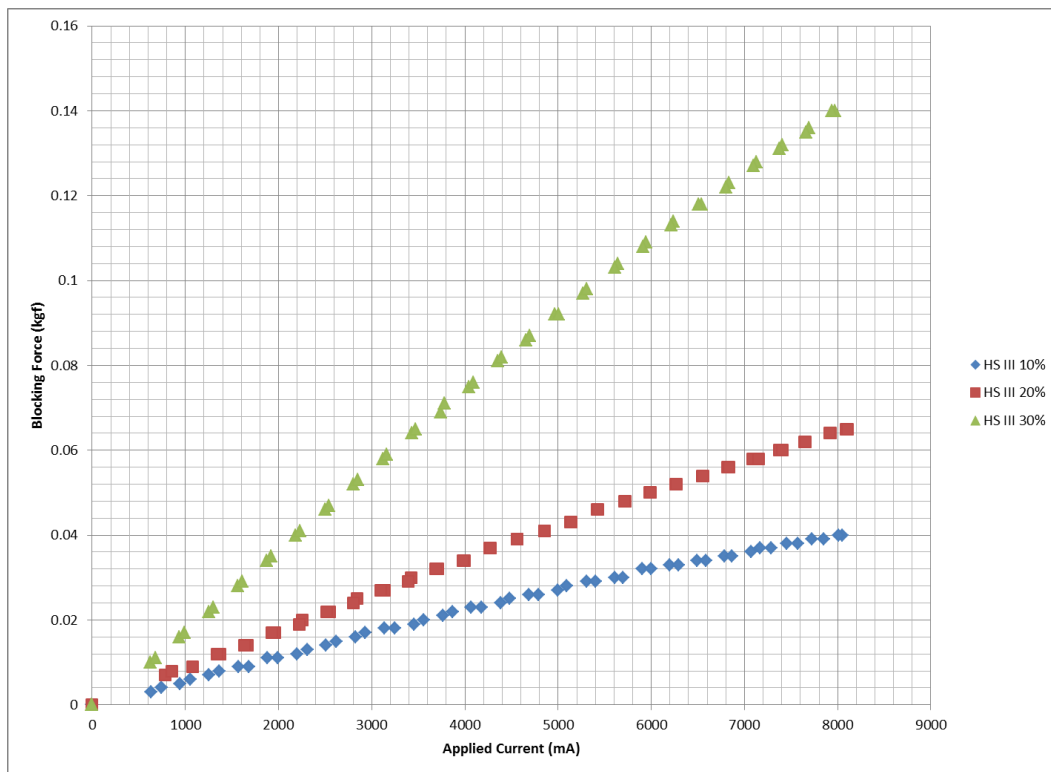
Figure 35: Blocking force experimental results for HS III.
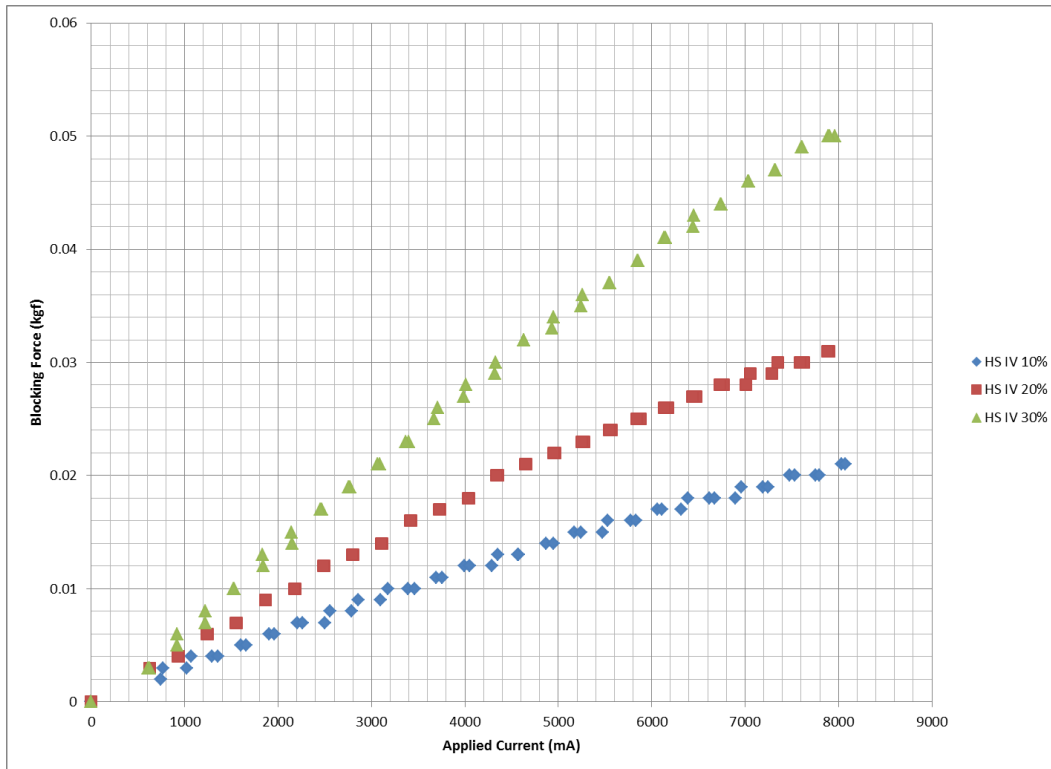
Figure 36: Blocking force experimental results for HS IV.
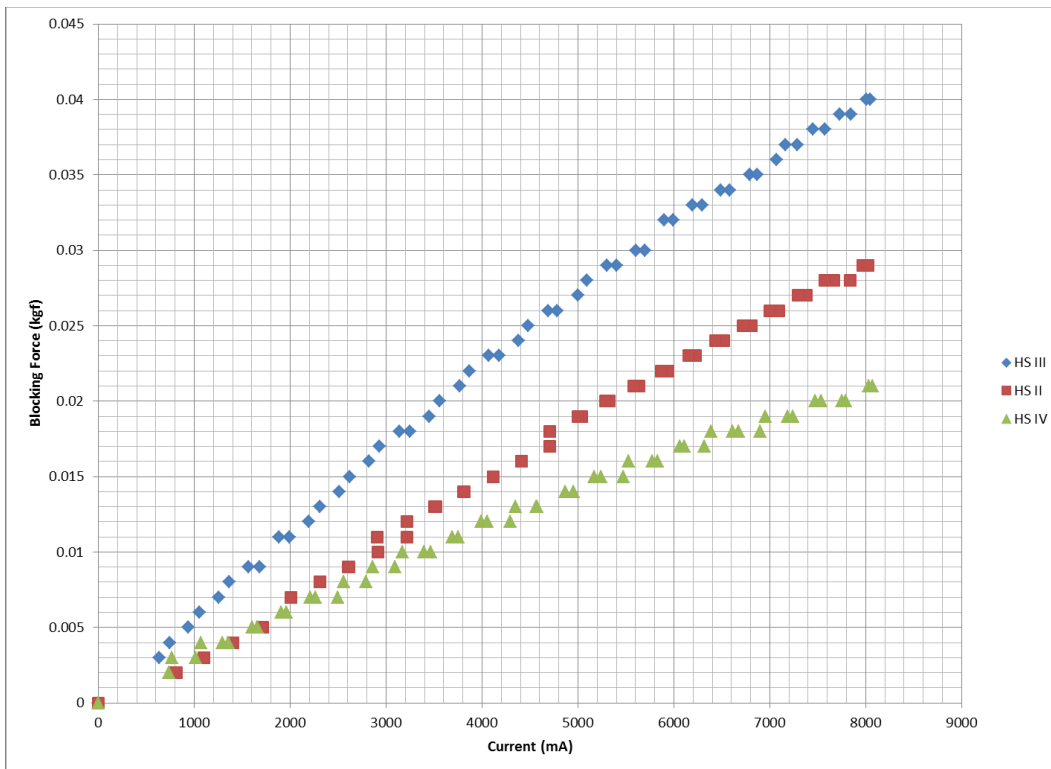
Figure 37: Blocking force experimental results for 10% volume fill percentage neodymium.
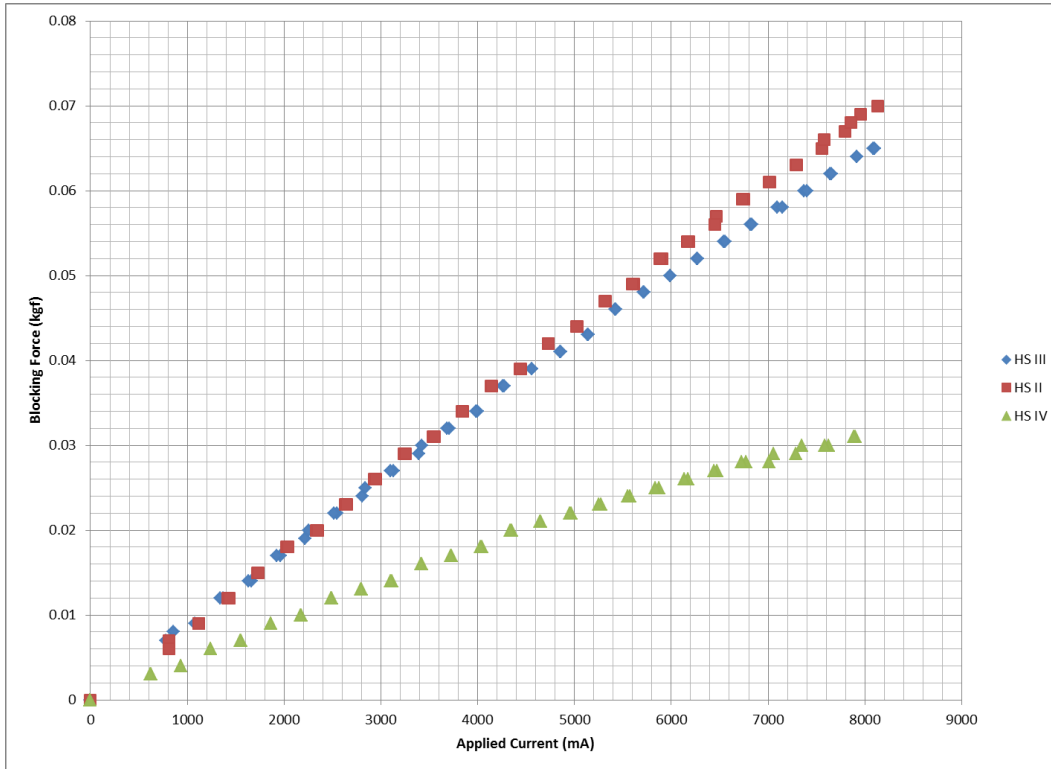
Figure 38: Blocking force experimental results for 20% volume fill percentage neodymium.
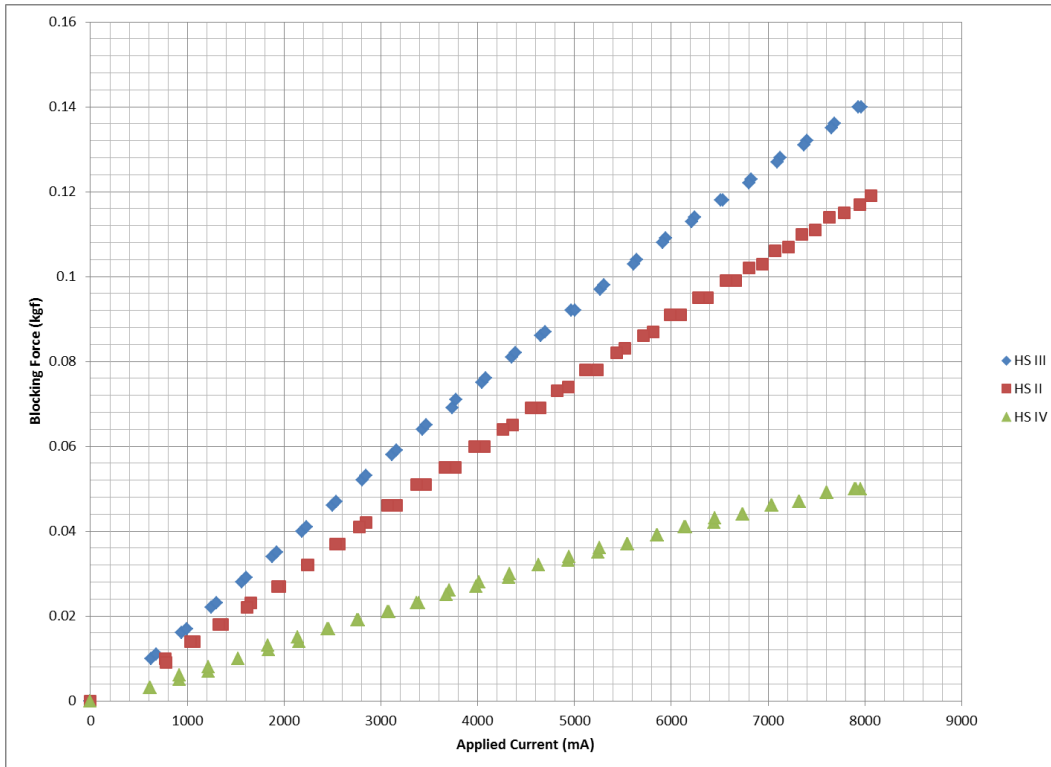
Figure 39: Blocking force experimental results for 30% volume fill percentage neodymium.
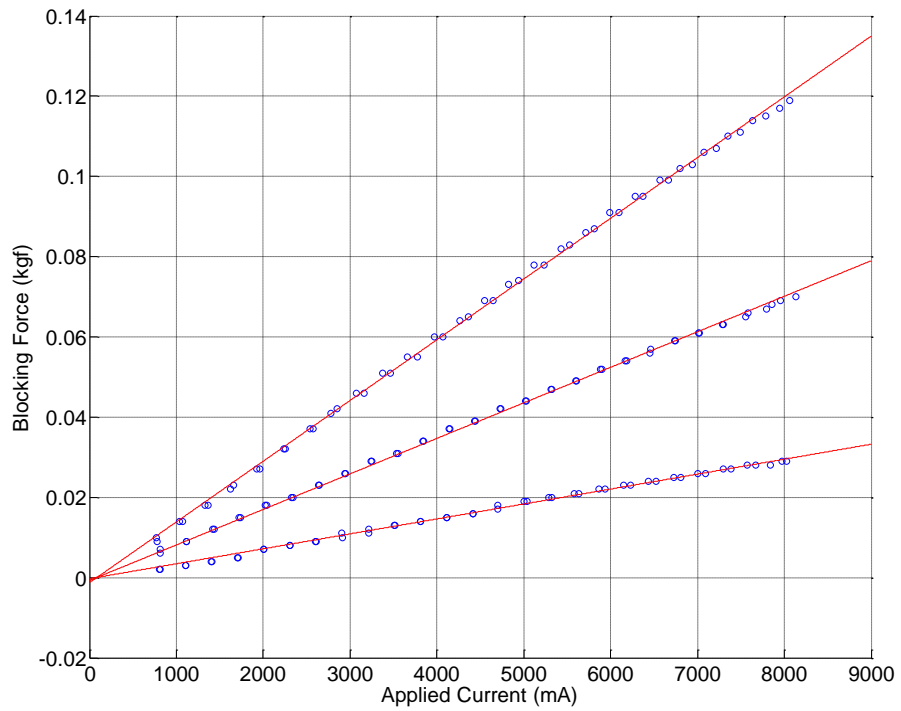
Figure 40: Individual blocking force model fitting for HS II.
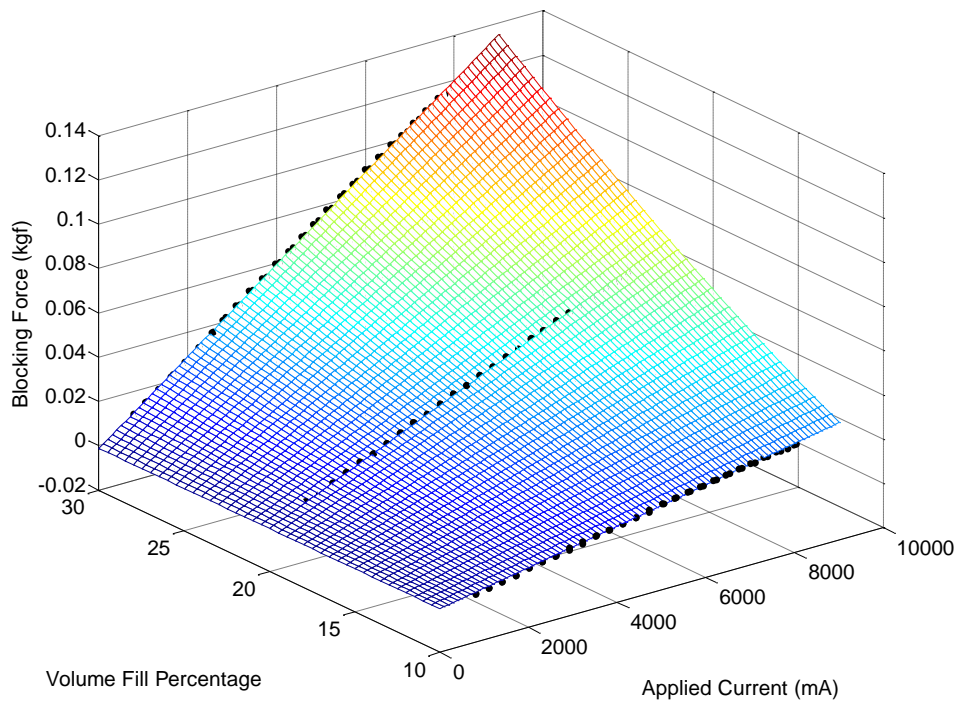
Figure 41: Individual blocking force model fitting for HS II, 3D plot.
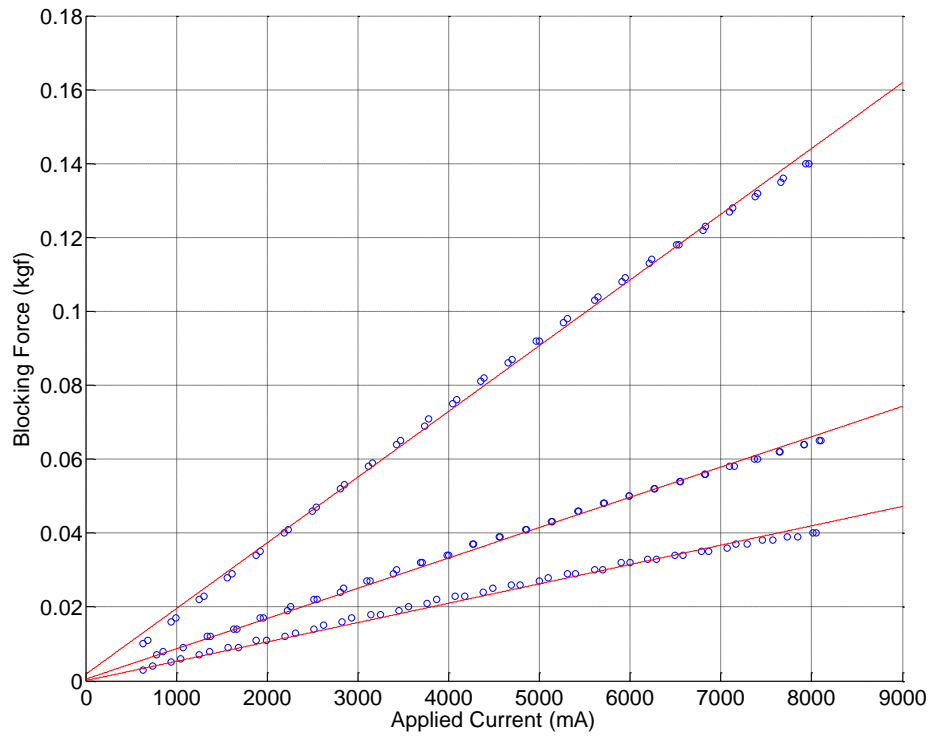
Figure 42: Individual blocking force model fitting for HS III.
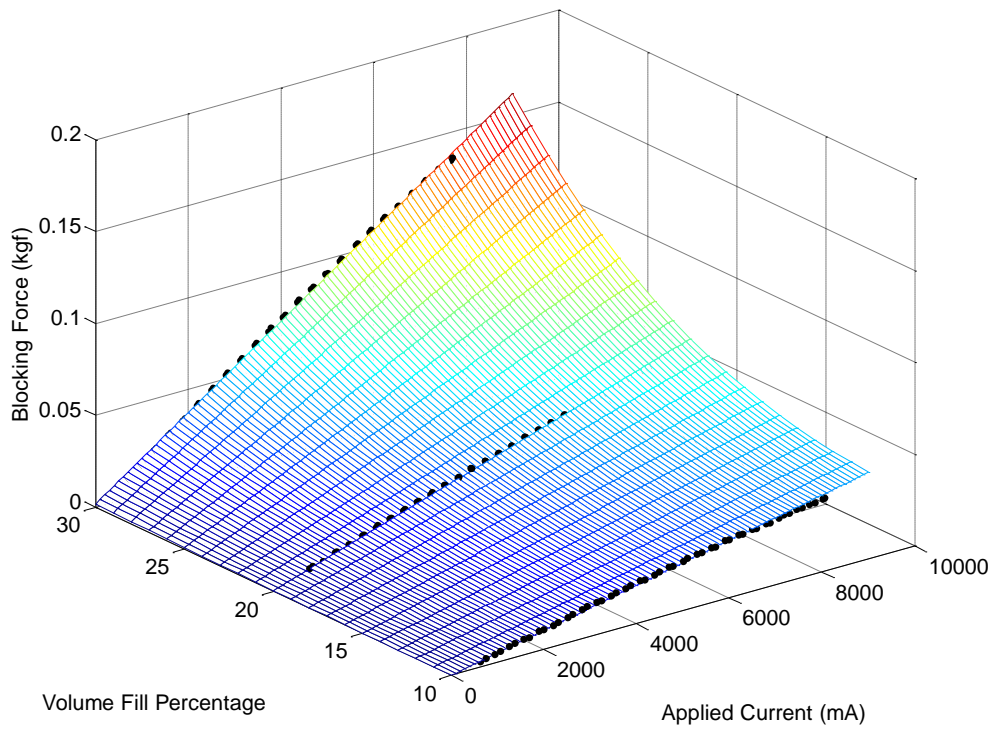
Figure 43: Individual blocking force model fitting for HS III, 3D plot.
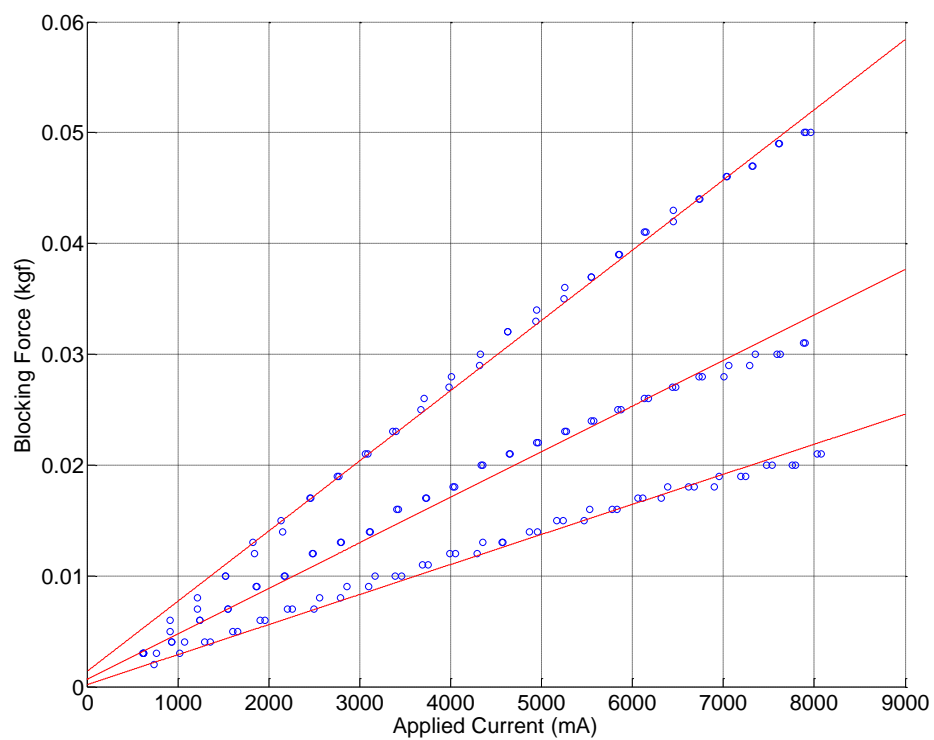
Figure 44: Individual blocking force model fitting for HS IV.
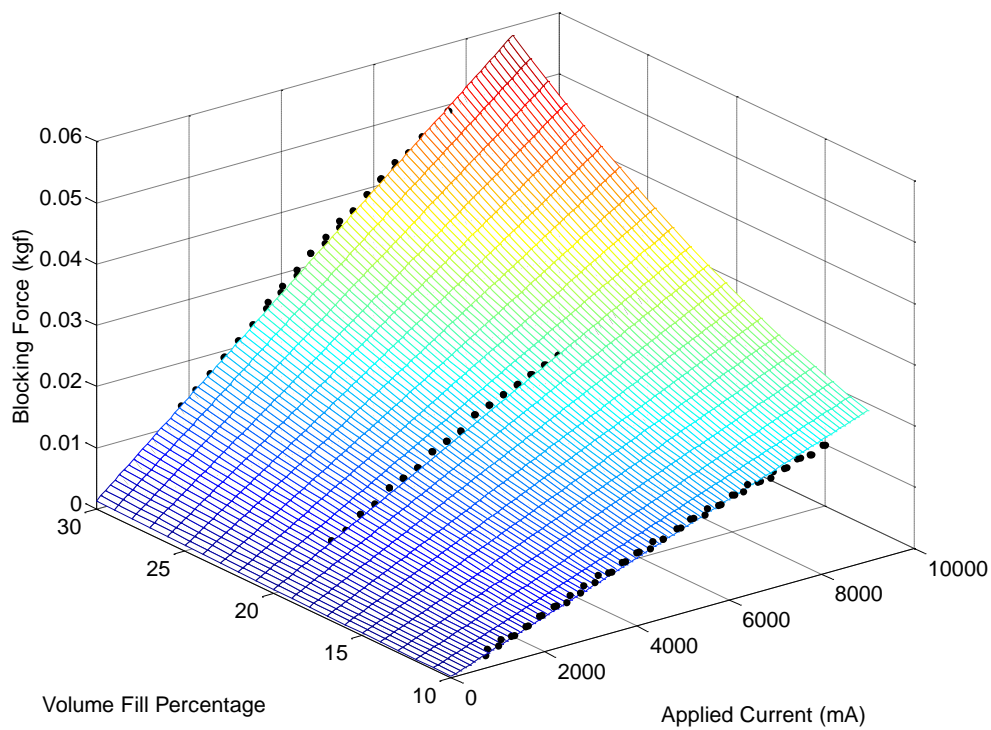
Figure 45: Individual blocking force model fitting for HS IV, 3D plot.
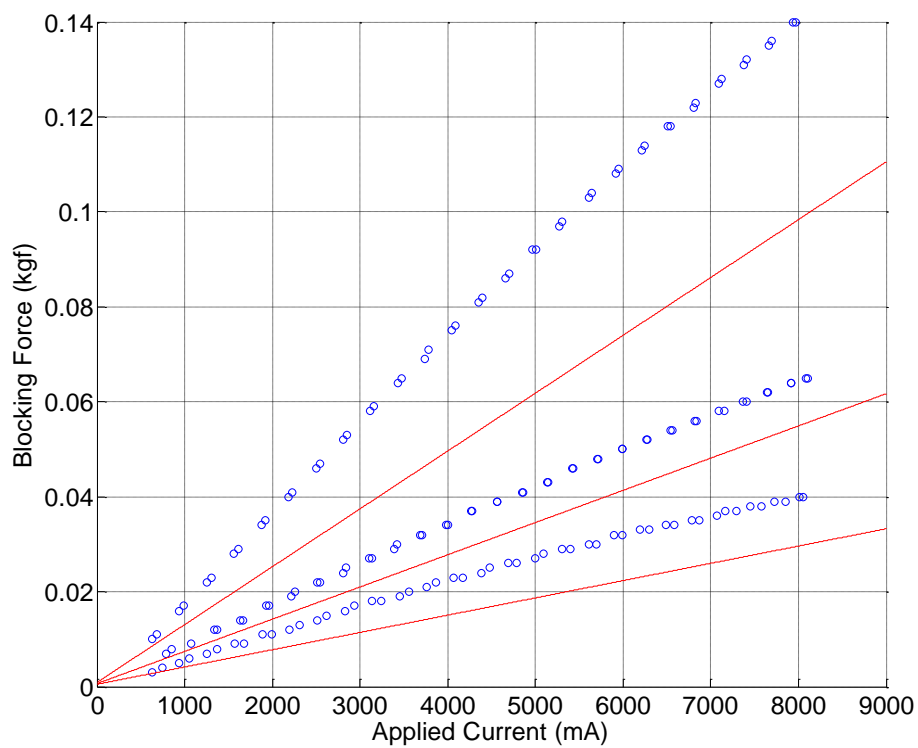
Figure 46: Global model fitting results for HS II samples.
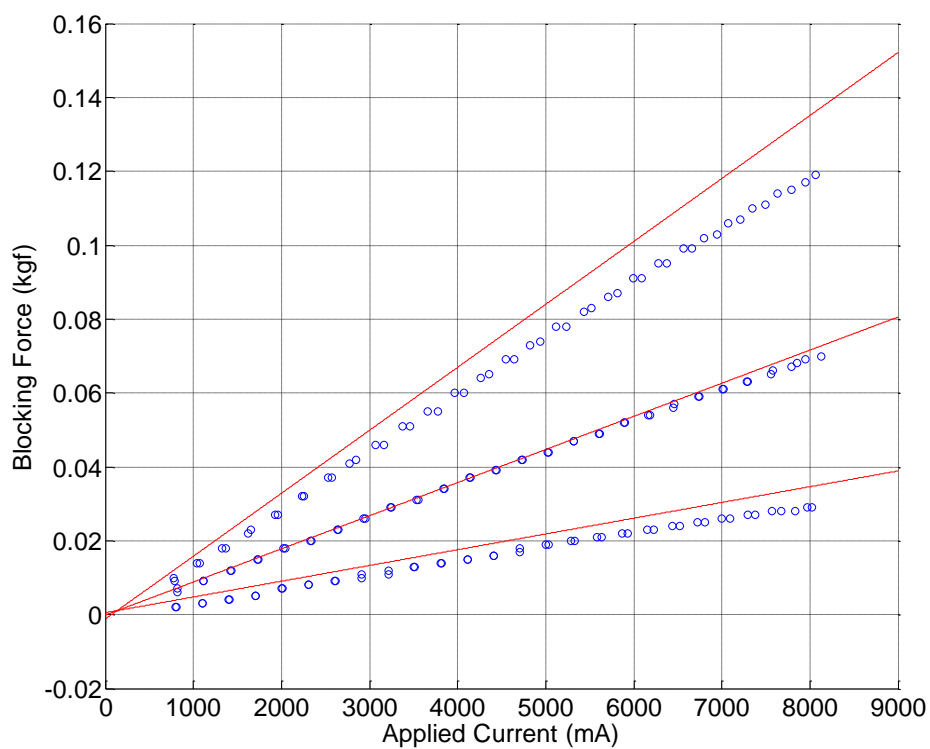
Figure 47: Global model fitting results for HS III samples.
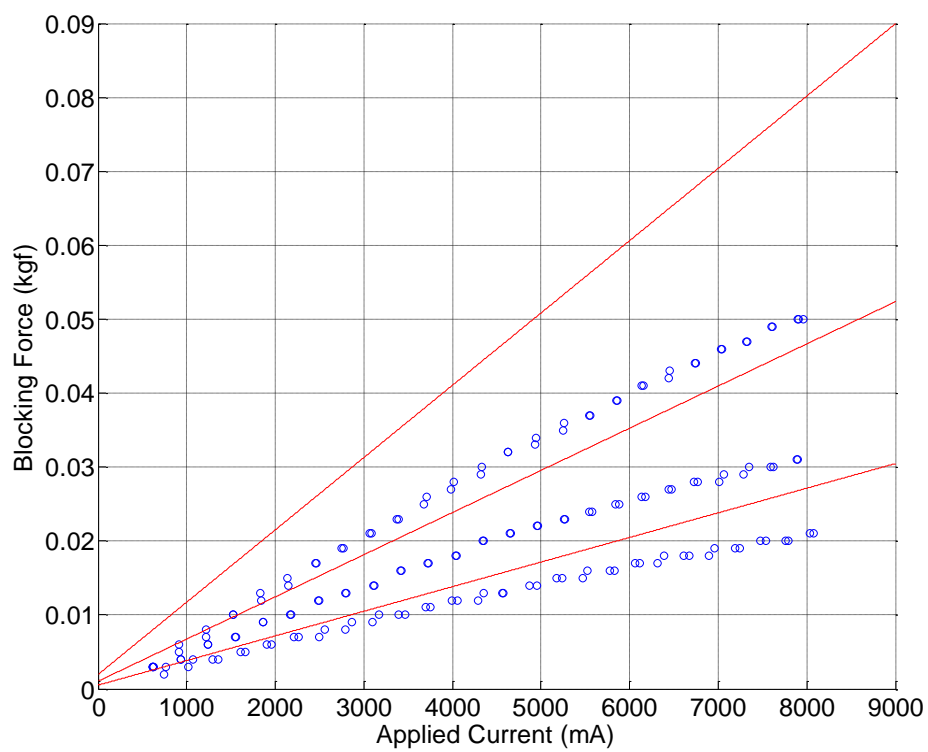
Figure 48: Global model fitting results for HS IV samples.

Appendix B – Sensing Experimental Data
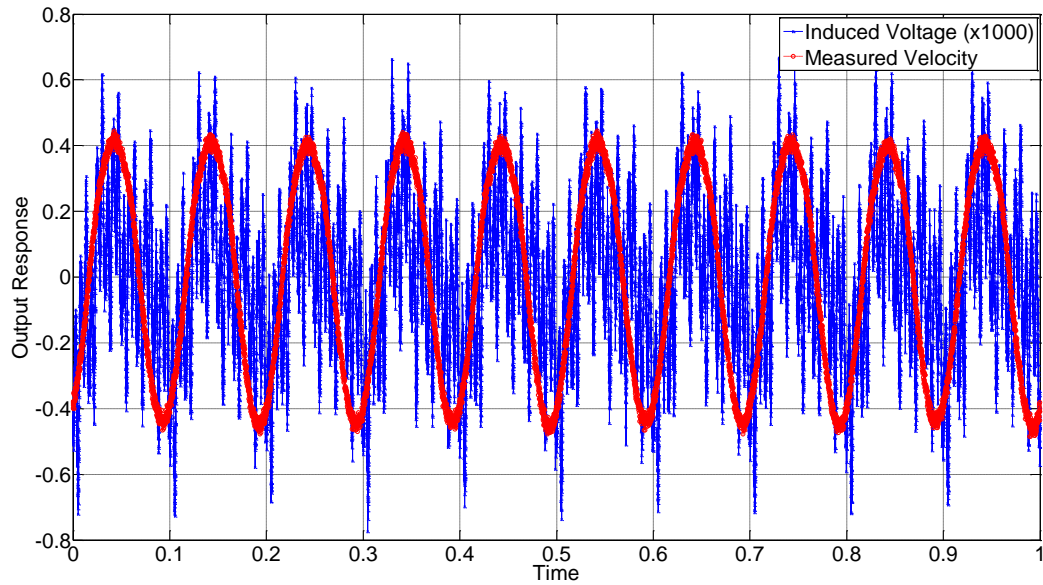
Figure 49: Laser displacement sensor and pick-up coil induced EMF signals for HS II 20% excited at 10 Hz.
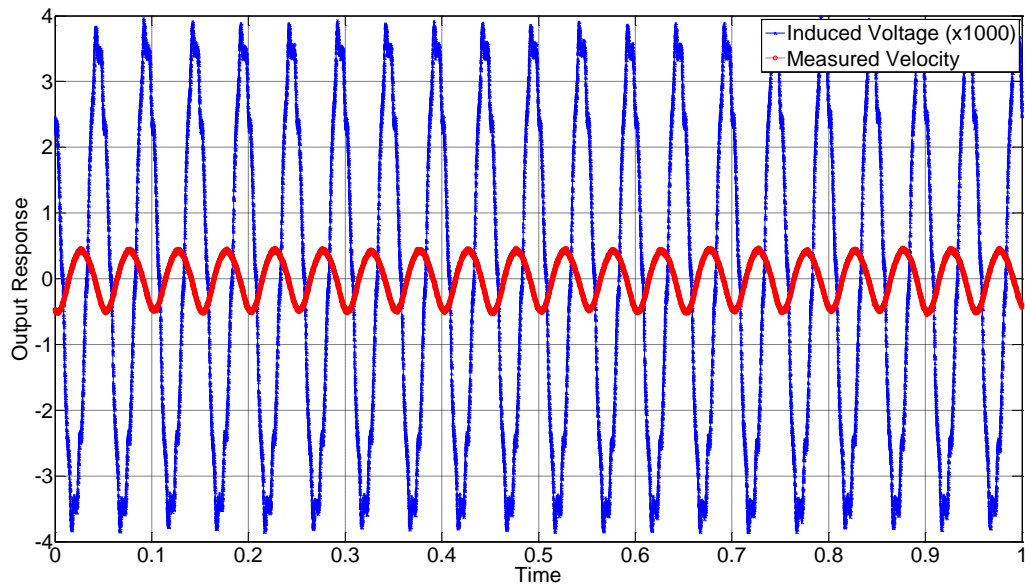
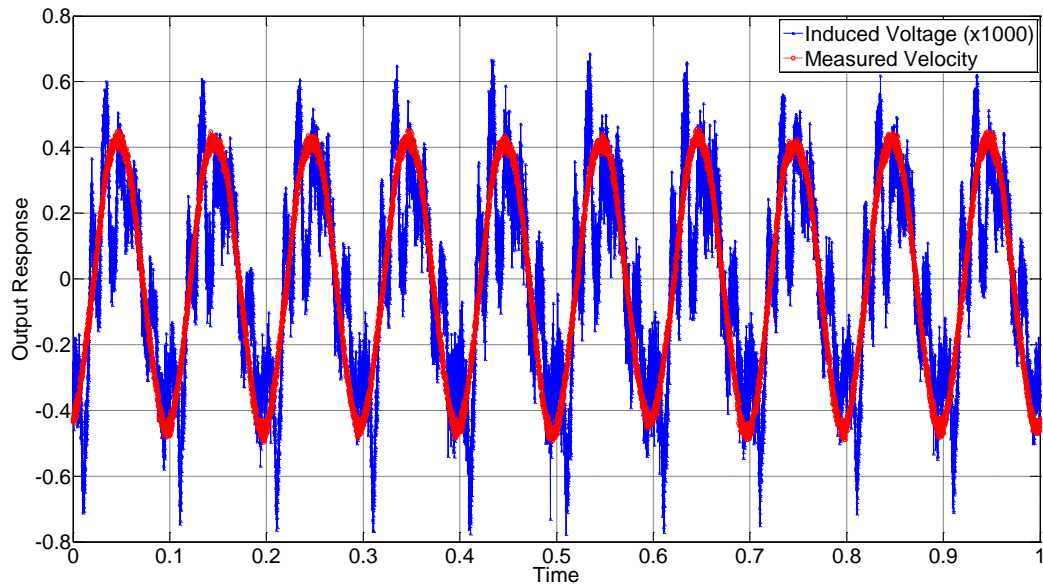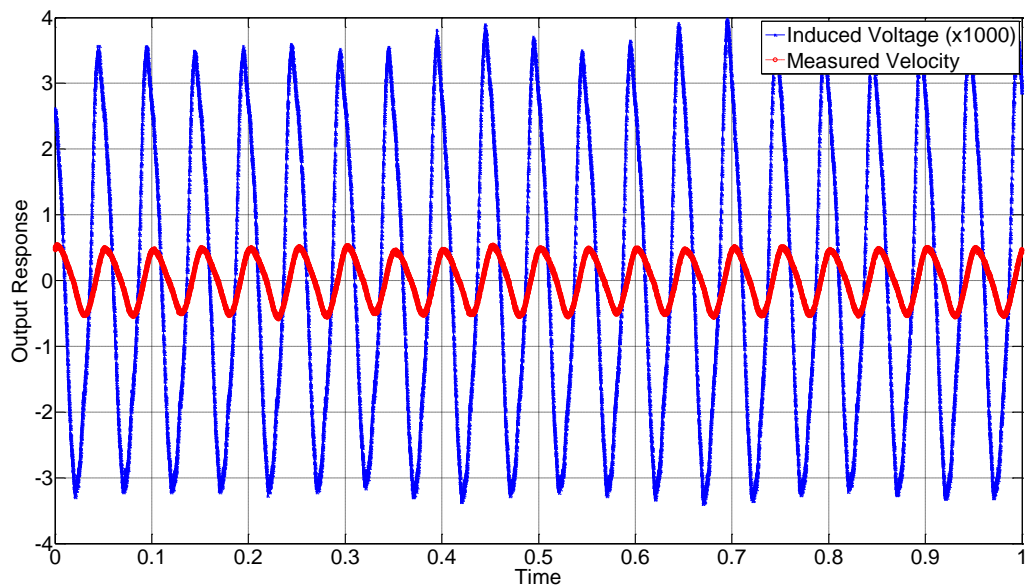**Figure 50: Laser displacement sensor and pick-up coil induced EMF signals for HS II 20% excited at 20 Hz.**
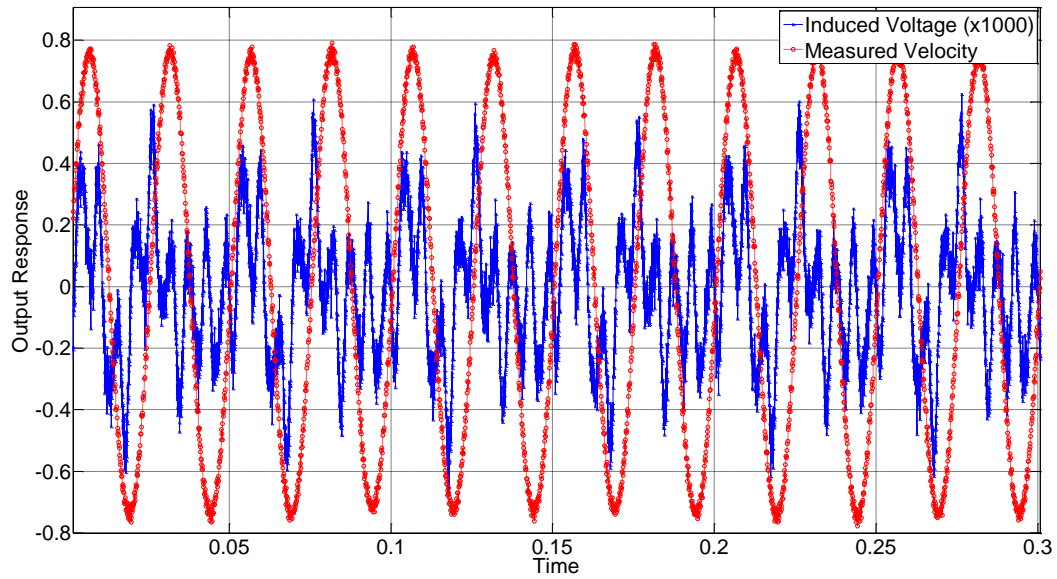
Figure 51: Laser displacement sensor and pick-up coil induced EMF signals for HS II 20% excited at 40 Hz.
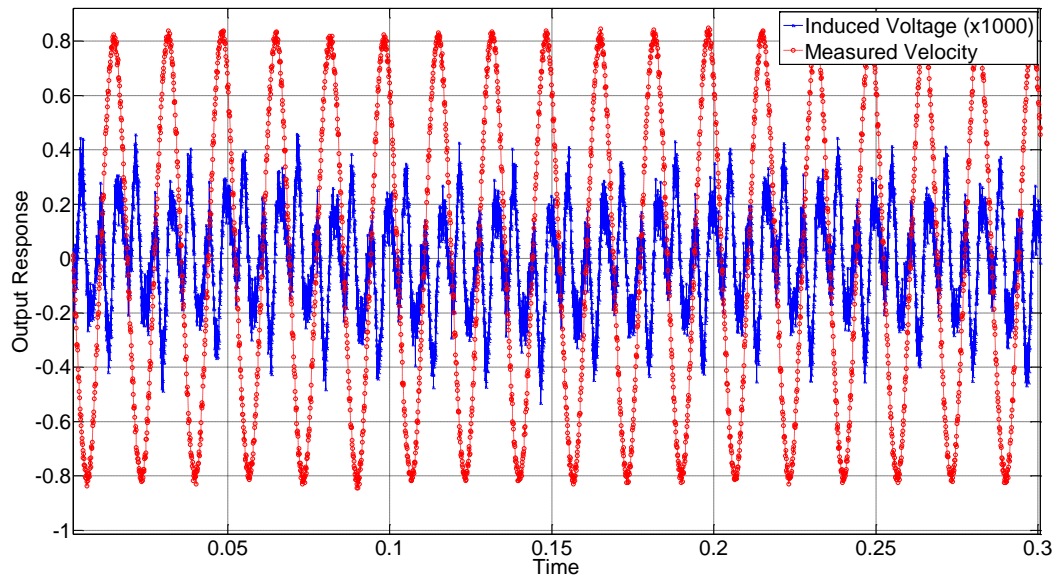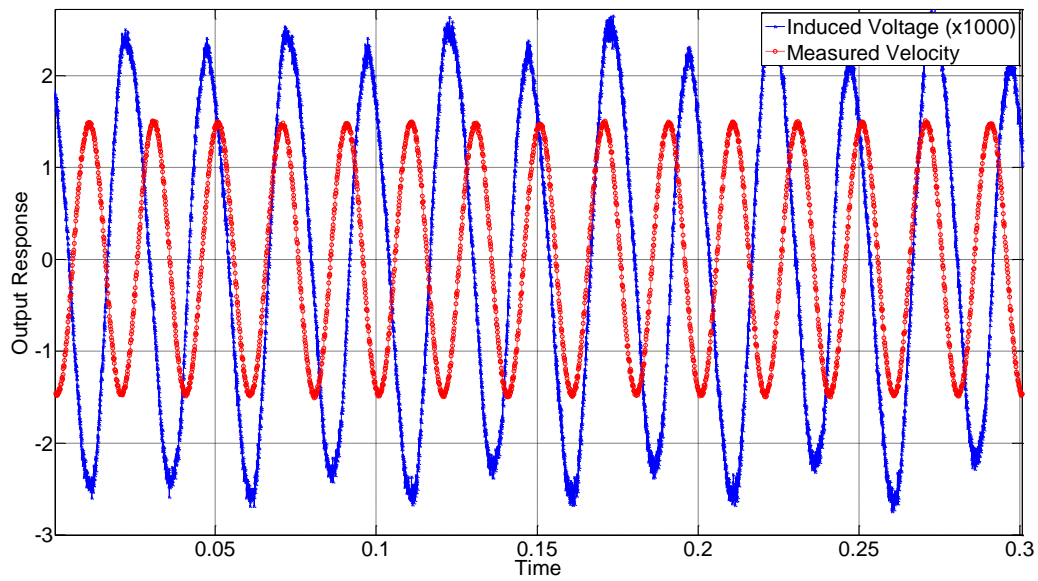

Figure 52: Laser displacement sensor and pick-up coil induced EMF signals for HS II 20% excited at 60 Hz.
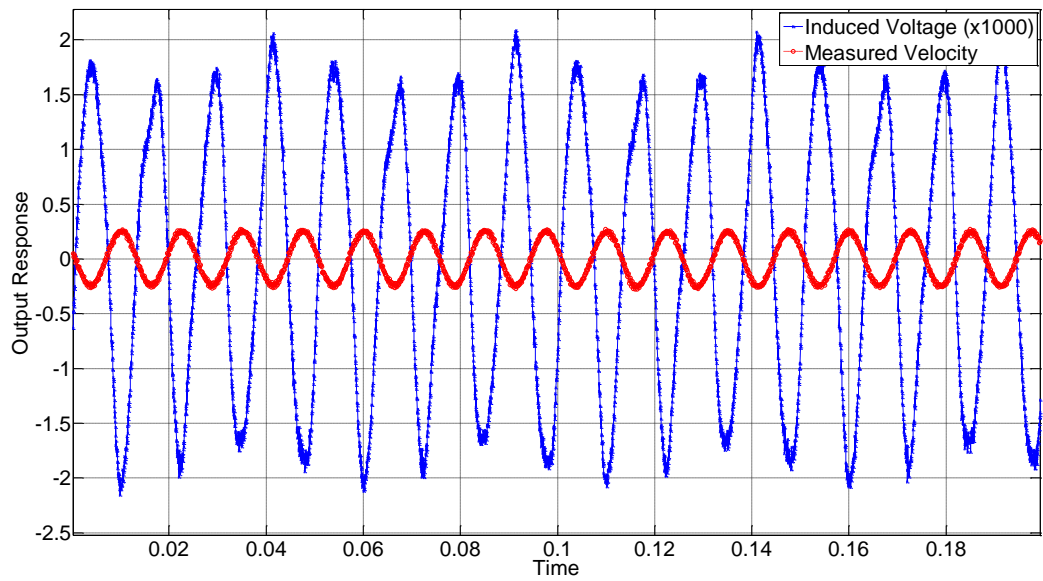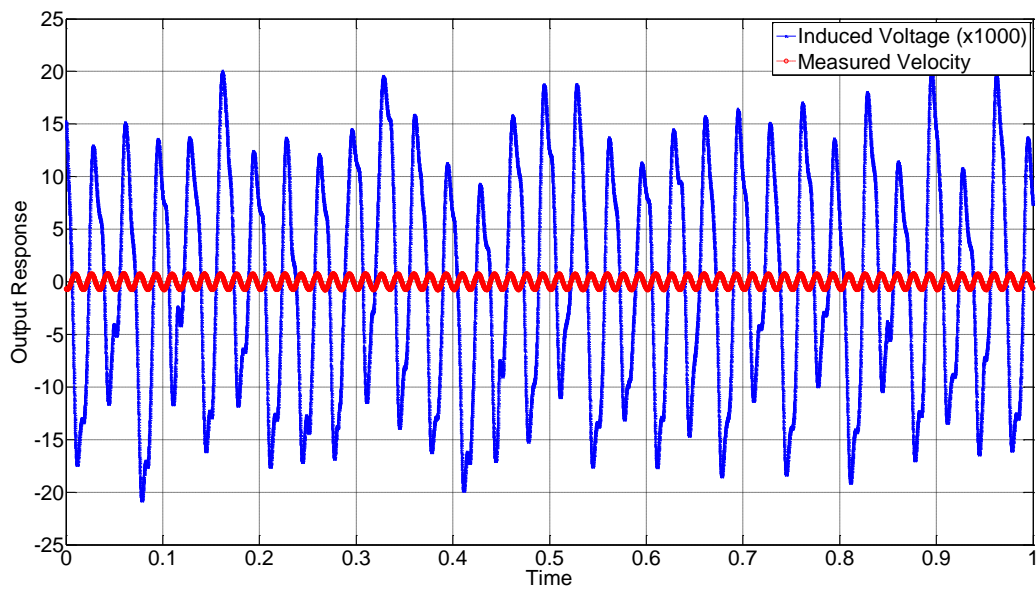
Figure 53: Laser displacement sensor and pick-up coil induced EMF signals for HS II 20% excited at 80 Hz.
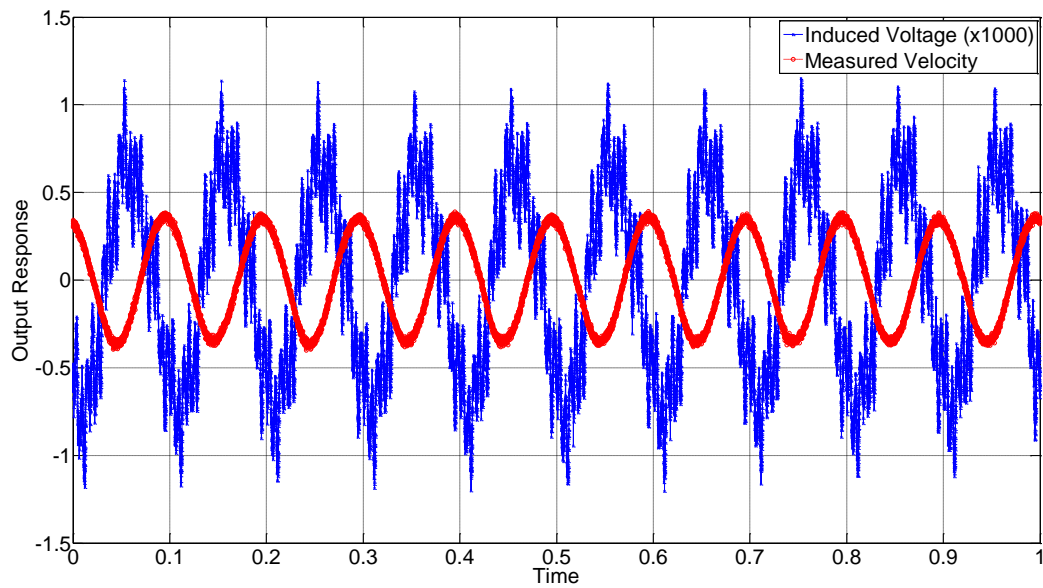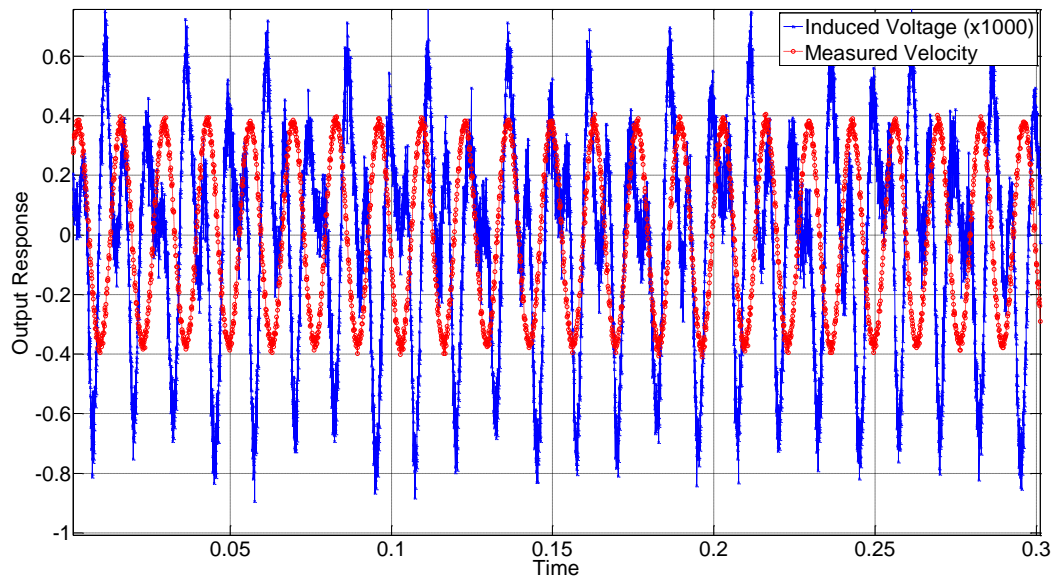

Figure 54: Laser displacement sensor and pick-up coil induced EMF signals for HS II 30% excited at 10 Hz.
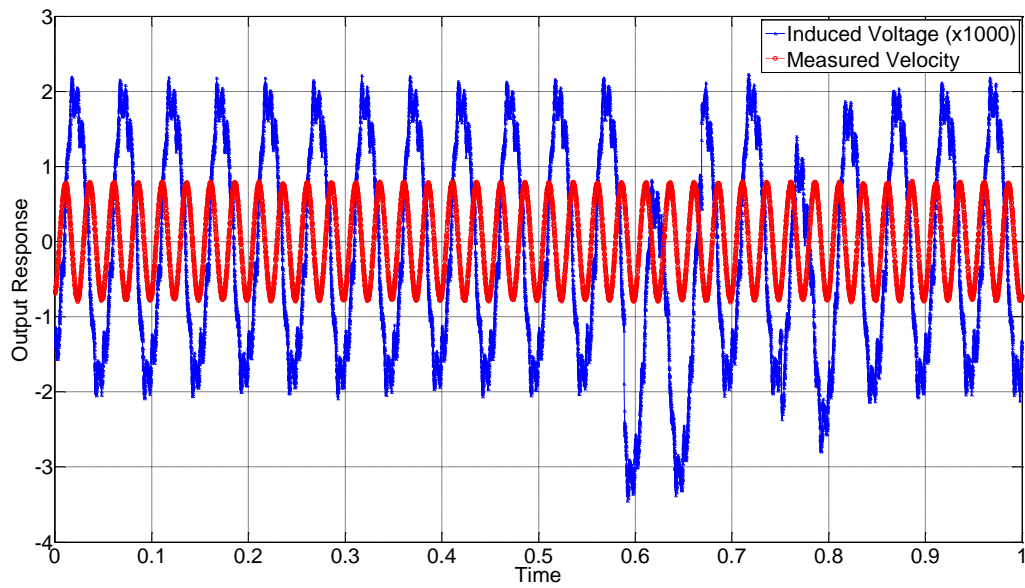
Figure 55: Laser displacement sensor and pick-up coil induced EMF signals for HS II 30% excited at 20 Hz.
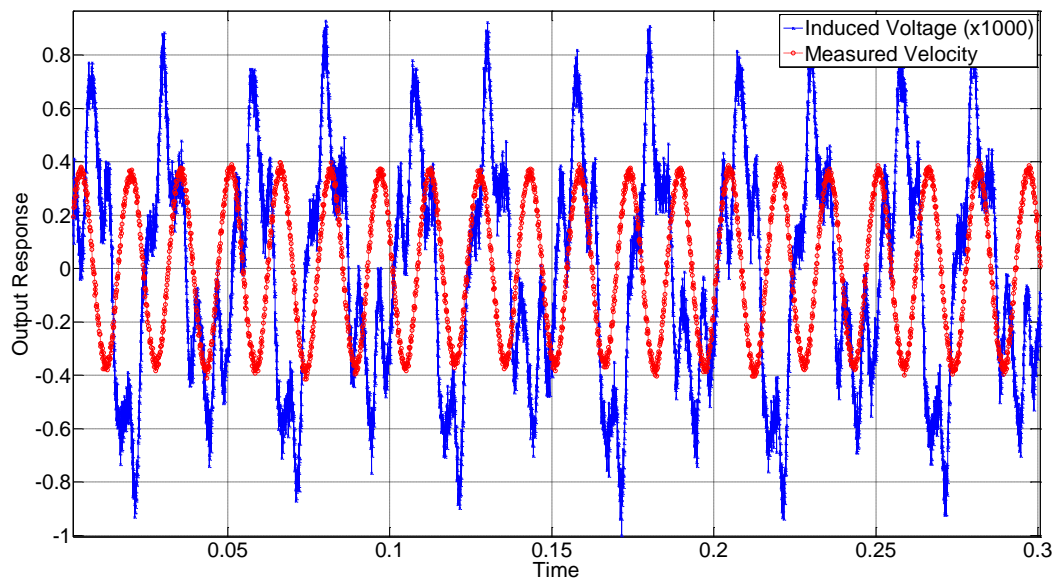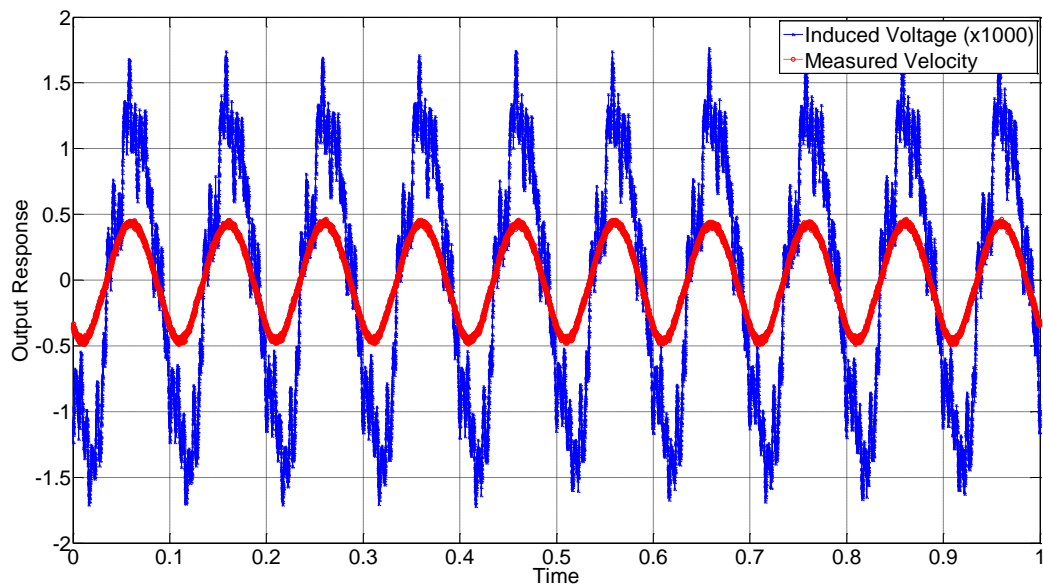

Figure 56: Laser displacement sensor and pick-up coil induced EMF signals for HS II 30% excited at 40 Hz.
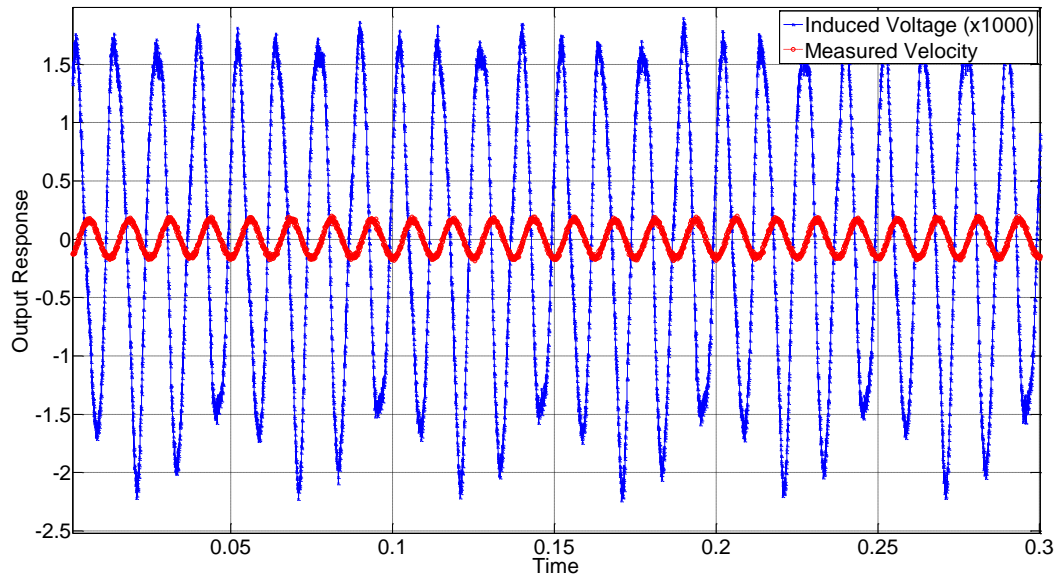
Figure 57: Laser displacement sensor and pick-up coil induced EMF signals for HS II 30% excited at 80 Hz.
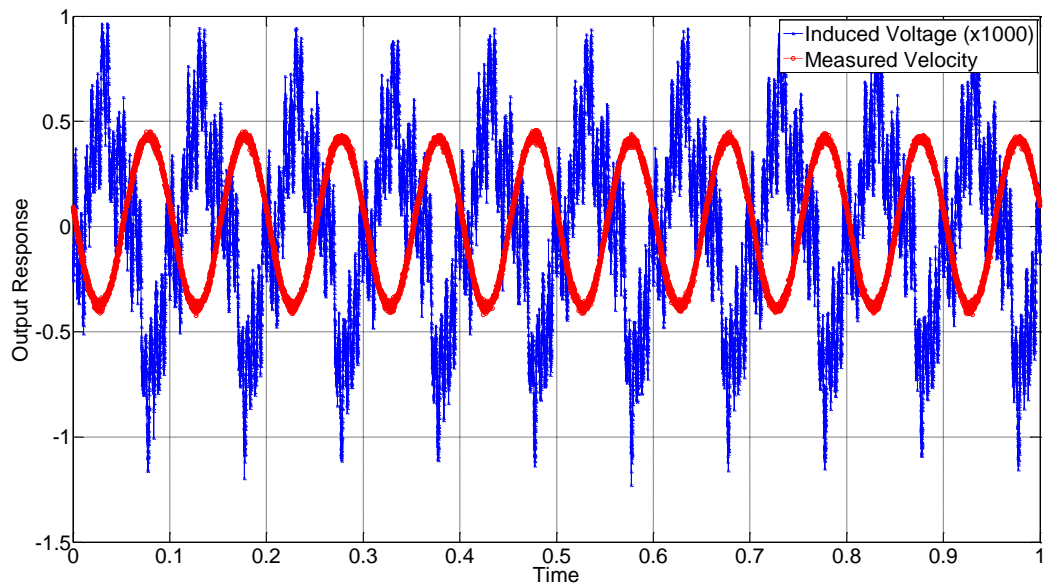
Figure 58: Laser displacement sensor and pick-up coil induced EMF signals for HS III 20% excited at 10 Hz.
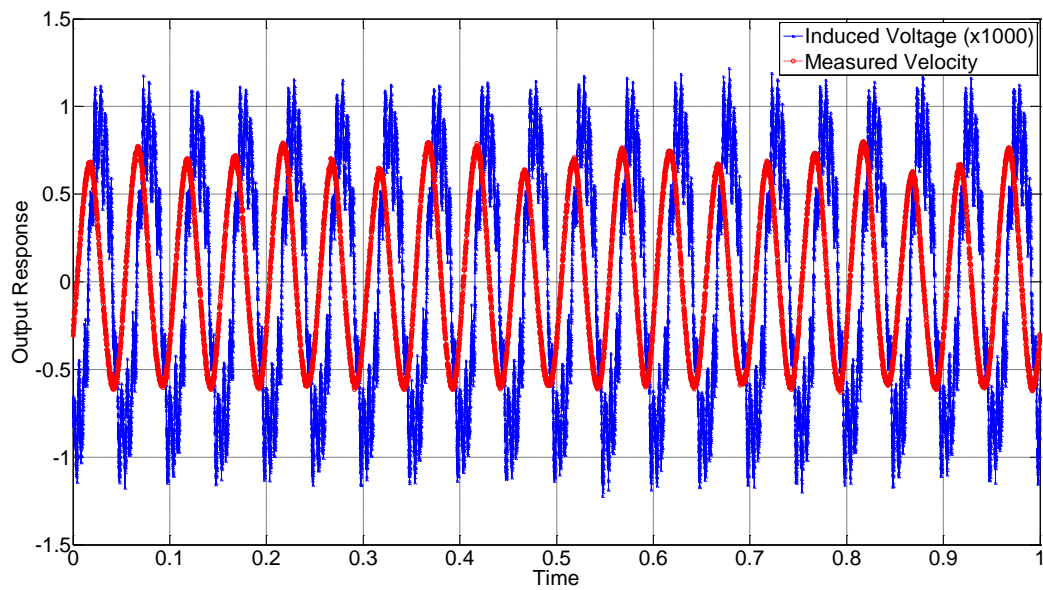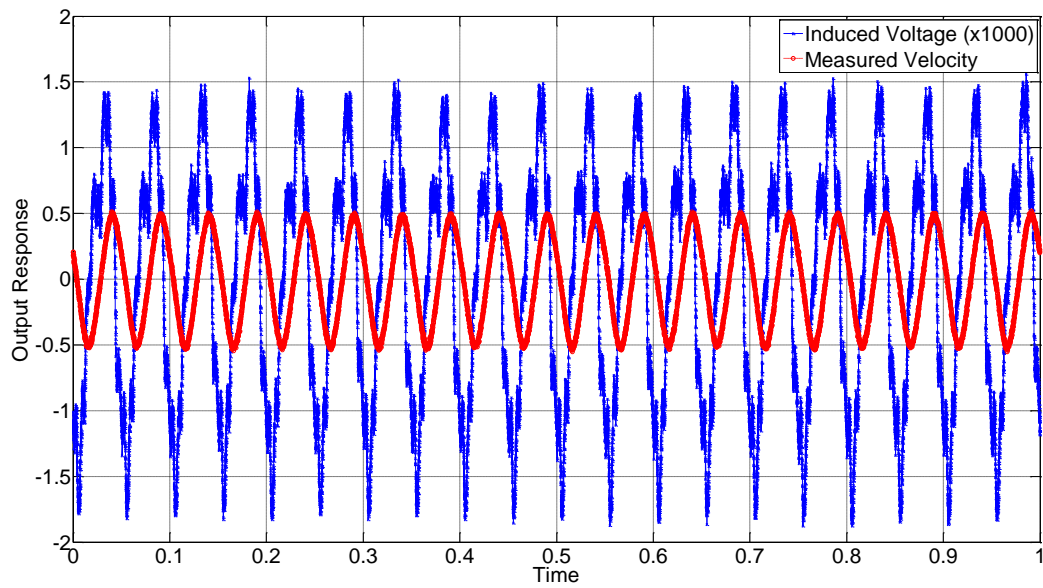

Figure 59: Laser displacement sensor and pick-up coil induced EMF signals for HS III 20% excited at 20 Hz.
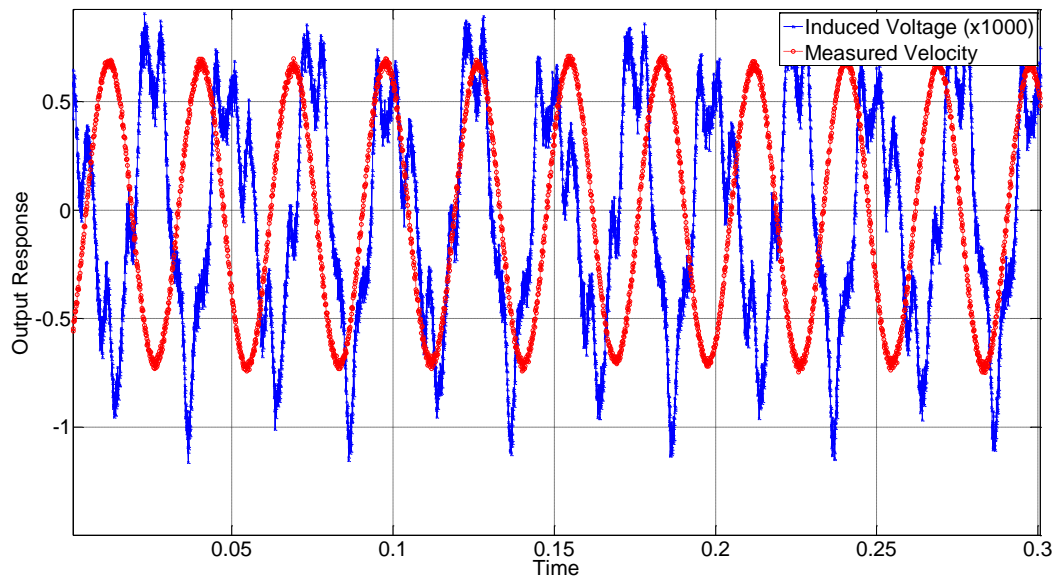
Figure 60: Laser displacement sensor and pick-up coil induced EMF signals for HS III 20% excited at 40 Hz.
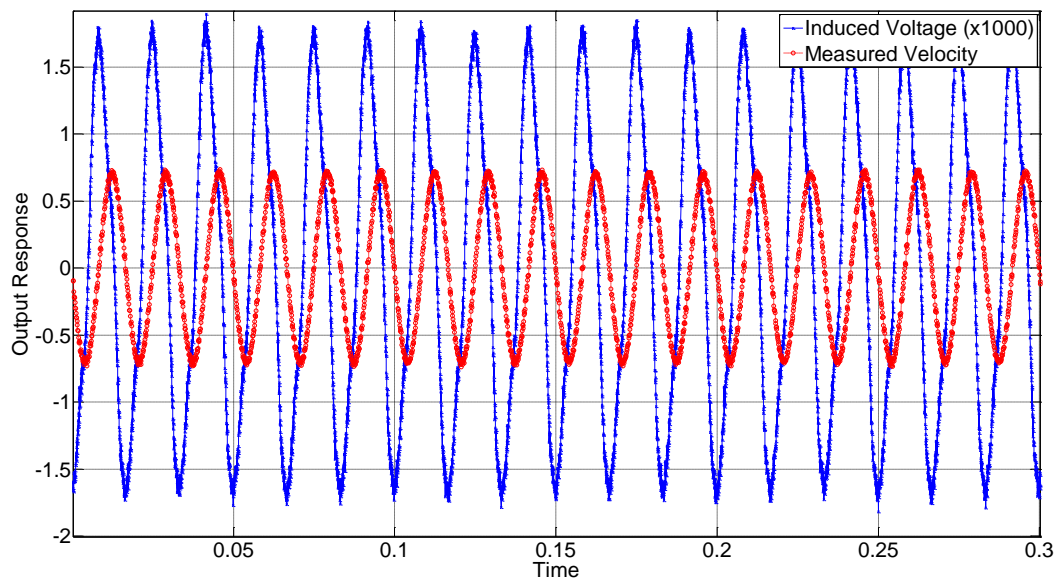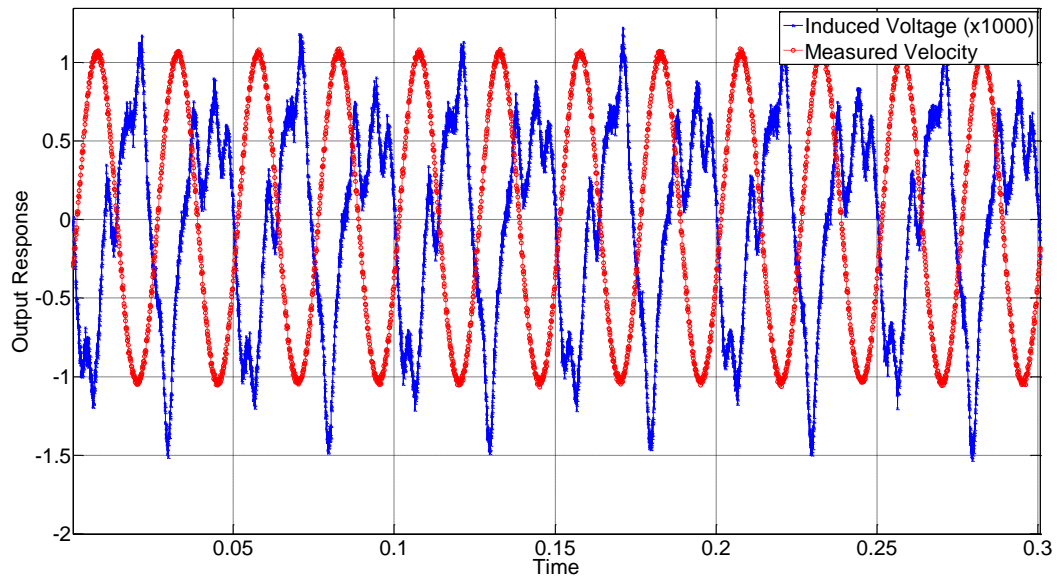

Figure 61: Laser displacement sensor and pick-up coil induced EMF signals for HS III 20% excited at 60 Hz.
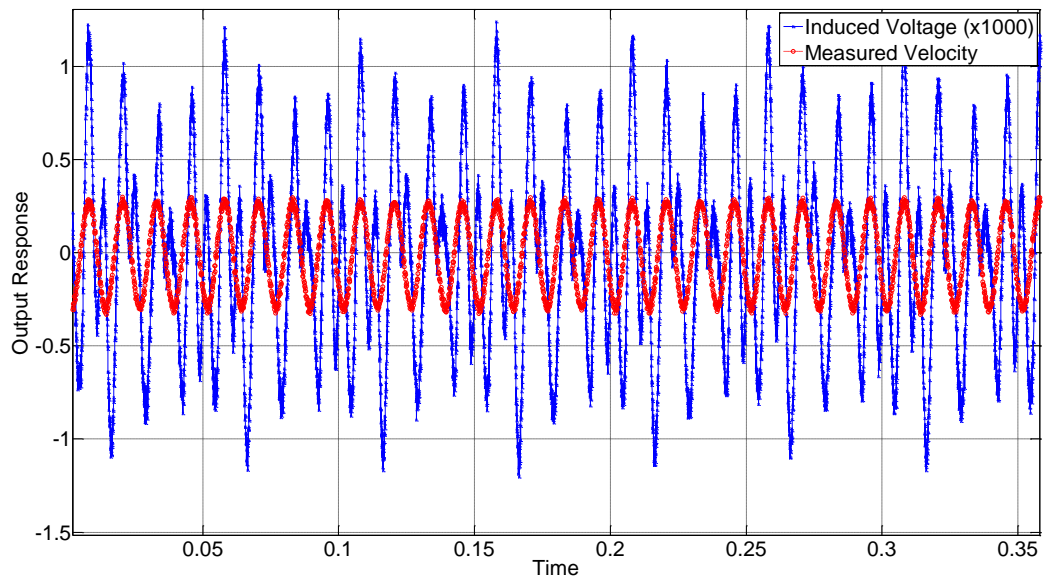
Figure 62: Laser displacement sensor and pick-up coil induced EMF signals for HS III 20% excited at 80 Hz.
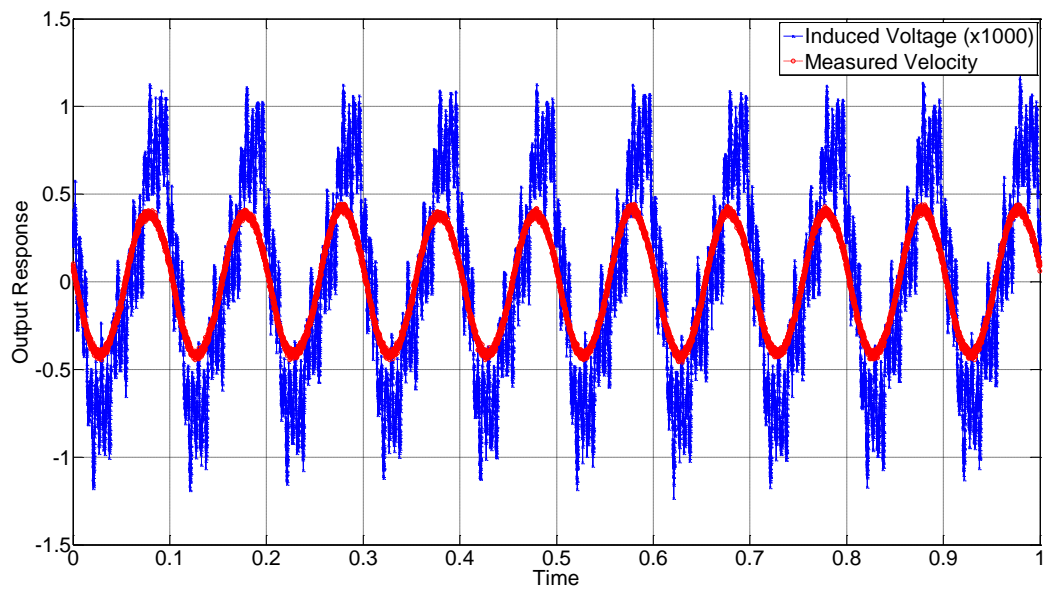
Figure 63: Laser displacement sensor and pick-up coil induced EMF signals for HS III 30% excited at 10 Hz.
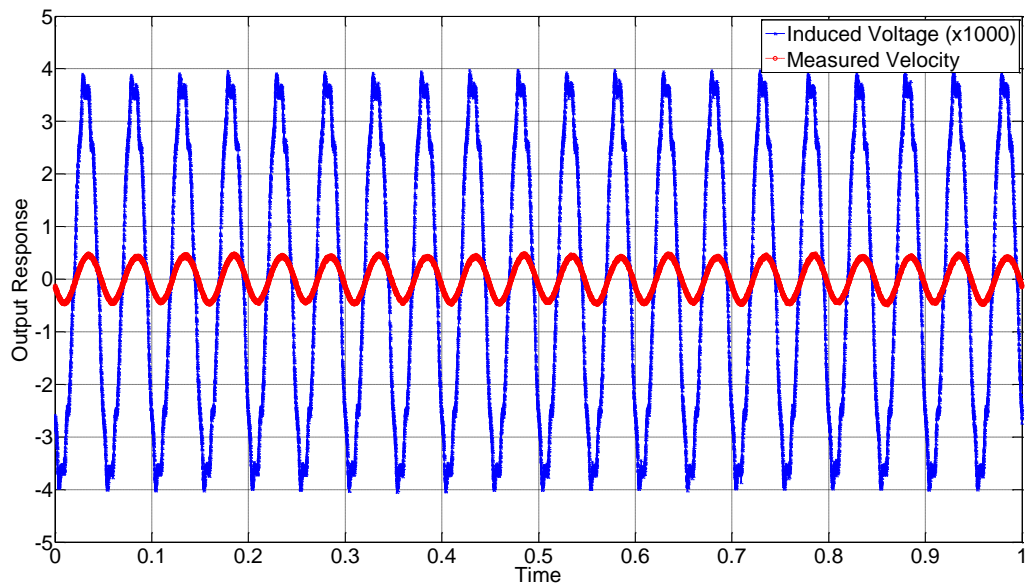
Figure 64: Laser displacement sensor and pick-up coil induced EMF signals for HS III 30% excited at 20 Hz.
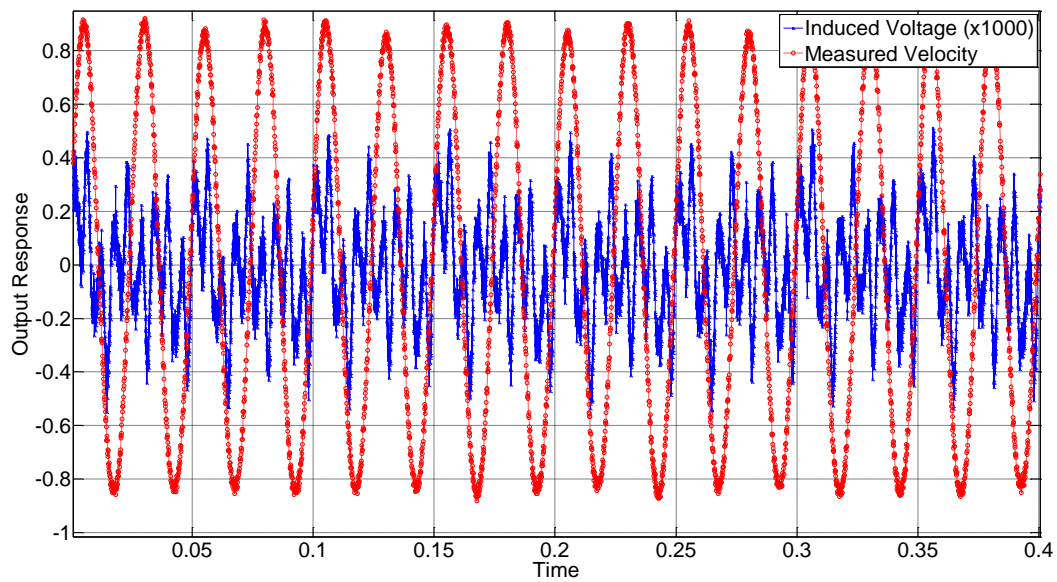
Figure 65: Laser displacement sensor and pick-up coil induced EMF signals for HS III 30% excited at 40 Hz.
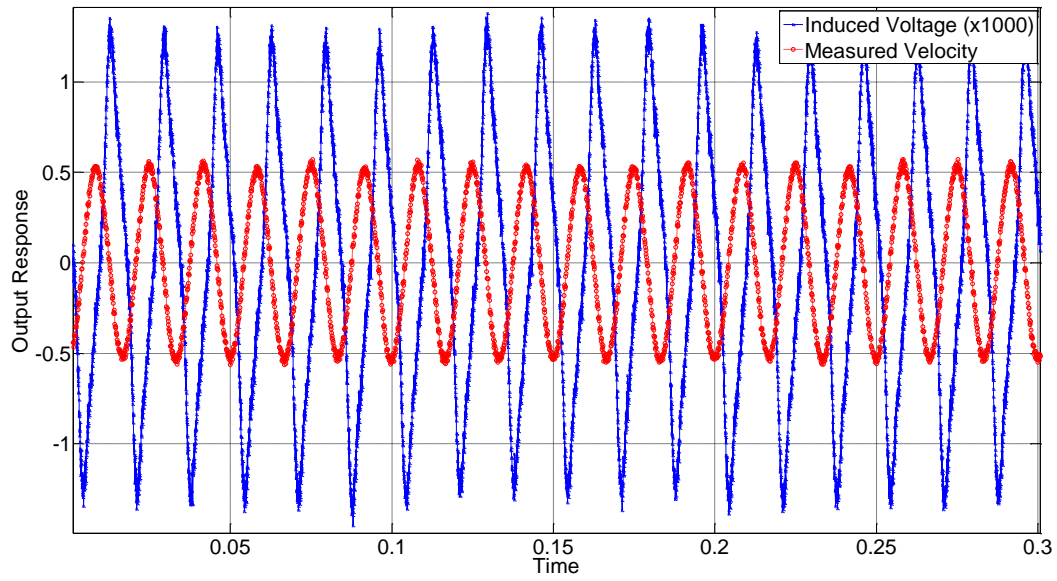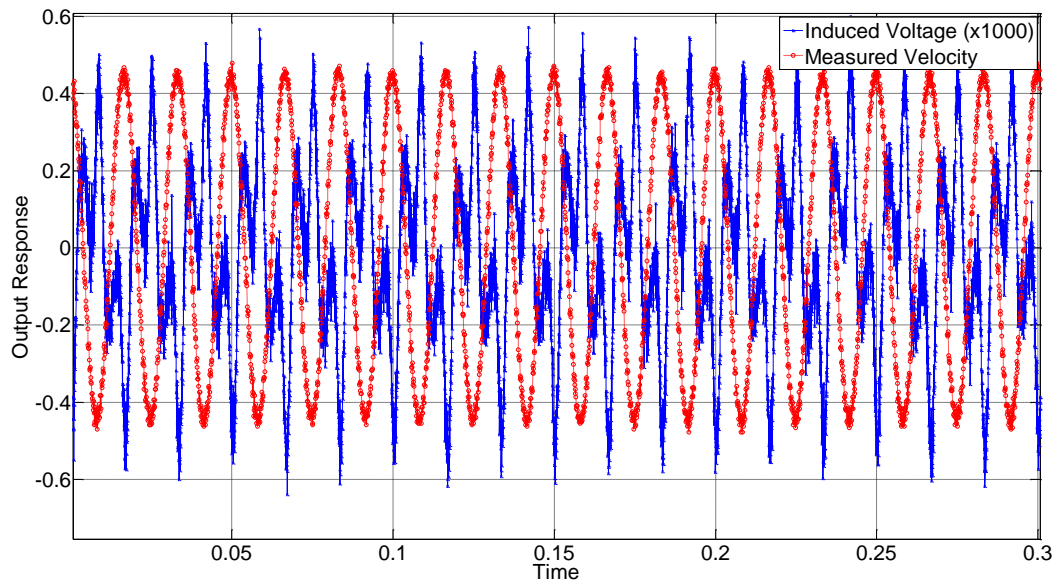
Figure 66: Laser displacement sensor and pick-up coil induced EMF signals for HS III 20% excited at 60 Hz.
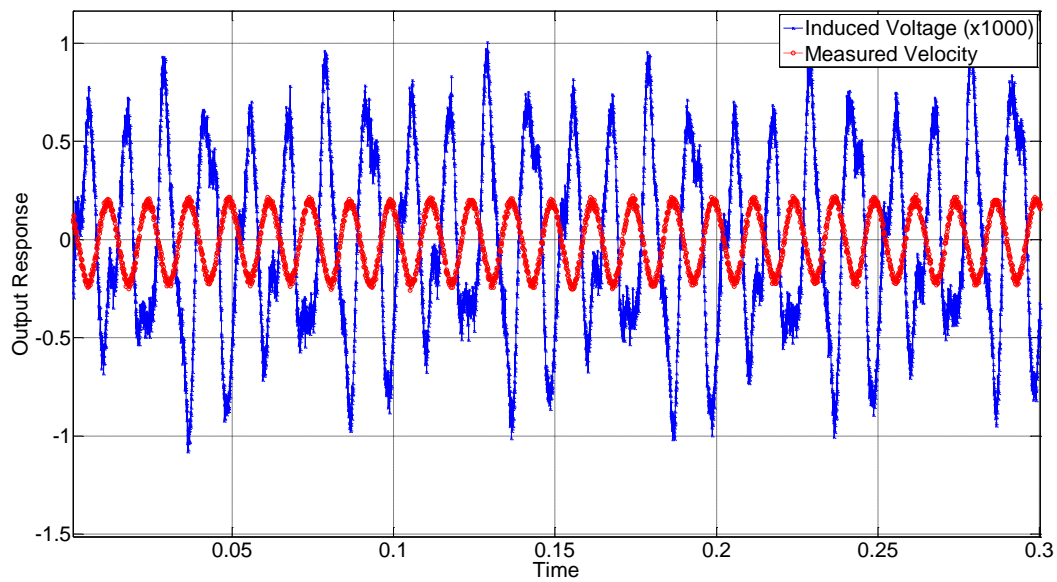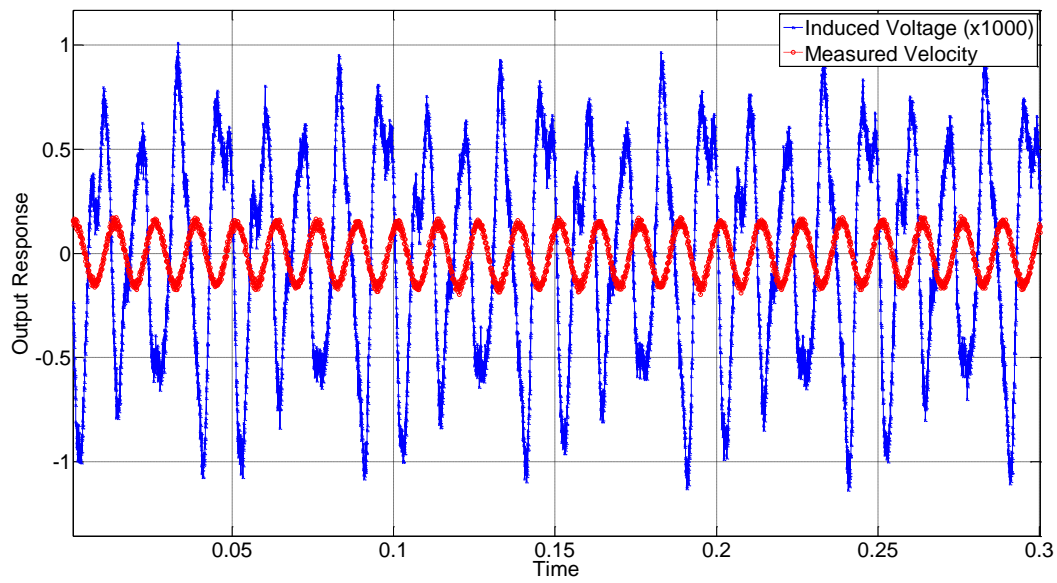

Figure 67: Laser displacement sensor and pick-up coil induced EMF signals for HS III 20% excited at 80 Hz.

Figure 68: Laser displacement sensor and pick-up coil induced EMF signals for HS IV 20% excited at 10 Hz.

Figure 69: Laser displacement sensor and pick-up coil induced EMF signals for HS IV 20% excited at 20 Hz.

Figure 70: Laser displacement sensor and pick-up coil induced EMF signals for HS IV 20% excited at 40 Hz.

Figure 71: Laser displacement sensor and pick-up coil induced EMF signals for HS IV 20% excited at 60 Hz.

Figure 72: Laser displacement sensor and pick-up coil induced EMF signals for HS IV 20% excited at 80 Hz.

Figure 73: Laser displacement sensor and pick-up coil induced EMF signals for HS IV 30% excited at 10 Hz.

Figure 74: Laser displacement sensor and pick-up coil induced EMF signals for HS IV 30% excited at 20 Hz.

Figure 75: Laser displacement sensor and pick-up coil induced EMF signals for HS IV 30% excited at 40 Hz.

Figure 76: Laser displacement sensor and pick-up coil induced EMF signals for HS IV 20% excited at 60 Hz.

Figure 77: Laser displacement sensor and pick-up coil induced EMF signals for HS IV 20% excited at 80 Hz.

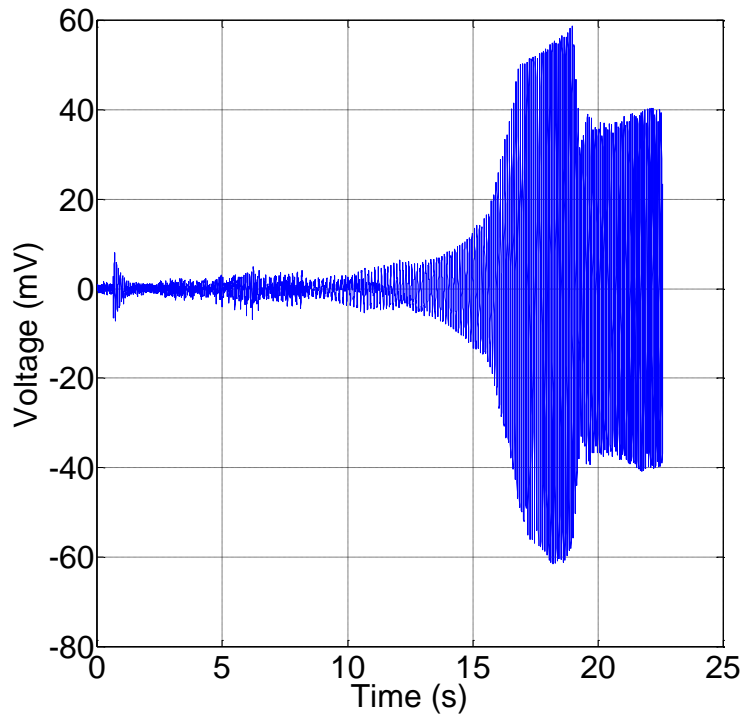# Appendix C – Energy Harvesting Experimental Data
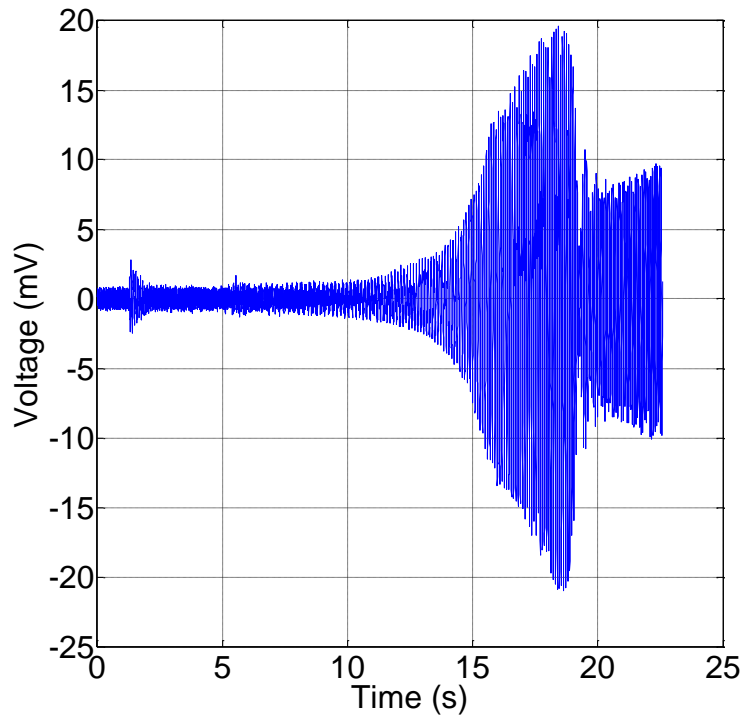
Figure 78: Voltage induced within the pick-up coil for HS II 10% cantilevered beam vibration sine sweep signal.
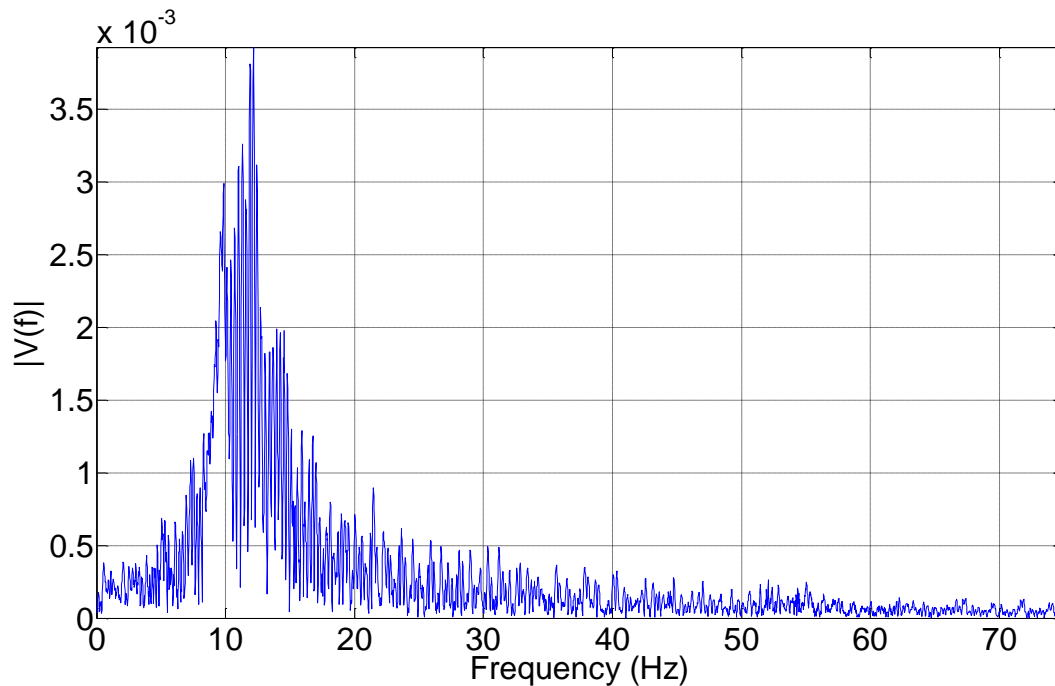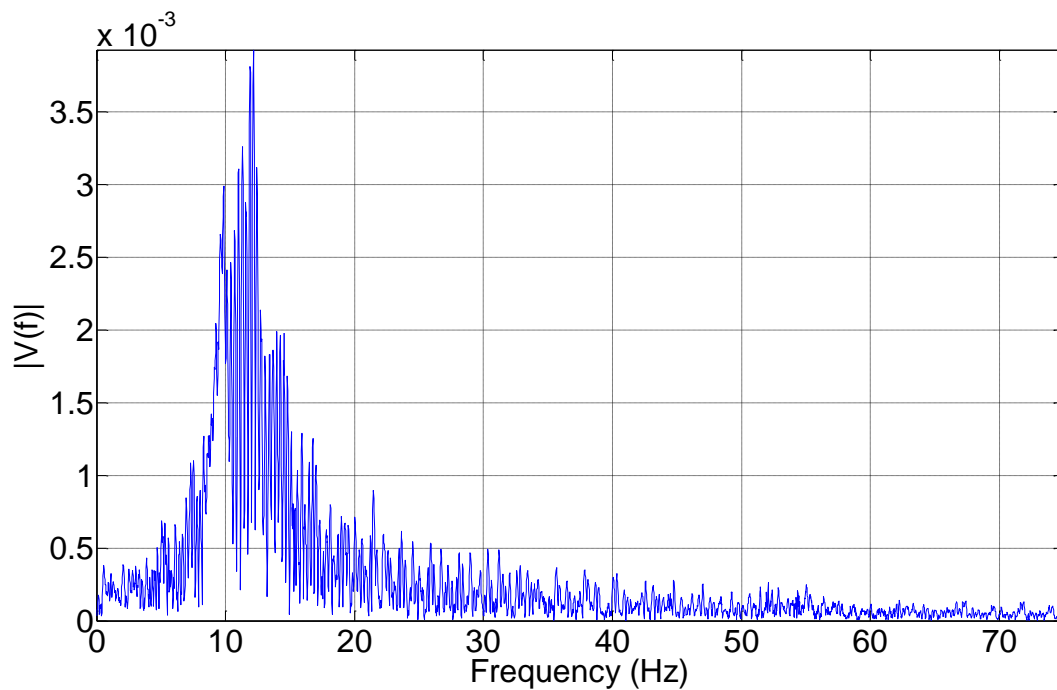

Figure 79: FFT of the induced voltage as a function of time indicating the ideal frequency for operation of this HS II 10% sample as an energy harvesting is around 11.5 Hz.
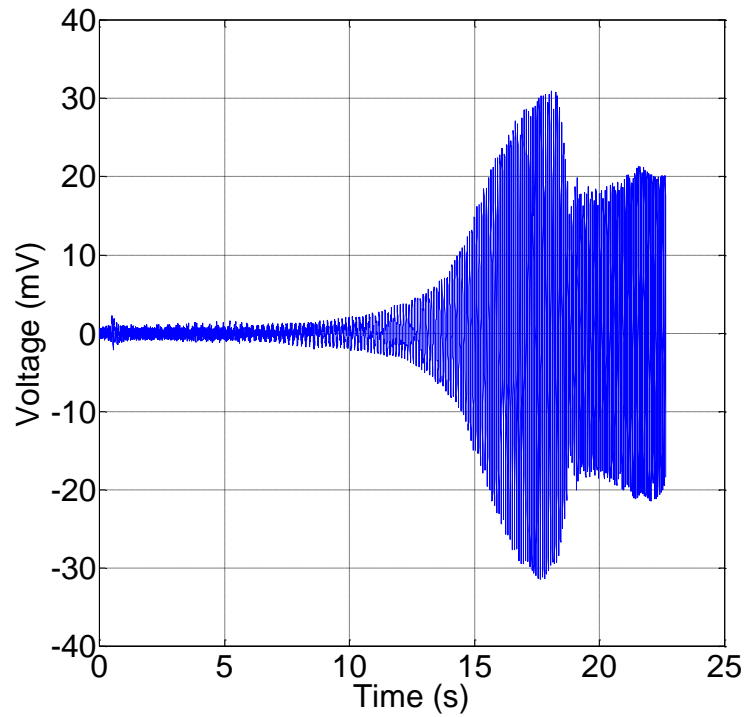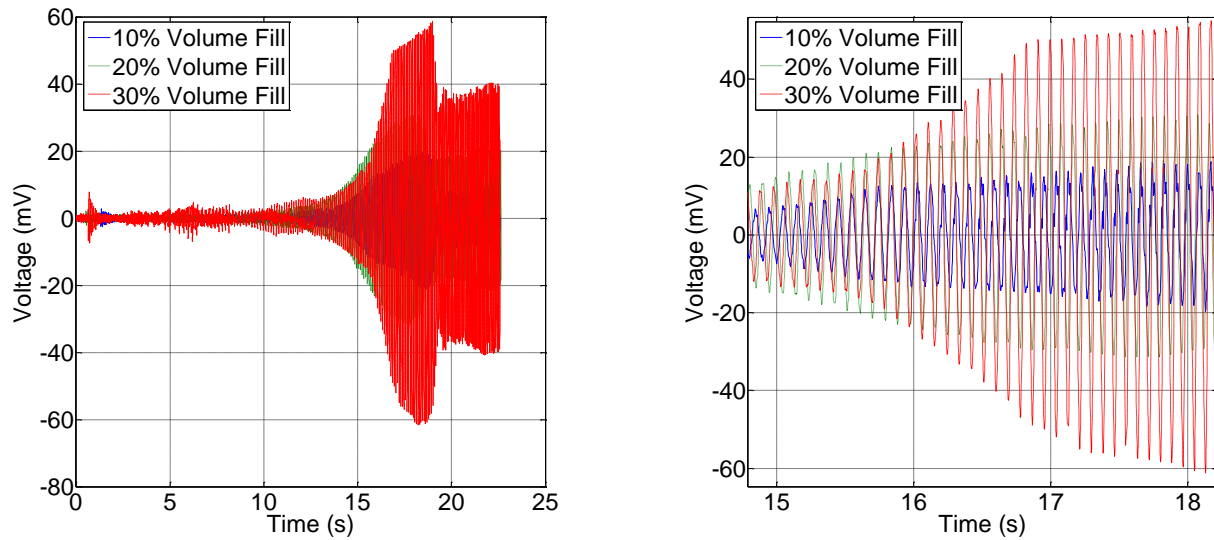
Figure 80: Voltage induced within the pick-up coil for HS II 20% cantilevered beam vibration sine sweep signal.
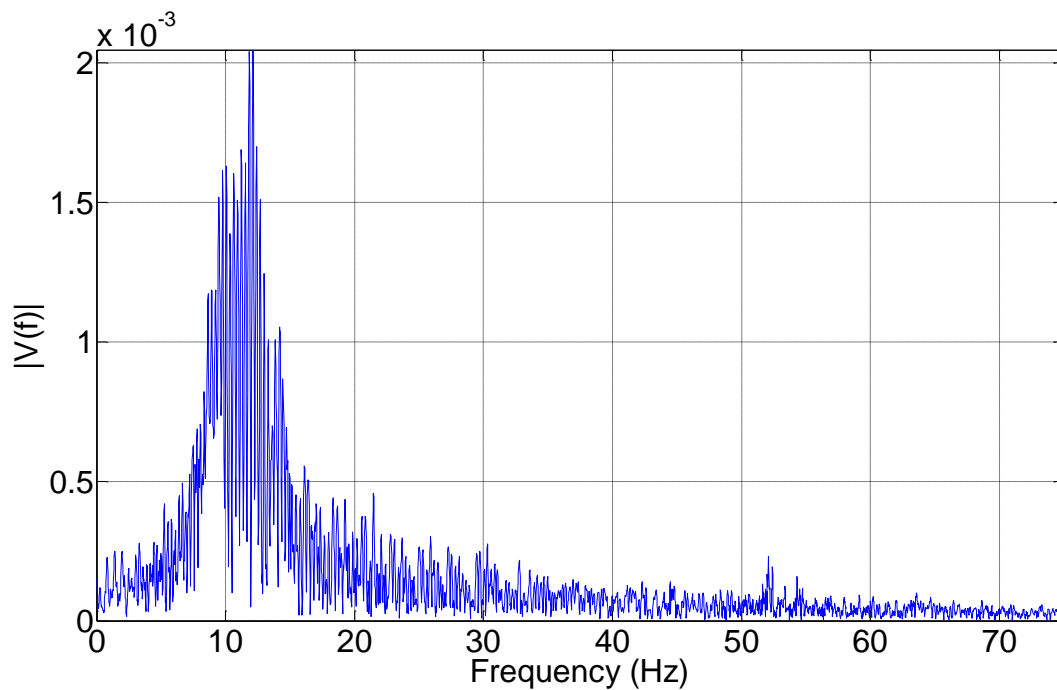
Figure 81: FFT of the induced voltage as a function of time indicating the ideal frequency for operation of this HS II 20% sample as an energy harvesting is around 12.14 Hz.

Figure 82: Voltage induced within the pick-up coil for HS II 30% cantilevered beam vibration sine sweep signal.

Figure 83: FFT of the induced voltage as a function of time indicating the ideal frequency for operation of this HS II 30% sample as an energy harvesting is around 12.17 Hz.

Figure 84: Comparison of the voltage induced within the pick-up coil for all HS II cantilevered beam vibration sine sweep signals, indicating that the peak-to-peak voltage increased with increasing volume fill percentage.

Figure 85: A more zoomed in view of Figure 83 indicating the difference in peak-to-peak voltage amplitudes among the different HS II samples.
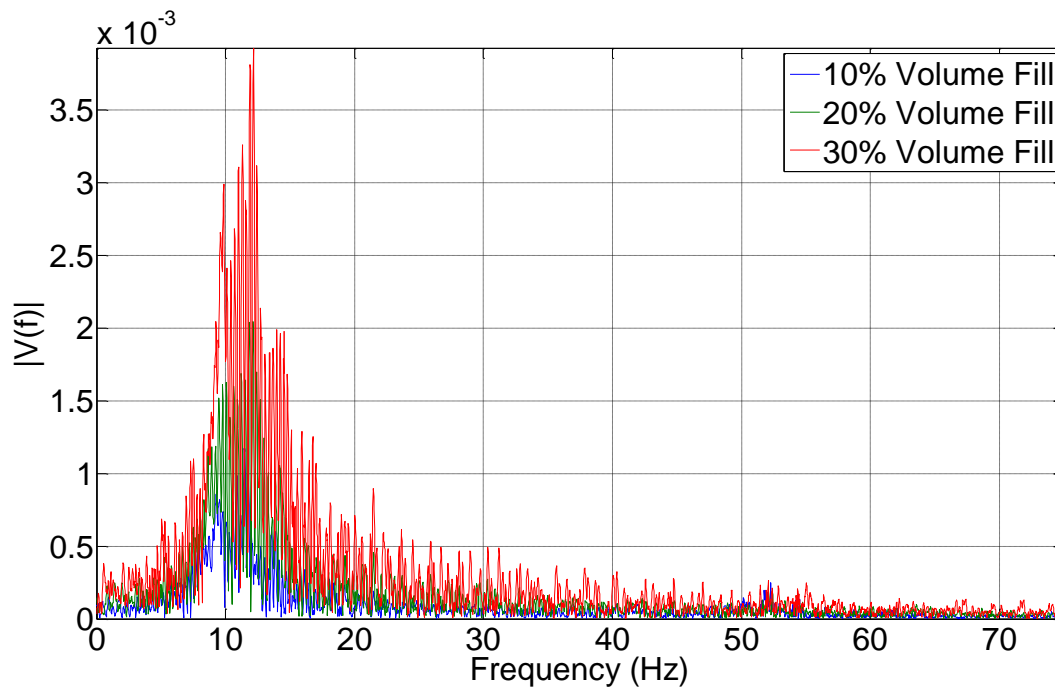

Figure 86: FFT signals for all of the HS II samples, again demonstrating that there is a difference in the maximum induced voltage for each sample and also indicating the slight shift in ideal operating frequencies for each sample.
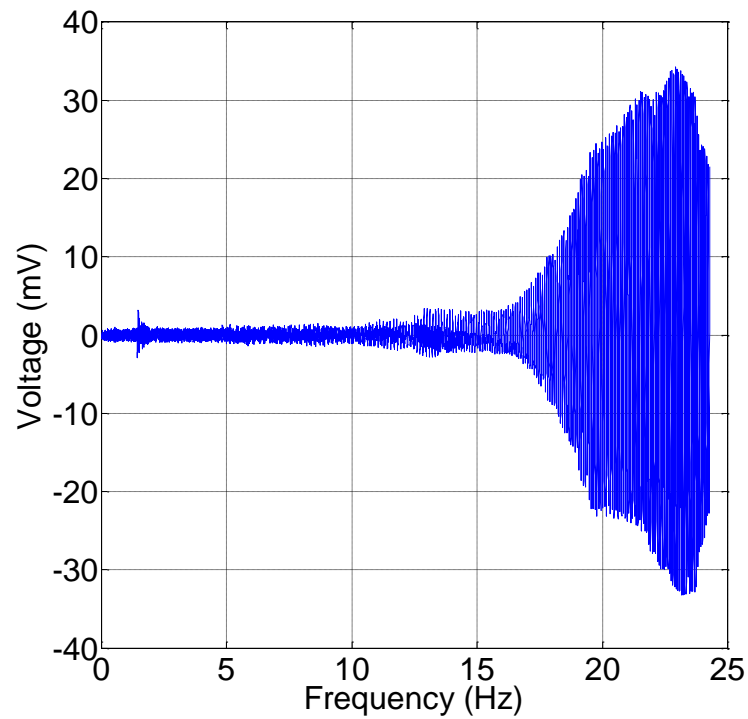
Figure 87: Voltage induced within the pick-up coil for HS III 20% cantilevered beam vibration sine sweep signal.
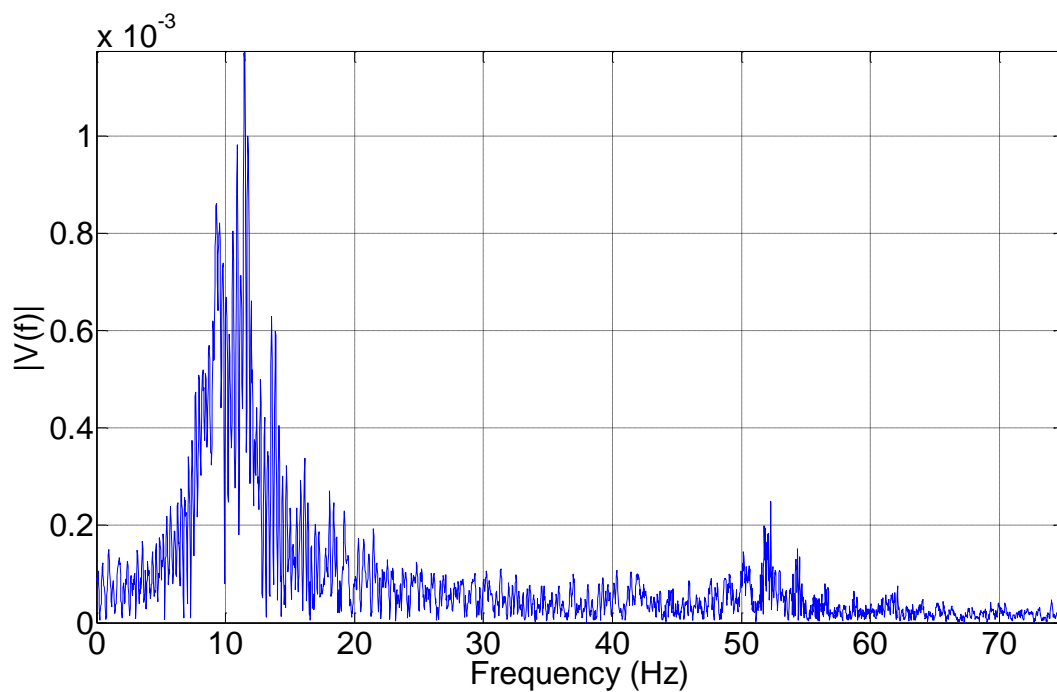

Figure 88: FFT of the induced voltage as a function of time indicating the ideal frequency for operation of this HS III 20% sample as an energy harvesting is around 12.63 Hz.
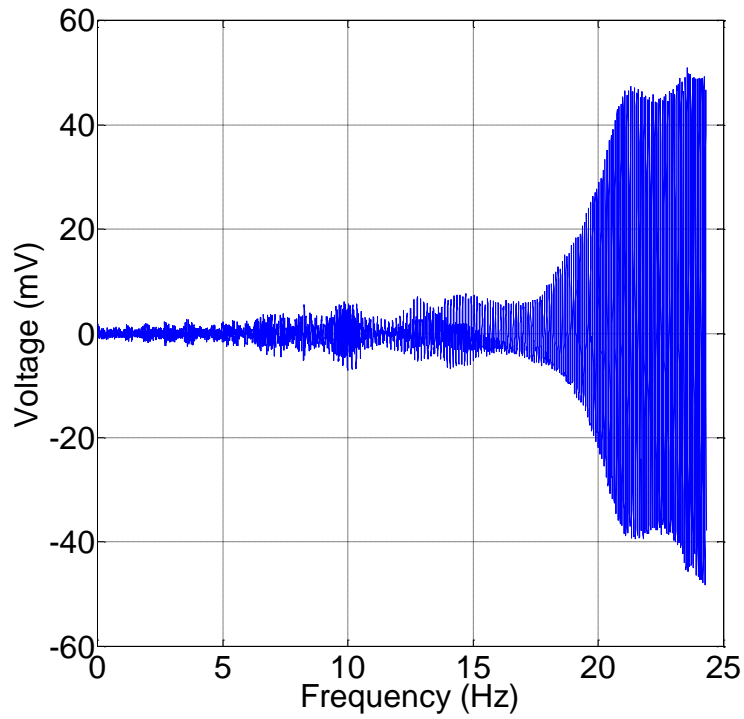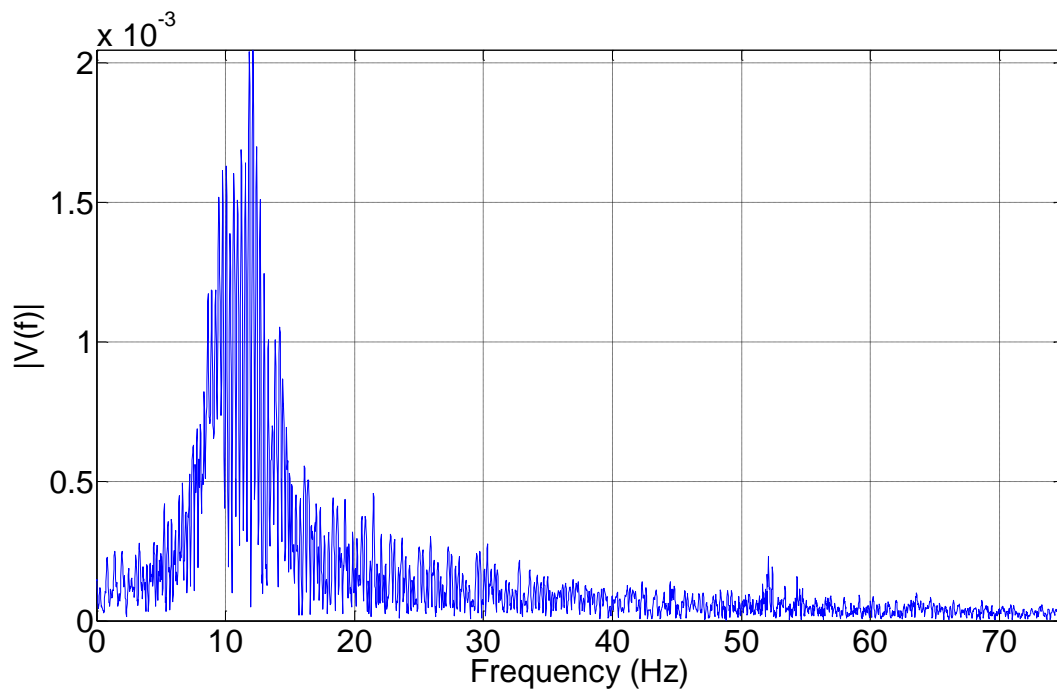
Figure 89: Voltage induced within the pick-up coil for HS III 30% cantilevered beam vibration sine sweep signal.

Figure 90: FFT of the induced voltage as a function of time indicating the ideal frequency for operation of this HS II 30% sample as an energy harvesting is around 12.37 Hz.
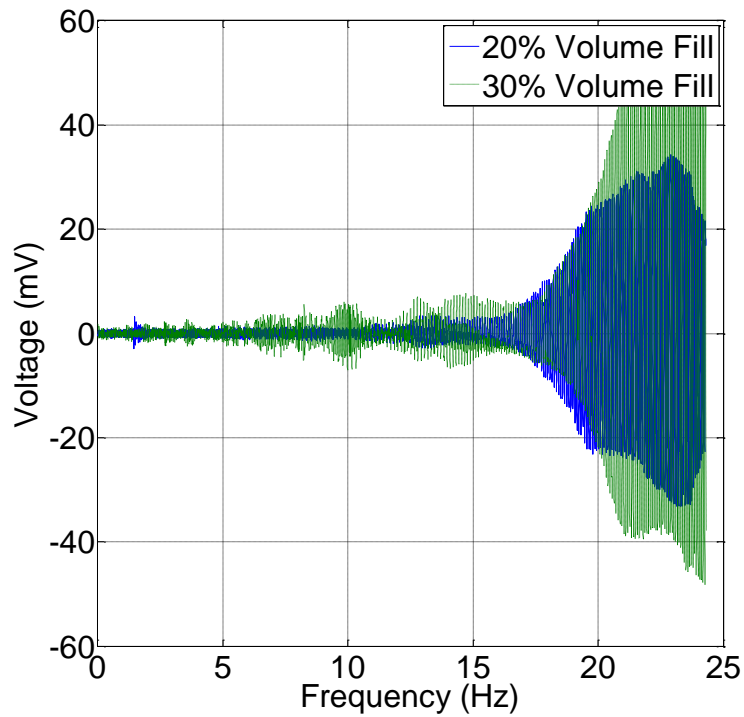
Figure 91: Comparison of the voltage induced within the pick-up coil for both HS III cantilevered beam vibration sine sweep signals, indicating that the peak-to-peak voltage increased with increasing volume fill percentage.
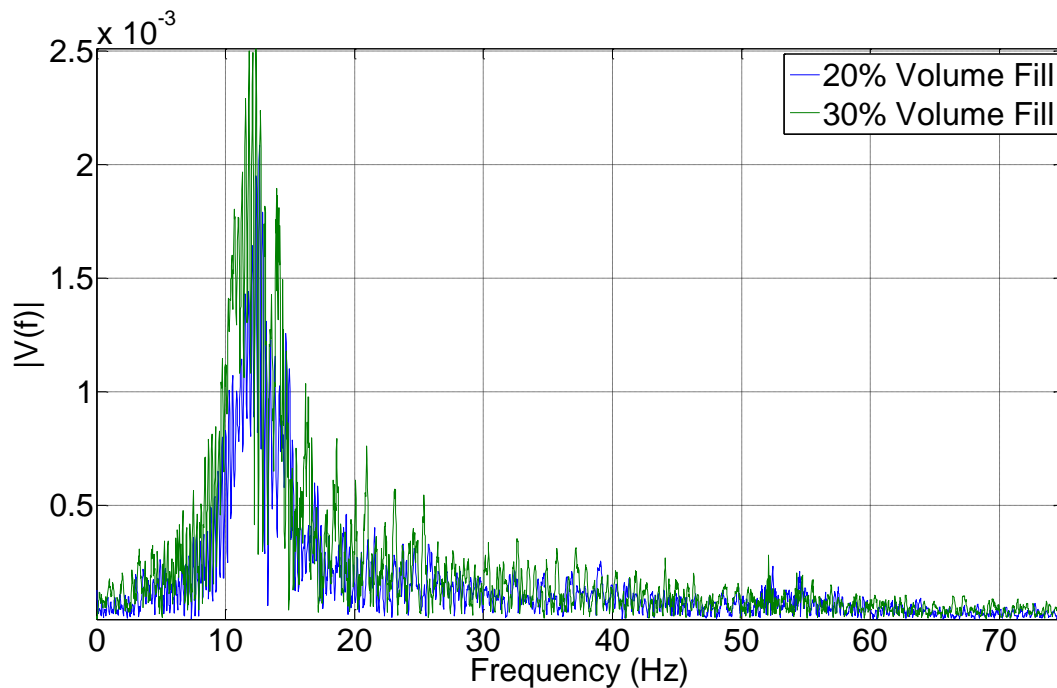

Figure 92: FFT signals for both of the HS III samples, again demonstrating that there is a difference in the maximum induced voltage for each sample and also indicating the slight shift in ideal operating frequencies for each sample.
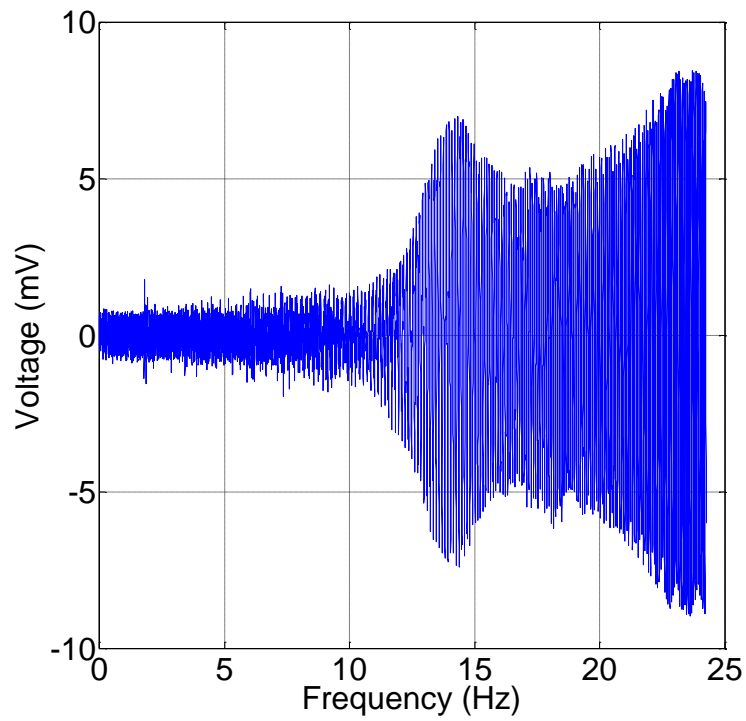
Figure 93: Voltage induced within the pick-up coil for HS IV 20% cantilevered beam vibration sine sweep signal.
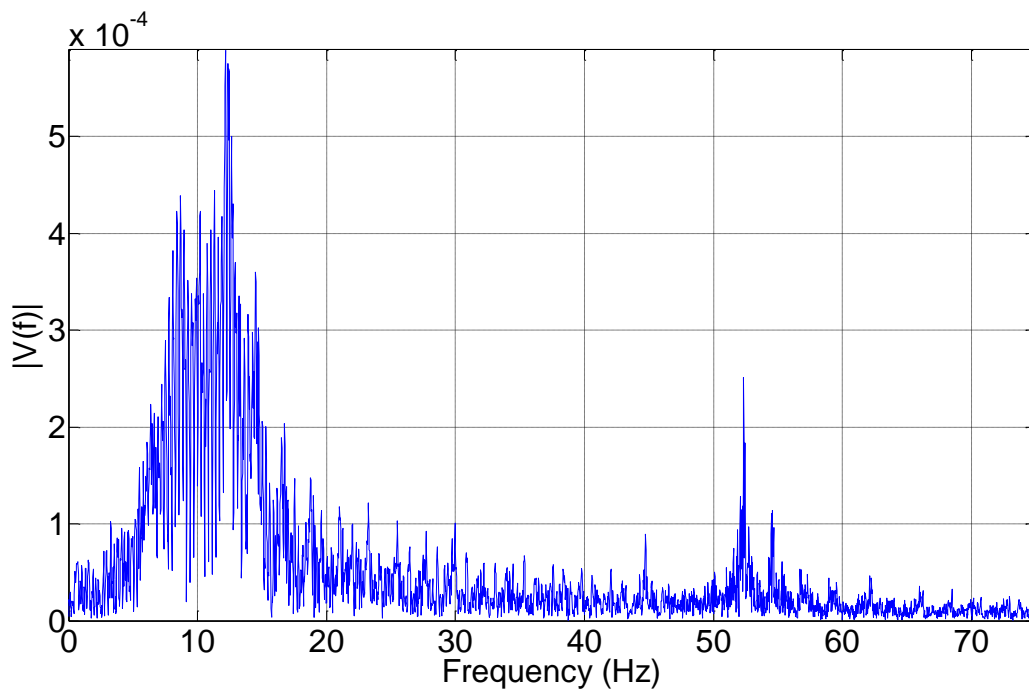

Figure 94: FFT of the induced voltage as a function of time indicating the ideal frequency for operation of this HS IV 20% sample as an energy harvesting is around 12.17 Hz.

Figure 95: Voltage induced within the pick-up coil for HS IV 30% cantilevered beam vibration sine sweep signal.

Figure 96: FFT of the induced voltage as a function of time indicating the ideal frequency for operation of this HS IV 30% sample as an energy harvesting is around 12.96 Hz.
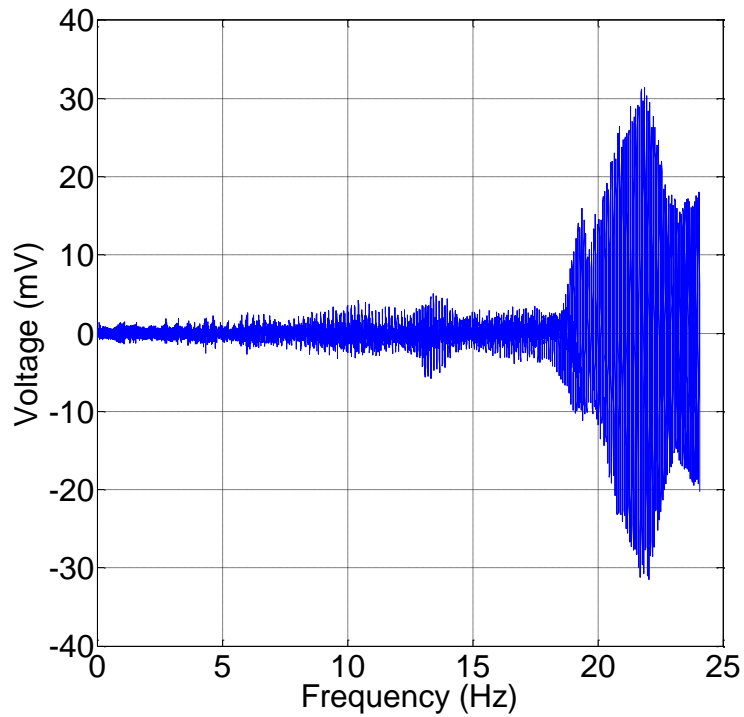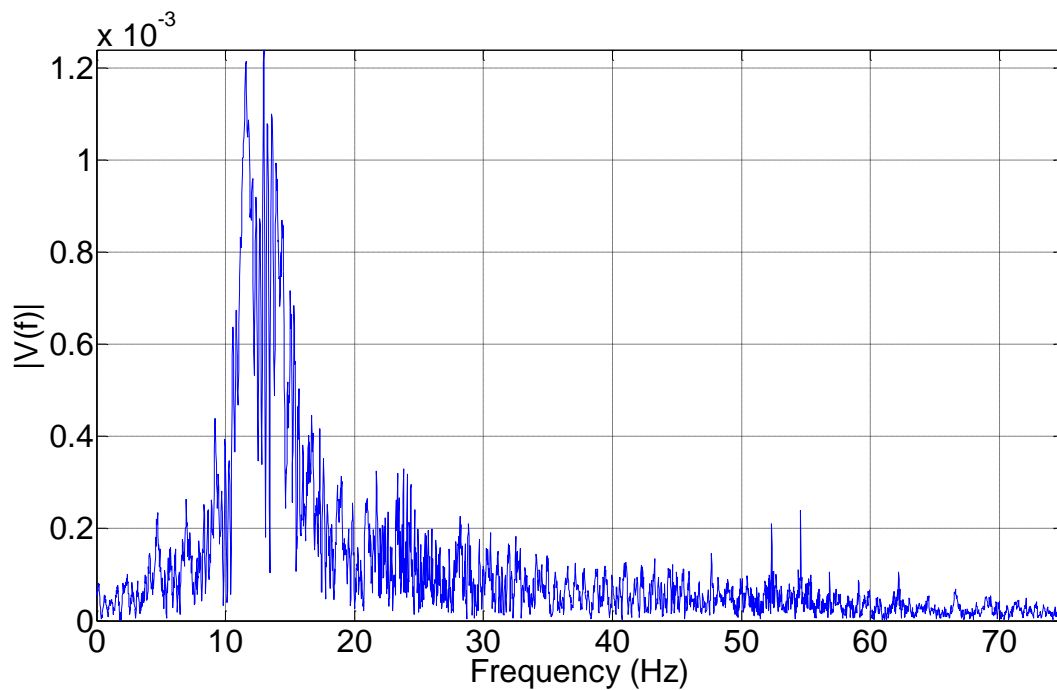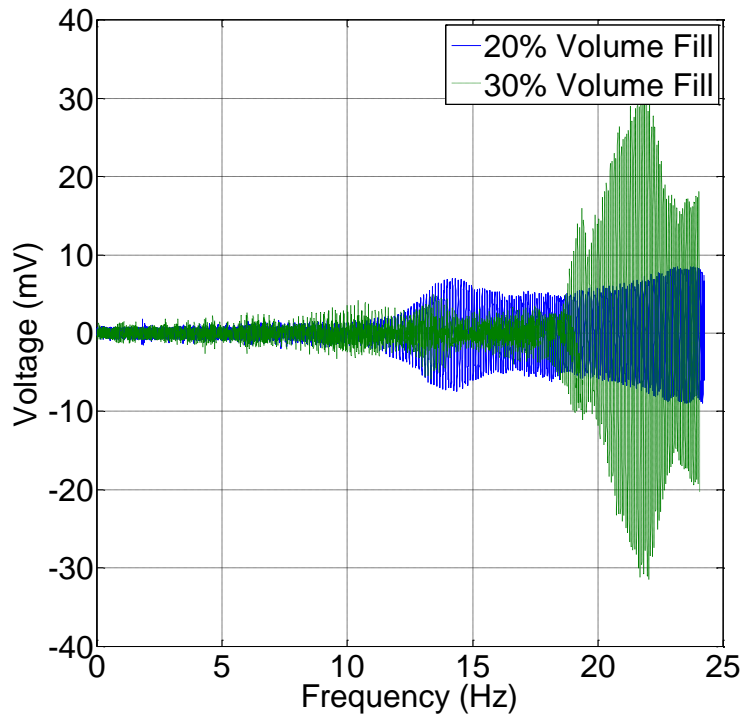
Figure 97: Comparison of the voltage induced within the pick-up coil for both HS IV cantilevered beam vibration sine sweep signals, indicating that the peak-to-peak voltage increased with increasing volume fill percentage.
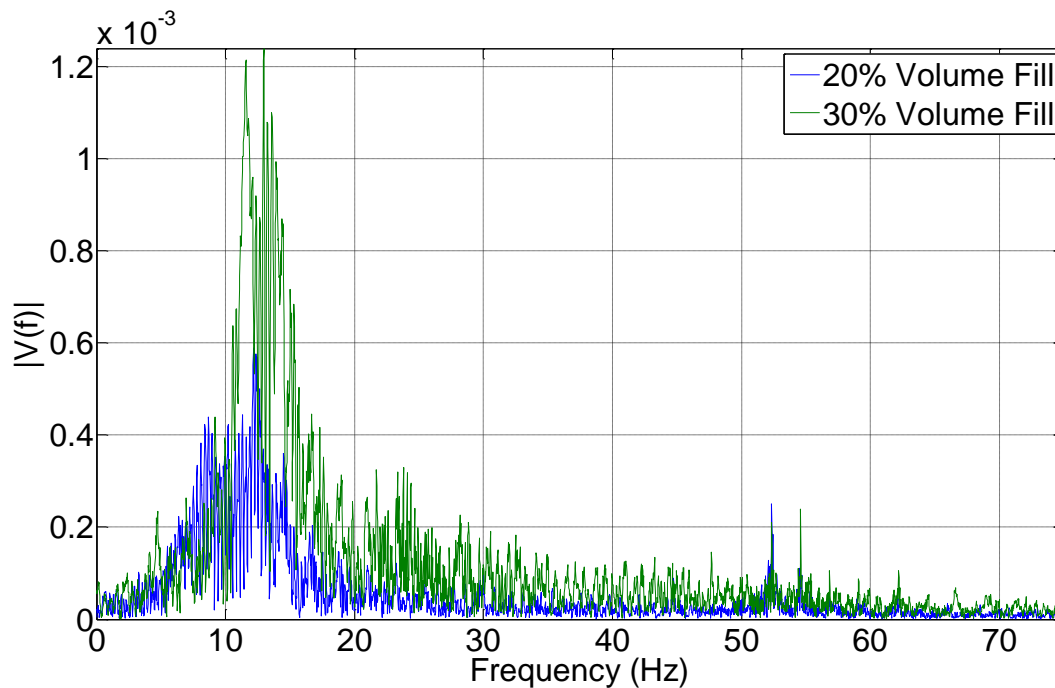

Figure 98: FFT signals for both of the HS IV samples, again demonstrating that there is a difference in the maximum induced voltage for each sample and also indicating the slight shift in ideal operating frequencies for each sample.

Table 9: Quantities used to calculate the mechanical efficiency as obtained from the energy harvesting experimental data. The voltage is used to calculate electric power, while the mechanical energy is a function of the square of velocity.

Sample	Quantity	7.5 Hz	10 Hz	12.5 Hz	15 Hz	20 Hz	25 Hz
HS II 10%	Voltage (mV)	1.0470	1.6640	1.3280	2.4140	18.7060	9.6890
	Mech. Energy (J/kg)	0.0391	0.0548	0.1075	0.1631	0.2954	0.4678
HS II 20%	Voltage (mV)	1.2290	1.4050	1.6810	3.6820	30.3680	20.4640
	Mech. Energy (J/kg)	0.0435	0.0696	0.1118	0.1713	0.3121	0.4930
HS II 30%	Voltage (mV)	2.3370	4.8610	2.8216	6.3770	52.8060	40.4210
	Mech. Energy (J/kg)	0.0405	0.0691	0.1007	0.1583	0.2904	0.4590
HS III 20%	Voltage (mV)	0.9040	1.2070	1.4940	2.0610	9.9320	34.2650
	Mech. Energy (J/kg)	0.0457	0.0791	01163	0.1789	0.3247	0.5125
HS III 30%	Voltage (mV)	2.6230	3.0700	4.1500	3.3510	7.3410	50.9590
	Mech. Energy (J/kg)	0.0452	0.0789	0.1140	0.1759	0.3216	0.5097
HS IV 20%	Voltage (mV)	1.0250	1.4880	1.6150	2.5680	5.3570	8.4710
	Mech. Energy (J/kg)	0.0422	0.0721	0.1149	0.1690	0.3046	0.4788
HS IV 30%	Voltage (mV)	1.8240	2.5900	2.8990	3.3840	3.4390	31.3990
	Mech. Energy (J/kg)	0.0441	0.0768	0.1142	0.1714	0.3106	0.4908